

**Springer Theses**  
Recognizing Outstanding Ph.D. Research

Yang Yu

# Orbital Dynamics in the Gravitational Field of Small Bodies



Springer

# **Springer Theses**

Recognizing Outstanding Ph.D. Research

## **Aims and Scope**

The series “Springer Theses” brings together a selection of the very best Ph.D. theses from around the world and across the physical sciences. Nominated and endorsed by two recognized specialists, each published volume has been selected for its scientific excellence and the high impact of its contents for the pertinent field of research. For greater accessibility to non-specialists, the published versions include an extended introduction, as well as a foreword by the student’s supervisor explaining the special relevance of the work for the field. As a whole, the series will provide a valuable resource both for newcomers to the research fields described, and for other scientists seeking detailed background information on special questions. Finally, it provides an accredited documentation of the valuable contributions made by today’s younger generation of scientists.

## **Theses are accepted into the series by invited nomination only and must fulfill all of the following criteria**

- They must be written in good English.
- The topic should fall within the confines of Chemistry, Physics, Earth Sciences, Engineering and related interdisciplinary fields such as Materials, Nanoscience, Chemical Engineering, Complex Systems and Biophysics.
- The work reported in the thesis must represent a significant scientific advance.
- If the thesis includes previously published material, permission to reproduce this must be gained from the respective copyright holder.
- They must have been examined and passed during the 12 months prior to nomination.
- Each thesis should include a foreword by the supervisor outlining the significance of its content.
- The theses should have a clearly defined structure including an introduction accessible to scientists not expert in that particular field.

More information about this series at <http://www.springer.com/series/8790>

Yang Yu

# Orbital Dynamics in the Gravitational Field of Small Bodies

Doctoral Thesis accepted by  
Tsinghua University, Beijing, China



Springer

*Author*  
Dr. Yang Yu  
Beihang University  
Beijing  
China

*Supervisor*  
Prof. Hexi Baoyin  
School of Aerospace  
Tsinghua University  
Beijing  
China

ISSN 2190-5053  
Springer Theses  
ISBN 978-3-662-52691-0  
DOI 10.1007/978-3-662-52693-4

ISSN 2190-5061 (electronic)  
ISBN 978-3-662-52693-4 (eBook)

Library of Congress Control Number: 2016939913

© Springer-Verlag Berlin Heidelberg 2016

This work is subject to copyright. All rights are reserved by the Publisher, whether the whole or part of the material is concerned, specifically the rights of translation, reprinting, reuse of illustrations, recitation, broadcasting, reproduction on microfilms or in any other physical way, and transmission or information storage and retrieval, electronic adaptation, computer software, or by similar or dissimilar methodology now known or hereafter developed.

The use of general descriptive names, registered names, trademarks, service marks, etc. in this publication does not imply, even in the absence of a specific statement, that such names are exempt from the relevant protective laws and regulations and therefore free for general use.

The publisher, the authors and the editors are safe to assume that the advice and information in this book are believed to be true and accurate at the date of publication. Neither the publisher nor the authors or the editors give a warranty, express or implied, with respect to the material contained herein or for any errors or omissions that may have been made.

Printed on acid-free paper

This Springer imprint is published by Springer Nature  
The registered company is Springer-Verlag GmbH Berlin Heidelberg

*To my parents, who supported me at each  
step of the way; And to my wife, who  
accompanied me writing this thesis.*

# **Supervisor's Foreword**

One of the core issues in modern celestial mechanics is the orbital dynamics in the near-regime gravitational fields of Solar System small bodies, which is related to the mathematical nature of a class of nonlinear systems, and plays a critical basis for in situ explorations of different scientific goals. Lots of efforts have been made to reveal the characteristics of orbital motion in the vicinities of asteroids, and to improve the skills of asteroid research in methodology. This impressive Ph.D. thesis focuses on the rich dynamics associated with a tracer particle orbiting around the arbitrarily shaped asteroid, which is modelled in great detail. As an exploration to this astrophysical frontier, the author, Dr. Yang Yu, mastered advanced topics in nonlinear dynamics, asteroid mission design and asteroid system formation. It is remarkable the author adopted both precise numerical models and theoretical qualitative analysis in this work, and this should be highlighted as a valuable exploration to the issues in the modern celestial mechanics, which has been in the face of increasing complexity and resolution today.

The main innovative work of this thesis: the author exposed the 3D structure of the zero-velocity surface of a specific asteroid, and explored the stabilities of its equilibrium points; an efficient numerical method was proposed for hierarchical search of large-scale periodic orbits, and by applying this methodology, 29 periodic families were found about the given asteroid, based on which the author further discussed the topological transitions and the general motion patterns around these periodic orbits; the study of resonant orbits near the equatorial plane presented the essence of 1:1 resonance and the distribution of resonant orbits; and in the study of the free motion near the asteroid surface, the thesis demonstrated how a detailed mechanical model may provide a feedback to our understanding of the coupled motion of the granular over the surface of a real asteroid.

This thesis was awarded 2014 Excellent Doctoral Dissertation of Tsinghua University, and got highly praised by the four reviewers, who concluded that this is a high-quality Ph.D. thesis, showing original results of academic significance and application value. I have benefited greatly from Dr. Yu's insights during our collaboration, and I hope you will share my experience after reading this book.

Beijing, China  
February 2016

Hexi Baoyin

# Preface

The orbital dynamics in the near-regime gravitational fields of Solar System small bodies (SSSB) is an important aspect of modern celestial mechanics, which is of abundant physical phenomena and offers insights into the mathematical expressions of astronomical events. During last two decades, several deep space probes have been launched for in situ explorations to these small worlds, and the orbital dynamics around a small body comes as one of the biggest challenges in space engineering. As an application of basic research, the work advanced in this thesis is about the common issues in the orbital dynamics around SSSBs, using high-resolution models, which serves as a bridge to the understanding of the orbital motion in the vicinity of a real small body.

Four types of orbits are discussed in this thesis: equilibrium points, periodic orbits, resonant orbits near the equatorial plane, and natural motion close to the surface. Specific asteroids' models are employed in these studies, and new algorithms are developed based on the polyhedral models, i.e. the Hierarchical Grid Search Method (HGSM) designed for searching the large-scale periodic orbits around a small body, and the surface mitigation model in order to mimic the complicated motion of a particle close to the surface. FORTRAN packages are developed for numerical implementation of these algorithms.

In the studies of equilibrium points and periodic orbits, we focus on the qualitative properties of the system, especially for the general behaviours of vicinal orbits. Four equilibrium points of asteroid 216 Kleopatra are exposed by checking the 3D geometries of the zero-velocity surfaces, and then their stabilities and topologies are determined. The general motion around the equilibrium points are decomposed into three types of local invariant manifolds, sketching out the general behaviours of nearby orbits. Six continuous families of local periodic orbits are obtained in the centre manifolds. In the study of large-scale periodic orbits, 29 new families around Kleopatra are generated using HGSM. Poincaré mapping is introduced to investigate the stability of the 29 families, and these families are classified into different types based on their topologies. It is noticed that the transition within the same family follows specific strategies, which characterizes the

topological evolution of the periodic orbits. Motions around the orbits of the 29 families are attributed to five simple patterns, and the general motion near the periodic orbits is qualitatively determined.

In the studies of resonant orbits near the equatorial plane and free motion close to the surface, we highlight the role of numerical experiments. The variation of orbital energy is analyzed to understand the dynamical nature of the 1:1 resonance. Grid search on the parameter space reveals the condition of this type of resonance. Observing that 1:1 resonance is the major cause of ejecting motions, we present the distribution of ejecting orbits around Kleopatra on the parameter space and determine the critical conditions. A high-risk region for the probes is found near Kleopatra for the rich ejecting orbits in the equatorial plane. The surface mitigation method is applied to the study of surface motion on asteroid 1620 Geographos. The global surface environment is evaluated, showing the connections between the free motions and the surface local geometries. Monte Carlo simulations are performed to investigate the trajectories initialized close to the surface. The results show that the free motions close to the surface are highly influenced by the local terrain, and several mechanisms may govern the free motion of different processes.

Noticing that most of this work is based on a specific small body, we generalize the results as consultative for similar types of issues. Essentially, the topics investigated in this thesis are common and representative for a large group of small bodies, and the ideas and approaches proposed here are supposed to be generic and portable.

## Acknowledgements

I would like to express special appreciation to my advisor Prof. Hexi Baoyin, who has been a tremendous mentor, always encouraging my work and allowing me to grow as a research scientist. I would also like to thank Prof. Junfeng Li, Prof. Tianshu Wang, Dr. Shengping Gong and Dr. Fanghua Jiang for the suggestions and discussions on my Ph.D. research. And thanks for the support of the National Basic Research Program of China (973 Program, 2012CB720000) and the National Natural Science Foundation of China (No. 11372150).

# Contents

<b>1</b>	<b>Introduction</b>	1
1.1	Background	1
1.2	Academic Merits and Significance	3
1.3	Research Status Survey	5
1.3.1	Progress in Astronautic Dynamics	5
1.3.2	Progress in Planetary Science	8
1.3.3	Progress in Nonlinear Dynamics	10
1.4	Content and Innovations	12
1.4.1	Content of the Thesis	12
1.4.2	Innovations of the Thesis	13
References		14
<b>2</b>	<b>Modelling Orbital Dynamics in the Potential of Small Bodies</b>	19
2.1	Introduction	19
2.2	Mechanical Environment in the Vicinity of Small Bodies	20
2.3	Descriptions of the Gravitational Field	24
2.3.1	Mass Point Cluster	25
2.3.2	Spherical/Ellipsoidal Harmonics	26
2.3.3	Polyhedral Method	29
2.4	Motion Equations	31
2.5	Dynamical Factor $\kappa$	33
2.6	Summary	36
References		37
<b>3</b>	<b>Stability of Equilibrium Points and Behaviour of Nearby Trajectories</b>	39
3.1	Introduction	39
3.2	Equilibrium Points of Asteroid 216 Kleopatra	40
3.2.1	Equilibrium Points	40
3.2.2	Zero-Velocity Surface	43

3.3	Stability of the Equilibrium Points . . . . .	45
3.4	Structure of Local Manifolds . . . . .	47
3.4.1	Three Types of Invariant Manifolds at $E_1$ and $E_2$ . . . . .	48
3.4.2	Three Types of Invariant Manifolds at $E_3$ and $E_4$ . . . . .	50
3.4.3	Periodic Orbital Families Determined from Central Manifolds . . . . .	51
3.5	Orbital Behaviours in the Neighbourhood of Equilibrium Points . . . . .	54
3.5.1	Behaviours of Trajectories Near $E_1$ and $E_2$ . . . . .	56
3.5.2	Behaviours of Trajectories Near $E_3$ and $E_4$ . . . . .	57
3.6	Summary . . . . .	59
	References . . . . .	59
<b>4</b>	<b>Topological Classification and Stability of Large-Scale Periodic Orbits . . . . .</b>	<b>61</b>
4.1	Introduction . . . . .	61
4.2	Periodic Orbits Around 216 Kleopatra . . . . .	62
4.2.1	Hierarchical Grid Search Method . . . . .	63
4.2.2	Families Generated Around Kleopatra . . . . .	66
4.3	Stability of Families 1–29 . . . . .	71
4.4	Topological Classification of Periodic Orbits . . . . .	74
4.5	Behaviours of Trajectories Near Periodic Orbits of 216 Kleopatra . . . . .	76
4.5.1	Periodic Orbits of Complex Saddle Type . . . . .	78
4.5.2	Periodic Orbits of Real Saddle Type . . . . .	80
4.5.3	Periodic Orbits of Central Saddle Type . . . . .	80
4.5.4	Periodic Orbits of General Centre Type . . . . .	81
4.6	Summary . . . . .	82
	References . . . . .	82
<b>5</b>	<b>Orbital Resonance Near the Equatorial Plane of Small Bodies . . . . .</b>	<b>85</b>
5.1	Introduction . . . . .	85
5.2	1:1 Resonant Orbits Near the Small Bodies . . . . .	86
5.2.1	Energy Equations . . . . .	87
5.2.2	A Mechanism of 1:1 Resonance . . . . .	88
5.2.3	Typical Resonant Orbits . . . . .	90
5.3	Parameter Dependence of the Resonance . . . . .	90
5.4	Resonant Orbits Near the Equatorial Plane of 216 Kleopatra . . . . .	93
5.4.1	Parameter Conditions for Orbital Resonance . . . . .	94
5.4.2	Distribution of the Ejecting Orbits . . . . .	94
5.5	Summary . . . . .	97
	Reference . . . . .	98

<b>6 Natural Motion Near the Surface of Small Bodies . . . . .</b>	99
6.1 Introduction . . . . .	99
6.2 Modelling Mechanics of the Surface . . . . .	100
6.2.1 Modified Polyhedral Method . . . . .	100
6.2.2 C <sup>1</sup> Surface Interpolation over the Polyhedron . . . . .	102
6.2.3 Equation of Motion on Surface . . . . .	104
6.3 Modelling the Natural Motion Near the Surface . . . . .	106
6.3.1 Triggering Events Within Orbital Motion Segments . . . . .	106
6.3.2 Triggering Events Within Surface Motion Segments . . . . .	108
6.3.3 Global Trajectory Patching Technique . . . . .	109
6.4 Verification and Assessment . . . . .	111
6.4.1 Example 1: Gravitational Field of a Solid Sphere . . . . .	111
6.4.2 Example 2: Demonstration Trajectories over Different Bodies . . . . .	112
6.5 Analysis of the Natural Motion Near Asteroid 1620 Geographos . . . . .	114
6.5.1 Surface Slope and Equilibrium Area . . . . .	114
6.5.2 Surface Curvature and Liftoff Speed . . . . .	115
6.5.3 Behaviours of Global Trajectories over 1620 Geographos . . . . .	117
6.6 Summary . . . . .	118
References . . . . .	119
<b>7 Conclusions and Future Directions . . . . .</b>	121
7.1 Conclusions . . . . .	121
7.2 Future Directions . . . . .	122

# Acronyms and Symbols

## Acronyms

CRTBP	Circular Restricted Three-Body Problem
SSSB	Solar System Small Body
NEA	Near-Earth Asteroid
NASA	National Aeronautics and Space Administration
ESA	European Space Agency
AU	Astronomical Unit

## Main Symbols

$\mathbf{r}, r$	Position
$\mathbf{a}, a$	Acceleration
$\omega, \omega$	Angular velocity
$L$	Orbital momentum of moment
$x$	State variable
$M$	Mass
$\sigma$	Bulk density of the small body
$R$	Radius of the influence sphere dominated by the small body
$D$	Mean distance from the sun to the small body
$U$	Gravitational potential
$V$	Effective potential
$H$	Hamiltonian function
$B$	Bézier surface function
$G$	Gravitational constant
$i$	Unit of imaginary number
$t$	Time
$\tau$	Normalized time
$\kappa$	Dynamical factor of orbital motion around the small body
$\rho$	Shape factor of the small body

$\Xi$	Discriminant index for the stability of the equilibrium point
$\Theta$	Discriminant index for the stability of the periodic orbit
$\mathbb{R}$	Set of real numbers
$\mathbb{N}$	Set of natural numbers

## Subscripts

A	Asteroid
$\odot$	The Sun
s	Solar radiation pressure
$f$	Face of the polyhedron
$e$	Edge of the polyhedron
e	Reference value in the spherical/ellipsoidal harmonics
$FS$	Face set of the polyhedron
$ES$	Edge set of the polyhedron

# Chapter 1

## Introduction

### 1.1 Background

In the story of mankind, explorations to unknown worlds have never stopped. Eager and curious adventures of every generation, heading for far places and pushing the limits, have empowered the progress of human civilization in history. The evolution of modern technologies spanned the world field of vision: scientists have pointed the Hubble telescope to the far reaches of the universe [1]; the interstellar space probe Voyager 1, has flied over the edge of outer Solar System, taking a golden record of human's information [2]; and the Hayabusa spacecraft has successfully returned the regolith samples from the Near-Earth Asteroid 25143 Itokawa [3]. It is a competition between the eyes and the footsteps, and the development of technology is undoubtedly crucial to this course. Distant sceneries are returned by new equipments and probes, which enable us to take an increasingly detailed look into our Solar System. The discovery and understanding of asteroids are the best indicators for this process. The history goes back scarcely over two hundred years when none in the world had realized the existence of Solar System small bodies, and Solar System in human mind was nothing more than the Sun and eight isolated orbiting planets. From the beginning of the nineteenth century, Solar System small bodies were found gradually, while the large number and masses could not be determined at that time. From late nineteenth century to middle twentieth century, people learned that the total mass of small bodies is tiny compared with the planets, leading to a decline of relative studies [4]. As it goes with a series of observations and space missions from 1920 to 1970s, the studies on Solar System small bodies have been renewed in multiple research fields, which revealed the chemical composition and general interior of the small bodies. Several asteroids' shapes have been determined from radar observations, and a few of them have even been imaged by spacecrafts with high resolution, showing abundant geomorphic features of the surfaces [5]. Nowadays it is established that Solar System small bodies probably include important information on the origins of the planets and the life on Earth, which might change our knowledge of some fundamental issues in nature [6, 7]. Briefly, the research course of recent 40 years

of small bodies reflects a profound change of modern view of nature, and it has a deep impact on the development of multiple related subjects (not just astronomy), e.g. planetary geology, cosmobiology, aerospace engineering and space weaponry, etc. All goes as the prophetic words by American astronomer Tom Gehrels in 1971, “We are now on the threshold of a new era of asteroid studies” [8].

Solar System small bodies encompass all the natural objects orbiting the Sun other than the planets and dwarf planets. And the majority of the components are asteroids distributed between the planetary orbits. In the early nineteenth century, Italian astronomer Giuseppe Piazzi discovered 1 Ceres, which is today known as the largest member of the asteroid belt (The uniform number of an asteroid is presented only when it is first mentioned in the context). After two centuries, today the asteroids with formal numbers have been over 380,000, and over 95 % of these were discovered in recent decades [9]. With the technical development in deep space explorations, human activities about asteroids have spread from remote sensing observations to in situ explorations with space probes. Following the moon and some planetary systems, asteroid has become one of the main targets of deep space exploration. The implement of an asteroid mission requires a combination of techniques in heliocentric orbital tracking and determination, global trajectory optimization, and autonomous navigation and control of spacecrafts. By and large, it reflects the current national comprehensive power, and will play as a significant role to future international strategic balance, space resource sharing and national space defence strength.

Since the 1920–1990s, several space missions have been proposed for small body exploration by NASA, ESA and JAXA [10, 11]. Table 1.1 lists these missions by the (planned) launching time. In October 1991 and August 1993, NASA’s unmanned spacecraft, Galileo, visited two asteroids 951 Gaspra and 243 Ida in midway of its journey to Jupiter, measuring the size, shape and surface craters of target asteroids; in 1996, NASA launched NEAR Shoemaker spacecraft, which made the first multispectral images of C-type asteroid 253 Mathilde, and landed on a NEA 433 Eros successfully; in 1998, Deep Space I probe flied by asteroid 9969 Braille and comet Borrelly and accomplished detections to the coma plasma and the gas streams on the nucleus; in 1999, NASA launched the comet probe Stardust, which successfully returned the dust samples of the coma of Wild 2; in 2005, NASA started the Deep Impact Program, aiming at a kinetic impact test on the nucleus of comet Tempel 1 to measure the ejecta and the shape, depth of the crater, and a subsequent flyby with comet Hartley 2 using Earth gravity assist; in 2006, the New Horizons Project was started, planning to explore the dwarf planet 134340 Pluto with its 5 moons, and to fly by a Kuiper belt object after that; in 2007, NASA launched spacecraft Dawn to visit the two largest asteroids 4 Vesta and 1 Ceres successively; NASA also plans to launch OSIRIS-REX Project in 2016, in order to send a spacecraft to NEA 101955 1999RQ36 and return samples to the Earth. ESA started ROSETTA Project in 2004, aiming at a close approach to comet 67P/Churyumov-Gerasimenko and releasing a lander on the nucleus’ surface for long-term tracking; as the importance of planetary defence arising in recent years, ESA initialized Don Quijote Concept in 2013, which is designed to demonstrate and validate the technology that can be used to deflect an asteroid threatening the Earth. JAXA launched HAYABUSA spacecraft in 2003,

**Table 1.1** A mission chronology of SSSB explorations

Mission name	Lunching time	Agency	Target SSSB
Galileo	1991	NASA	951 Gaspra; 243 Ida
NEAR Shoemaker	1996	NASA	253 Mathilde; 433 Eros
Deep Space I	1998	NASA	9969 Braille; Borrelly
HAYABUSA	2003	JAXA	25143 Itokawa
ROSETTA	2004	ESA	67P/Churyumov–Gerasimenko
Stardust	2005	NASA	5535 Annefrank; Wild 2
Deep Impact	2005	NASA	Tempel 1; Hartley 2
New Horizons	2006	NASA	134340 Pluto
Dawn	2007	NASA	4 Vesta; 1 Ceres
Don Quijote	2013	ESA	2003 SM84; 99942 Apophis
HAYABUSA-II	2014	JAXA; ESA	162173 1999JU3
OSIRIS-REX	2016	NASA	101955 1999RQ36

which was developed to return a sample of material from a small NEA 25143 Itokawa for further analysis. The probe made a rendezvous with Itokawa in September 2005, landed on its surface in two months, and finally sent the collected samples back to Earth in June 2010. The subsequent mission HAYABUSA-II, planned to be launched in 2014, will explore the C-type NEA 162173 1999JU3, and return a sample of materials deep under the regolith. Besides, NASA proposed a scheme of NEA capturing around 2013, planning to bring a small NEA of  $\sim 500$  tonnes into the lunar orbit. If approved and successfully executed, this would be a great engineering achievement of mankind in future space development.

It is worth mentioning that Chinese lunar probe Chang'E 2 made a close flyby with NEA 4179 Toutatis December 13, 2012, which was a new task achieved after scheduled tasks were completed. Close-up images of Toutatis' surface were obtained for the first time, which made China as the fourth space agency to conduct a successful mission to an asteroid after NASA, ESA and JAXA.

## 1.2 Academic Merits and Significance

The completed missions for SSSB exploration show a detailed research on the small bodies is of importance in multiple aspects. First, small bodies are “residuum” left from the early formation of Solar System, which did not participate in the process of planetary evolution, but experienced an equal long history and survived to date. Compared with the planets, they have lower evolutive degrees and preserve a relatively complete information of the early stage of the Solar System, which could be important clues to what have happened at the origin of the planets, and further, the start of life [12]. Second, small bodies are rich in mineral resources. For example, an

M-type asteroid of size  $\sim 1$  km may contain amounts of rare metals (nickel, platinum, cobalt, iridium, etc.) several times of those on Earth. Mining on an asteroid has been proposed and widely discussed as a new famous concept of space engineering [13]. Besides, a more practical reason for us to concern SSSB is, part of the near-Earth asteroids could be a great threat to planetary security. Mutual collisions or the effects of secular perturbations can alter the NEAs' orbits, and once a massive member of these perturbed objects impacts the Earth, it would be a devastating blow to human civilization. Date back to the history, disasters caused by meteorite impact are rare, like the death of dinosaurs at the end of Cretaceous period, the Tunguska Event in early twentieth century, and the Chelyabinsk impact on February 15, 2013 that injured over 1500 people and caused extensive property damage. All these events may serve as reminders for the asteroid impact hazard and emphasize the importance of discovering hazardous NEAs and learning how to mitigate them [14].

In situ exploration of the small bodies is able to provide abundant details and evidence to scientific researches, and demonstrate new technologies in real circumstances for further resource development. For future NEA deflection, it also contributes in estimating the parameters of target object, to ensure the accurate implementation of the deflecting operation. Hence it has advantages that cannot be replaced by remote observation. While in technology, sending probes to NEAs is a great challenge to national comprehensive power. Excluding the requirements on deep space orbital tracking and spacecraft's autonomous navigation, just the flight dynamics of a spacecraft around a small body will become especially difficult because of the surrounding complex mechanical environments. And the real missions will be obstructed by these difficulties. For instance when spacecraft HAYABUSA was approaching 25143 Itokawa for the second time in November, 2005, it released the landmark and the surface rover MINERVA at the altitude  $\sim 1.4$  km above the asteroid, but the latter failed to reach the asteroid surface as the predicted trajectory. Analysis after this accident shows the trajectory error should be caused by inaccurate estimation of the gravitational field of Itokawa [15]. Another example is about the Dawn mission, which entered the 4 Vesta's orbit in July, 2011. Earlier when the mission orbits were in planning, Tricarico and Sykes from Planetary Science Institute in Tucson pointed out that the spacecraft could be trapped in a band region, which is formed by the resonance between the orbit and Vesta's rotation [16]. And they asserted the resonant band is dangerous that cannot be escaped from by the propulsive system of the spacecraft. This effect was finally taken into account in the orbital design of Dawn mission. These facts show that the difficulty of the orbital dynamics around small bodies at least comes from two aspects. First, due to the limitation of measurements, spacecraft cannot obtain the complete information before approaching the target asteroid, e.g. the rotational state, the shape model and the gravitational data. It has to repeat measurements and corrections simultaneously during the approaching, which increases the risk of near-field flight. Second, the complex nature of this type of problems. Solar System small bodies are diverse in shapes, chemical composition and interior structures, and accordingly the gravitational field around them could be irregular and very different for each object; therefore the orbital behaviour around small bodies may differ significantly from that around the planets. Besides, most

small bodies have small mass, and the relative influence of space perturbations will be strong and cannot be ignored, e.g. the tidal forces from the Sun and planets, the radiative forces, etc. All these factors contribute to the abundant orbital behaviours around small bodies, and some internal mechanisms are still hidden, which presents new challenges to the near-field segments of orbital design and control.

As stated above, motion control of spacecraft around small bodies is unavoidable in techniques of in situ exploration and the importance of understanding the orbital dynamics around a small body is obvious for space mission. On the other hand, the formation of SSSB systems (e.g. binary systems and asteroid families), and the geological evolution of individual asteroids (e.g. the shape, interior and surface features) all have proven to be related with the orbital behaviours in their vicinities [17, 18]. The study of orbital dynamics would help us to find the intrinsic reasons behind the phenomena, and further to find a driven model for the evolution of this part of Solar System. In addition, a theoretical framework of the local/global behaviours of a general nonlinear system has been established, concluding a series of mechanisms of different scales that need to be found and verified with real physical objects [19]. A mass point moving in the irregular gravitational field is regarded as a typical model of the practical system, which presents a new frontier to explore in theory that enriches the connotation of modern celestial mechanics.

## 1.3 Research Status Survey

Orbital dynamics around Solar System small bodies can be discussed from the perspectives of multiple subjects. A massive study under this topic started from 1920–1990s, against the background of NASA’s missions for asteroid exploration. The motion control, orbital design and dynamical environment analysis of the spacecraft were concentrated in the field of astrodynamics at first. Nearly at the same time, researchers of celestial mechanics and planetary physics started to explore the formation and evolution of small bodies by combining new results of observations. Correspondingly, progresses in asteroid exploration also inspired a theoretical interest of nonlinearity researchers, who have organized studies of dynamical behaviours in special gravitational field aiming at the real asteroidal issues. This section will summarize the progresses and status of these research fields.

### 1.3.1 Progress in Astronautic Dynamics

The orbital dynamics around small bodies is essentially concerning a special kind of gravitational field induced by irregular massive bodies. Researchers in astronautic dynamics usually begin with the applied aspects, e.g. the approximation of asteroidal gravity field. Spherical harmonics are conventionally used as a classic method to describe the gravitational field of arbitrary celestial object [20], i.e. the objective

field is expanded as spherical harmonic series based on a central item to approximate its non-spherical perturbation (see Sect. 2.3.2). In this method, the volumetric integral of gravity/potential over the central body is converted to a surface integral, and is then reduced to a series of harmonic coefficients  $C_{nm}$  and  $S_{nm}$ , which determine the geometric properties of objective field. The spherical harmonic method provides a uniform formulation for arbitrary central body [21], and this formulation proves linear to  $C_{nm}$  and  $S_{nm}$ , which enables us to identify their values conveniently from the flight data records. Thus, spherical harmonics were widely applied in calculating the near-Earth orbits of satellites. Since the 1920–1930s, a rich literature has been published on inversion algorithms of harmonic coefficients [22–24]. While the major flaw of spherical harmonics is the convergency depends on the position outside the reference sphere, i.e. the closer to the reference radius, the slower the convergency becomes, and the method completely fails inside the reference sphere [25]. An important modification was first made by Bierly, MacMillan and Hobson, who proposed the ellipsoidal harmonic method [26–28], which defines a reference triaxial ellipsoid as the envelope of the central body, and then solves the harmonic coefficients of different orders and degrees according to the three semi-axes. Obviously, it is able to provide a wide region of convergency closer to the irregular central body, like asteroids, which is more qualified for the study of orbital dynamics around small bodies [29]. For those small bodies whose shapes are not well determined, a simple way is usually to describe their shapes as triaxial ellipsoids directly, and the expressions of gravity and potential can be derived analytically [30]. This reduced expression fits theoretical investigation better, and German, Friedlander and Scheeres et al. studied some particular forms of orbital motion around a uniformly rotating ellipsoid [31, 32].

A space mission for asteroid requires an accurate estimation of the gravitational field around the target object, which highly relies on its dimension and shape. A straightforward approach to describe the mass distribution over a small body is to assume it as a homogeneous polyhedron, and then the gravity from the small body will be expressed as a volumetric integral over the polyhedron. Explicit expressions of the gravity/potential can be derived following conventional routines (hereafter referred as “polyhedral method”). The study on the gravitational field induced by a homogeneous polyhedron could date back to the end of nineteenth century [33], while it makes a validate method to solve the asteroidal gravity until recent decades as the development of computer technology. Werner derived the analytical forms of the exterior gravitation of a constant-density polyhedron in 1993 [34], and Scheeres et al. applied this polyhedral method to their study of orbits around asteroid 4769 Castalia [35]. Then, the polyhedral method was increasingly used in asteroid mission analysis, as well as in theoretical studies. Forsberg proposed a method to approximate the gravitational field of a non-homogeneous polyhedron, i.e. to divide the polyhedron into multiple unit tetrahedrons assigned with varying density, and sum up the gravities from all these units [36]. Petrović and Pohánka et al. reformulated the conventional expressions of the polyhedral method to suit programming [37, 38] and Tsoulis et al. determines the singularity condition of those formulas [39]. Generally, the polyhedral

method has been one of the most mature and effective approaches to deal with the orbital dynamics near small bodies. We will detail this method in Sect. 2.3.

Classic orbital theory and methods are a basic guide for the studies of orbital motion around small bodies. On the one hand, conventional perturbation method is still being used to analyze the effects of non-spherical item and other items of perturbations near a small body; on the other hand, the equation form of orbital motion in asteroidal gravitational field is close to that of the circular restricted three-body problem (hereafter referred as CRTBP), which has been one of the central topics in celestial mechanics during the past century. It has been established fact that several methods and conclusions from CRTBP can be extended directly into our problem. Since the 1920–1990s, Scheeres et al. began to model the gravitational field of some asteroids with the polyhedral method, and to analyze the orbital behaviours nearby these small bodies [35]. Taking asteroid Castalia as an example (it has a radar shape model), Scheeres et al. show the motion equation has a generalized energy integral, and there exist equilibrium points, zero-velocity surfaces and Hill region defined like those in CRTBP. In the study of the equatorial orbits, they found the geosynchronous orbits and prograde orbits both unstable, i.e. these two types of orbits eventually escape from Castalia or collide with it, while most of the retrograde orbits are stable, meaning the orbital shape only shifts slightly with the mission duration. Reference [40] presents the existing condition of ejecting orbits based on a rotating second degree and order gravity field, revealing the resonant mechanism between the rotation of asteroid and the angular velocity of the orbit. In the study of a tumbling NEA Toutatis, Scheeres et al. found a type of quasi-periodic frozen orbits effected by  $C_{20}$ , and presented the general effects of  $C_{20}$  and  $C_{30}$ . They also discovered several simple periodic orbits around Toutatis using the polyhedral method [41]. Based on these results, Hu and Scheeres presented the possible periodic motion in the equatorial plane using the gravitational field of second degree and order [42]; Wang and Xu studied the effects of gravity gradient torque on the altitude motion of spacecraft [43]; Antreasian et al. applied averaging method together with the second degree and order gravity to seek the stable motion around asteroid 433 Eros, and achieved a family of retrograde orbits [44]. As the studies going deeper, other forms of perturbations were taken into account. Reference [45] shows the tidal forces from the large objects of Solar System and the solar radiation pressure can also affect the stability of the orbits of spacecraft around an asteroid.

The diversity of Solar System small bodies in size, shape and components has always been an obstacle to in situ explorations. The successful implementation of a few previous missions acquired precise physical properties of the target small bodies, which enables a detailed estimation to the dynamical circumstances around them. Schemes and Williams et al. gave a complete analysis of the orbital motion near an NEA Eros based on data returned by NEAR Shoemaker spacecraft, e.g. the limits of stable orbits are determined using an approximation analysis, and the stable condition of periodic orbits is discussed. The results show that the stability of retrograde motion near the equatorial plane of Eros is conditional, which plays significant role in redesigning of the complete mission [46]. In 2005, spacecraft HAYABUSA accompanied the NEA Itokawa for over 3 months, and high-resolution models of the shape

and gravitational field are obtained, with which Scheeres and Gaskell et al. discussed the general gravitational properties of the shape model assuming a constant-density and the actual dynamical environment both on the surface and in orbit [47]. Reference [47] also detailed one trajectory of a close approaching to the surface of Itokawa, showing the methodology is reliable. Besides, at the beginning of Dawn's exploration to Vesta, Tricarico and Sykes analyzed the 1:1 resonance with multiple gravity models, and pointed out the risky working conditions for the spacecraft referring to the propulsion limits, which was later considered into the designing of flight mission [16]. In summary, a precise estimation to the dynamical environment around a small body is not only important to academic research of astronautic dynamics, but also very consultative to the design of future asteroid missions.

On the other hand, the understanding the orbital dynamics around a small body is also crucial to the motion control of the spacecraft. No matter whether the task is companion, hovering, orbiting, landing (for relatively big objects like Eros) or approaching, touchdown, sampling (for relative small objects like Itokawa), it requires an appropriate dynamic modelling as the precondition of applying a control scheme. Broschart et al. studied active control strategies about the body, and derived the forms of hovering control laws both in the body-fixed and inertial reference frames. Perturbation equations for inertial frame hovering were presented and numerically simulated to identify regions of stability, and the stable region of body-fixed hovering were found to be roughly approximated by the body's resonance radius [48]. Reference [49] discussed the design of landing mission of NEAR Shoemaker on Eros. Recurrences were given to the landing scenario using radio metric, optical landmark and laser ranging tracking data, which determined the characteristics of the landing to be within the expected dispersions. Lantoine and Braun described a technique for computing optimal autonomous controlled trajectories for soft landing in an irregular gravity field of a rotating asteroid. The complexity of technical environment was discussed first, and the numerical method to solve the optimal control problem was also presented. Example cases were studied at asteroids Vesta and Golevka, in which they identified the best mission design scenarios and the parameter uncertainties of landing process for both cases [50]. Beyond the close approaching phase, the choice of landing site is also crucial to the mission. References [51, 52] surveyed the constraint conditions of landing site choosing, including the landform, communication and lighting conditions, scientific merit and technical obstacles, etc. As for the motion control of surface rover, Refs. [40, 47] presented the launching speed depending on the geomorphology of different target asteroids. Bellerose and Scheeres analyzed the stability of the equilibrium region over a rotating triaxial ellipsoid, and developed control laws to limit the range of the rover's motion on the ellipsoidal surface [53].

### 1.3.2 Progress in Planetary Science

Plenty of binary asteroid systems have been found by observation during the past 20 years, which draw a lot of attention of the planetary scientists. The first hypothesis on

binary asteroid could date back to two centuries ago, when Ceres was first discovered and was predicted to have a moon. Until 1993, when Galileo probe first flew by Ida and found the satellite Dactyl 1, the binary asteroid was confirmed to exist [54]. So far, over 200 binary asteroids have been registered. These binary systems are important, because they give information on the mass and density of asteroids, and show clues to understanding the dynamics of planetary systems [55]. Scheeres et al. surveyed the stable orbits under highly non-spherical perturbation, in order to find out the possible orbits of natural satellites [56, 57]. Scheeres and Bellerose further introduced a full two-body model into the study of binary orbits [56, 58]. Maciejewski presents the equations of absolute motion and relative motion of the full two-body model, and gave a discussion on the possible equilibrium phases [59]. Scheeres analyzed the stable condition of the binary motion based on an ellipsoid–sphere model [60]. At the same time, the calculation of mutual gravity and potential has been widely studied: Refs. [61, 62] present expressions of mutual potential in spherical harmonics, showing a more serious convergency problem than the singleton [63]; Refs. [64, 65] give a more straight approach, to discrete the two bodies into clusters of mass points, and calculate the potential/gravity by summing up that between the mass points; Ref. [35] points out this method has a very slow rate of convergency, which could be computationally expensive; similarly as the singleton case, Werner and Scheeres proposed a method to approximate the mutual gravity based on the polyhedral shape model [66], which shows better convergence and successfully applied in their subsequent studies; Refs. [67, 68] presented the expressions of gravity and gravitational torque between two homogeneous polyhedrons in different frames. On the other hand, it was noticed traditional integration methods may encounter precision problems in simulations of the full two-body system, Fahnestock and Lee et al. developed the Lie Group Variational Integrator (LGVI) to improve the accuracy and efficiency [68, 69]. Fahnestock et al. applied this method to analyze the motion of NEA binary 66391 1999K W4 [57]. Scheeres et al. derived the practical motion of 1999K W4 based on radar observation and numerical simulations, showing the primary has a high rotational speed (approaching the limit of stability [70]), and the secondary largely lies on the equatorial plane (showing a significant orbital precession due to the solar perturbation at the perigee). This is consistent with the formation theory proposed by McMahon and Richardson et al., that the secondary of 1999K W4 was originally reaccumulated from nearby debris, which was ejected from the primary’s equator as it was gradually pinned up by YORP effect [71].

The evolution of small bodies involves abundant dynamical phenomena, and a detailed look into the orbital behaviours around the small body will help to understand the geologic features of its surface. For instance, an asteroid may take a lot of impacts from micro-meteorites [72], and the craters will take a long time to degenerate [73]. Part of the ejected material may fall back to the surface and reaccumulate, part may escape from the vicinity of the asteroid, and the remaining part may enter temporary orbits around the asteroid [74]. A lot of researches on the orbital motion of the ejecta were published in 1920–1990s [75]. After the NEAR Shoemaker probe sent

back the images of Eros' surface, there appeared a growing interest on the formation of several geological features, which was believed to be correlated with the ejecta evolution [76]. Weidenschilling et al. pointed that a study on the orbital dynamics of the ejecta could give clues to these problems [77]. Hamilton and Burns investigated the boundary of stable orbits around an asteroid, aimed at an explanation on the stability zone [78, 79]. Chauvineau et al. studied the influence of solar tide on the ejecta motion [80], and Richter et al. studied the orbital features of ejecta moving close to the stability limit [81, 82]. Since 1993, Chauvineau and Scheeres et al. published their research on the dynamical environment around specified asteroids [83], showing the differences of the surroundings of small bodies from that of the planets. Geissler et al. simulated the orbital motion of ejecta from the biggest crater Azzurra on asteroid Ida, with a detailed dynamical model employed, and the results show good consistent with the observation, that the reaccumulated ejecta profoundly changed the optical features of northwest part of Ida's surface [64]. This work is significant, not only because of its contribution to the studies of Ida, but also because it displayed the power of a detailed dynamical model in understanding the real astronomical phenomenons. This work influenced several researchers afterwards [84–86]. Durda et al. developed the tracer model of ejecta dynamics around asteroid Eros, which, combining the surface images, can be used to back track the source craters, linking with some specific impact events [87].

Besides, among the craters observed on asteroid surfaces, the “double crater” (meaning two craters close or adjacent, with similar geological age) takes a high percentage. A widely accepted hypothesis on the formation of double crater is that the meteorite is disrupted during the rendezvous with the asteroid, and the two separated parts impact on the asteroid surface at a short interval [88]. During the last two decades, there was an increasing attention on the encounter history of asteroids, which has partly interpreted the formation of “double crater”, and has made it a new hotspot in the planetary research [89].

### 1.3.3 Progress in Nonlinear Dynamics

The motion of a test particle in a gravitational field makes an important kind of nonlinear system. As for the potential of the planets, the conventional perturbation analysis has provided complete results. In comparison, the gravitational fields of small bodies show a huge diversity and are more complicated in geometry, which leads to more various orbital behaviours. The activities of asteroid explorations from the end of the twentieth century also motivated the studies of nonlinear dynamics under special backgrounds.

In this context, gravitational fields induced from simple geometries are usually adopted as the abstract models. Halamek used a massive line segment to approximate the prolate objects [89]. Prieto-Llanos et al. investigated the equilibrium points

around these spinning massive line segments and discussed their linear stabilities. They proposed an algorithm of stabilization control, and verified it using the model of Phobos (a natural satellite of Mars) [90]. Riaguas et al. further studied the nonlinear stabilities of the equilibrium points using the theory of Arnold [91], talking about the stability of orbital motion close to the equilibria including the resonant cases [92]. Riaguas and Elipe et al. considered the non-spinning case, and presented the periodic orbital families around the straight segment model with bifurcations [93]. Liu et al. took the homogeneous unit cube as a typical object and studied the nearby orbits systematically, like the equilibria, periodic orbits [94], homoclinic and heteroclinic connections [95], and equilibrium region on its surface [96]. The triaxial ellipsoid is another simple geometry frequently adopted to approximate the small bodies [97]. Reference [32] presented the stability criteria of equilibrium points based on a uniformly rotating homogeneous ellipsoid, and revealed several common features of orbits around an oblate body. Kammeyer focused on the periodic orbits around the ellipsoid, and analyzed the bifurcations using Morse Lemma [98].

Among the above researches, the symmetry of gravitational field played a part role in analysis, which is just the practical asteroids have been lacking. Yu and Baoyin took the asteroid 216 Kleopatra as an example, studied the stabilities of the equilibria and orbits nearby [99]. Based on the irregular gravitational field model, they also surveyed the resonant orbits near the equatorial plane of Kleopatra, and presented the distribution and conditions of ejected orbits [100]. Reference [101] proposed a scheme to search large-scale periodic orbits around irregular bodies, which was then applied to find out the periodic orbital families of Keopatra, showing the influence of asymmetry on periodic orbits.

The geometric interpretation to the structure of a dynamical system has greatly affected multiple branches of physics [102]. Likewise, works have been done in this way to explore the orbital dynamics around small bodies. Gutiérrez-Romero et al. gave a method to compute explicitly the asymptotic expressions of invariant manifolds near the equilibrium points [103], in which they made two different Lie transformations of the original Hamiltonian, revealing the composition of three types of local manifolds, the 2D-tori and quasi-periodic orbits. Jiang et al. presented a new metric to link the orbit and the geodesic on local manifolds, and classified the equilibrium points into 8 types [104].

Since the orbital equation around a uniformly rotating small body holds Hamiltonian form, the symplectic geometry has also been applied in the study of orbital dynamics. Maruskin et al. considered fundamental constraints on the evolution of symplectic sub-volumes, and presented a numerical method for deriving a symplectic state transition matrix for an arbitrary Hamiltonian system, which preserved the natural symplectic structure and proved to be computationally efficient [105, 106]. Numerical examples showed this method improved the accuracy of state transition matrix computation, as compared with the conventional linear method with Runge-Kutta integrations.

## 1.4 Content and Innovations

### 1.4.1 Content of the Thesis

This chapter gives an introduction to the background of our study, together with the academic Merits and the research status of the orbital dynamics around a small body.

Chapter 2 discusses the modelling methodology of a particle moving around the small body. A previous analysis on the magnitudes of perturbational forms discriminates the region where the small body's gravity plays as a dominant role. Three main numerical methods to calculate the gravity are compared, showing the advantages and disadvantages. A general form of the orbital motion equation is presented with the potential expressed by polyhedral method. And the common features of this equation form are discussed as a preliminary. The last part of this chapter derives a unitless form of the orbital equation, and proposes a basic dynamical factor, which proves to have a crucial influence on the global scheme of the orbital behaviours.

Chapter 3 focuses on the equilibrium points of the motion equation, and the orbits within their neighbourhoods. A real asteroid Kleopatra is specified as the example, and the 3D zero-velocity surfaces are constructed, revealing the 4 equilibrium points around the target asteroid. The stabilities of the linearized systems at the equilibrium points are discussed, by which the topologies of these points are determined. Noticing the topological equivalence between the original and linearized systems, the orbital motion near the equilibrium points are decomposed into three types of local invariant manifolds. Furthermore, the general orbital patterns near the equilibrium points are determined through analysis on the structure of local manifolds.

Chapter 4 surveys the large-scale periodic motion around the small bodies. First, we propose the Hierarchical Grid Search Method for searching periodic orbits around an irregular massive body. This method is then applied to asteroid Kleopatra, and a total of 29 families of periodic orbits are found around it. Then the stabilities of these orbital families are examined by using Poincaré mapping to create an equivalent discrete system. A linearized analysis shows topologies of different orbital families, based on which these periodic orbits are classified into 7 types. The topological evolution within the same orbital family is tracked, and 4 typical topological structures are obtained. The last part of this chapter discusses these 4 structures, and derives the general motion patterns of orbits near periodic orbits of these 4 types, respectively.

Chapter 5 studies the orbital resonance near the equatorial plane of a small body. The 1:1 resonant orbits around asteroid Kleopatra are investigated under the accurate gravity model. We start with an analysis on the orbital energy, revealing the mechanical essence of 1:1 resonance near the small bodies. Then based on the results of Monte Carlo simulations, we present the parameter dependence of 1:1 resonance on Jacobi integral. A classification of resonant orbits is proposed according to the orbital energy change, and example orbits are given for each class. The rest of this chapter focuses on the ejecting orbit, and numerical experiments show its proportion and distribution over a wide parameter space.

Chapter 6 focuses on the migration of a grain on/over the surface of a small body. First, a global valid method is proposed to calculate the gravity and potential near/on a small body, and an interpolated surface model is developed to smooth the surface. The surface motion equation is derived, which is combined with the orbital motion equation, constituting the core of our methodology. The event-driven strategy is adopted to implement full simulation of a tracer particle moving over the surface of an asteroid. A series of fundamental tests are performed to validate our method, and the last part of this chapter applies this model to explore the surface mechanical environment of specified asteroid 1620 Geographos. The connections between the local geological features and the behaviours of the test particle are investigated through numerical simulations, and the results show the major mechanisms affecting the free motion over the surface.

### ***1.4.2 Innovations of the Thesis***

In the studies related to mechanical problems, there has always been a contradiction between the modelling sophistication and the thorough analytic understanding. The work advanced in this thesis joins together the detailed modelling methods and the qualitative analysis of orbital behaviours, i.e. an effort is made to keep using accurate dynamical model of the target object to explore the common issues of systems of the same kind. Various analytical and numerical approaches are adopted and combined in this study, which, to some extent, has broadened the ways of solving problems in modern celestial mechanics.

The specific innovations include the following:

1. In the study of equilibrium points, we present the 3D structure of the zero-velocity surface of Kleopatra, and find its 4 equilibrium points. A unitless dynamical factor is proposed, and we prove it has a crucial influence on the dynamical behaviours of the system. The general patterns of orbits near the equilibrium points are determined via decomposition into local manifolds.
2. In the study of periodic motion, we propose the Hierarchical Grid Search Method, and apply it to find out 29 periodic families around Kleopatra. The common features of topological transformations within the same family are revealed, and the general motion patterns around a periodic orbit are determined though linearized analysis of the Poincaré map.
3. In the study of resonant orbits near the equatorial plane, we interpret the essence of 1:1 resonance from the energy point of view. The parameter condition of resonance on the equatorial plane is derived, and the distribution of ejecting orbits is presented.
4. In the study of the grain's migration near the surface, we present the surface motion equation and propose an event-driven model to implement full simulation

of a tracer particle on the target asteroid. Correlations between the local geological features and the dynamical behaviours of the tracer particle are revealed. An analysis of the mechanical environment on asteroid Geographos shows the dominant mechanisms affecting the mitigation paths.

## References

1. Scoville N, Abraham RG, Aussel H et al (2007) COSMOS: hubble space telescope observations. *Astrophys J Suppl Ser* 172:38–45
2. Burlaga LF, Ness NF, Stone EC (2013) Magnetic field observations as voyager 1 entered the heliosheath depletion region. *Science* 341:147–150
3. Akira T, Masayuki U, Takashi M et al (2011) Three-dimensional structure of Hayabusa samples: origin and evolution of Itokawa regolith. *Science* 333:1125–1128
4. Cunningham C (1998) Introduction to asteroids: the next frontier, 1st edn. Willmann-Bell, Virginia
5. Dankanich JW, Landau D, Martini MC et al (2010) Main belt asteroid sample return mission design. In: Proceedings of the 46th AIAA/ASME/SAE/ASEE joint propulsion conference & exhibit, Nashville, TN, United States, 25–28 July 2010
6. Safronov VS (1969) Evolution of the protoplanetary cloud and formation of the earth and planets. Nauka, Moscow
7. Weidenschilling SJ (2000) Formation of planetesimals and accretion of the terrestrial planets. *Space Sci. Rev.* 92:295–310
8. Bottke Jr WF, Cellino A, Paolicchi P et al (2002) Asteroids III. University of Arizona Press, Tucson
9. IAU (The International Astronomical Union) Minor Planet Center. Issue 2013. <http://www.minorplanetcenter.net/mpc/summary>
10. Farquhar R, Kawaguchi J, Russell C (2002) Spacecraft exploration of asteroids: the 2001 perspective. In: William F et al (eds) Asteroids III. University of Arizona Press, Tucson, pp 367–376
11. Cheng AF, Santo AG, Heeres KJ et al (1997) Near-Earth asteroid rendezvous: mission overview. *J. Geophys. Res.: Planets* 102:23695–23708
12. Hu Z, Xu W (2008) Planetary Science. Science Press, Beijing, pp 334–365
13. Zacny K, Chu P, Craft J et al (2013) Asteroid mining. In: Proceedings of the AIAA SPACE 2013 conference and exposition, CA, San Diego, 10–12 Sept 2013
14. Galimov EM, Pillinger CT, Greenwood RC et al (2013) The Chelyabinsk fireball and meteorite: implications for asteroid hazard assessment. In: Proceedings of the 76th annual meeting of the meteoritical society, Edmonton, Canada, 29 July–7 Aug 2013
15. JAXA (Japan Aerospace Exploration Agency). Issue 2010. <http://www.isas.jaxa.jp/j/topics/topics/2005.shtml>
16. Tricarico P, Sykes MV (2010) The dynamical environment of dawn at Vesta. *Planet. Space Sci.* 58:12–38
17. Cintala MJ, Head JW, Wilson L (1979) The nature and effects of impact cratering on small bodies. In: Gehrels T (ed) Asteroids. University of Arizona Press, Tucson, pp 579–600
18. Housen KR, Wilkening LL, Chapman CR et al (1979) Regolith development and evolution on asteroids and the Moon. In: Gehrels T (ed) Asteroids II. University of Arizona Press, Tucson, pp 601–627
19. Shilnikov LP et al (2010) In: Jin C (ed) Methods of qualitative theory in nonlinear dynamics, pt 1, 1st edn. Higher Education Press, Beijing, pp ix–xi (Trans.)
20. Liu L (2004) Orbital theory of spacecraft. National Defence Industry Press, Beijing
21. Hobson EW (1965) The theory of spherical and ellipsoidal harmonics. Chelsea, New York

22. Chao BF, Rubincam DP (1989) The gravitational field of Phobos. *Geoph. Res. Let.* 16:859–862
23. Barnett CT (1976) Theoretical modeling of the magnetic and gravitational fields of an arbitrary shaped three-dimensional body. *Geophysics* 41:1353–1364
24. Jamet O, Thomas EA (2004) Linear algorithm for computing the spherical harmonic coefficients of the gravitational potential from a constant density polyhedron. In: 2nd GOCE user workshop, GOCE, The geoid and oceanography, ESA-ESRIN, Frascati, Italy, 8–10 Mar 2004
25. Heiskanen WA, Moritz H (1967) Physical geodesy. W.H. Freeman, San Francisco
26. Bierly W (1897) An elementary treatise on fourier's series and spherical, cylindrical, and ellipsoidal harmonics. Ginnand Company, London
27. MacMillan WD (1930) The theory of the potential. McGraw-Hill, New York
28. Hobson E (1955) The theory of spherical and ellipsoidal harmonics. Chelsea Publishing Company, Vermont
29. Romain G, Jean-Pierre B (2001) Ellipsoidal harmonic expansions of the gravitational potential: theory and application. *Celest. Mech. Astron.* 19:235–275
30. Dobrovolskis AR, Bruns JA (1980) Life near the Roche limit: behavior of ejecta from satellites close to planets. *Icarus* 42:422–441
31. German D, Friedlander AL (1991) A simulation of orbits around asteroids using potential field modelling. *Adv. Astron. Sci. Spacefl. Mech.* 75:1183–1201
32. Scheeres DJ (1994) Dynamics about uniformly rotating triaxial ellipsoids: applications to asteroids. *Icarus* 110:225–238
33. Rausenberger O (1888) Lehrbuch der Analytischen Mechanik I.B.G. Teubner: Leipzig
34. Werner RA (1994) The gravitational potential of a homogeneous polyhedron or don't cut corners. *Celest. Mech. Dyn. Astron.* 59:253–278
35. Werner RA, Scheeres DJ (1997) Exterior gravitation of a polyhedron derived and compared with harmonic and mascon gravitation representations of asteroid 4769 castalia. *Celest. Mech. Dyn. Astron.* 65:313–344
36. Forsberg RA (1984) Study of terrain reductions, density anomalies and geophysical inversion methods in gravity field modeling. Report of the Department of Geodetic Science and Surveying, Ohio State University
37. Petrović S (1996) Determination of the potential of homogeneous polyhedral bodies using line integrals. *J. Geodesy* 71:44–52
38. Pohánka V (1988) Optimum expression for computation of the gravity field of a homogeneous polyhedral body. *Geophys Prospect* 36:733–751
39. Tsoulis D, Petrović S (2001) On the singularities of the gravity field of a homogeneous polyhedral body. *Geophysics* 66:535–539
40. Scheeres DJ, Ostro SJ, Hudson RS et al (1996) Orbits close to asteroid 4769 Castalia. *Icarus* 121:67–87
41. Scheeres DJ, Ostro SJ, Hudson RS et al (1998) Dynamics of orbits close to asteroid 4179 Toutatis. *Icarus* 132:53–79
42. Hu W, Scheeres DJ (2004) Numerical determination of stability regions for orbital motion in uniformly rotating second degree and order gravity fields. *Planet. Space Sci.* 52:685–692
43. Wang Y, Xu S (2013) Gravity gradient torque of spacecraft orbiting asteroids. *Aircr. Eng. Aerosp. Technol.* 85:72–81
44. Antreasian PG, Helfrich CL, Miller JK et al (1998) Preliminary considerations for NEAR's low-altitude passes and landing operations at 433 Eros. In: Proceedings of the AIAA/AAS astrodynamics specialist conference and exhibit, Boston, MA, 10–12 Aug 1998
45. Bottke WF Jr, Vokrouhlický D, Rubincam DP (2002) The effect of Yarkovsky thermal forces on the dynamical evolution of asteroids and meteoroids. In: William F et al (ed) Asteroids III. University of Arizona Press, Tucson
46. Scheeres DJ, Williams BG, Miller JK (2000) Evaluation of the dynamic environment of an asteroid: applications to 433 Eros. *J. Guid. Control Dyn.* 23:466–475
47. Scheeres DJ, Gaskell R, Abe S et al (2006) The actual dynamical environment about Itokawa. In: AIAA/AAS astrodynamics specialist conference exhibit, Keystone, Colorado, Aug, pp 21–24

48. Broschart SB, Scheeres DJ (2005) Control of hovering spacecraft near small bodies: application to asteroid 25143 Itokawa. *J. Guid. Control Dyn.* 28:343–354
49. Antreasian PG, Chesley SR, Miller JK et al (2002) The design and navigation of the NEAR SHOEMAKER landing of EROS. *Adv. Astron. Sci.* 109:989–1015
50. Lantoine G, Braun RD (2006) Optimal trajectories for soft landing on asteroids. AE8900 MS Special Problems Report, Space Systems Design Lab
51. Yano H, Kubota T, Miyamoto H, Okada T et al (2006) Touchdown of the Hayabusa spacecraft at the Muses Sea on Itokawa. *Science* 312:1350–1353
52. Hawkins M, Guo Y, Wie B (2012) ZEM/ZEV Feedback guidance application to fuel-efficient orbital maneuvers around an irregular-shaped asteroid. In: Proceedings of the AIAA guidance, navigation, and control conference, Minneapolis, Minnesota, 13–16 Aug 2012
53. Bellerose J, Scheeres DJ (2008) Dynamics and control for surface exploration of small bodies. In: Proceedings of the AIAA/AAS astrodynamics specialist conference and exhibit, Honolulu, Hawaii, 18–21 Aug 2008
54. Chapman CR, Veverka J, Thomas PC (1995) Discovery and physical properties of Dactyl, a satellite of asteroid 243 Ida. *Nature* 374:783–785
55. Richardson DC, Walsh KJ (2006) Binary minor planets. *Annu. Rev. Earth Planet. Sci.* 34:47–81
56. Scheeres DJ (2002) Stability in the full two-body problem. *Celest. Mech. Dynam. Astron.* 83:155–169
57. Fahnestock EG, Scheeres DJ (2008) Simulation and analysis of the dynamics of binary near-Earth asteroid (66391) 1999 KW4. *Icarus* 194:410–435
58. Bellerose J, Scheeres DJ (2006) Periodic orbits in the full two-body problem. In: Proceedings of the AAS/AIAA conference, Tampa, Florida, United States, 22–26 Jan 2006
59. Maciejewski AJ (1995) Reduction, relative equilibria and potential in the two rigid bodies problem. *Celest. Mech. Dyn. Astron.* 63:1–28
60. Scheeres DJ (2002) Stability of binary asteroids. *Icarus* 159:271–283
61. Borderies N (1978) Mutual gravitational potential of N solid bodies. *Celest. Mech.* 18:295–307
62. Braun CV (1991) The gravitational potential of two arbitrary, rotating bodies with applications to the Earth–Moon system. University of Texas at Austin, Texas
63. Moritz H (1980) Advanced physical geodesy. Abacus Press, Wiedmann
64. Geissler P, Petit JM, Durda DD et al (1996) Erosion and ejecta reaccretion of 243 Ida and its Moon. *Icarus* 120:140–157
65. Ashenberg J (2005) Proposed method for modeling the gravitational interaction between finite bodies. *J. Guid. Control Dyn.* 28:768–774
66. Werner RA, Scheeres DJ (2005) Mutual potential of homogenous polyhedra. *Celest. Mech. Dyn. Astron.* 91:337–349
67. Fahnestock EG, Scheeres DJ, McClamroch NH et al (2005) Simulation and analysis of binary asteroid dynamics using mutual potential and potential derivatives formulation. In: Proceedings of the AAS/AIAA astrodynamics specialist conference, Lake Tahoe, CA, United States, 7–11 Aug 2005
68. Fahnestock EG, Scheeres DJ (2006) Simulation of the full two rigid body problem using polyhedral mutual potential and potential derivatives approach. *Celest. Mech. Dyn. Astron.* 96:317–339
69. Fahnestock EG, Lee T, Leok M et al (2006) Polyhedral potential and variational integrator computation of the full two body problem. In: Proceedings of the AIAA/AAS astrodynamics specialist conference, Keystone, Colorado, United States, 21–24 Aug 2006
70. Scheeres DJ, Fahnestock EG, Ostro SJ et al (2006) Dynamical configuration of binary near-Earth asteroid (66391) 1999 KW4. *Science* 314:1280–1283
71. Walsh KJ, Richardson DC, Michel P (2008) Rotational breakup as the origin of small binary asteroids. *Nature* 454:188–191
72. Holsapple K, Giblin I, Housen K (2002) Asteroid impacts: laboratory experiments and scaling laws. In: William F et al (ed) *Asteroids III*. University of Arizona Press, Tucson

73. Mantz A, Sullivan R, Veverka J (2004) Regolith transport in craters on Eros. *Icarus* 167:197–203
74. Thomas PC, Belton MJS, Carcich B et al (1996) The shape of Ida. *Icarus* 120:20–32
75. Scheeres DJ, Durda DD, Geissler PE (2002) The Fate of Asteroid Ejecta. In: William F, et al (ed) *Asteroids III*. University of Arizona Press, Tucson
76. Cheng AF, Barnouin JO, Zuber MT et al (2001) Laser altimetry of small-scale features on 433 Eros from NEAR-Shoemaker. *Science* 292:488–491
77. Weidenschilling SJ, Paolicchi P, Zappalá V (1989) Do asteroids have satellites? In: Binzel R P et al (ed) *Asteroids II*. University of Arizona Press, Tucson
78. Hamilton DP, Burns JA (1991) Orbital stability zones about asteroids. *Icarus* 92:118–131
79. Hamilton DP, Burns JA (1991) Orbital stability zones about asteroids. II. The destabilizing effects of eccentric orbits and of solar radiation. *Icarus* 96:43–64
80. Chauvineau B, Mignard F (1990) Dynamics of binary asteroids. I. Hill's Case. *Icarus* 83:360–381
81. Richter K, Keller HU (1995) On the stability of dust particle orbits around cometary nuclei. *Icarus* 114:355–371
82. Hamilton DP, Krivov AV (1997) Dynamics of distant moons of asteroids. *Icarus* 128:241–249
83. Chauvineau B, Farinella P, Mignard F (1993) Planar orbits about a triaxial body: applications to asteroidal satellites. *Icarus* 105:370–384
84. Thomas PC, Veverka J, Robinson M, Murchie S (2001) Shoemaker crater as the source of most ejecta blocks on the asteroid 433 Eros. *Nature* 413:394–396
85. Korycansky DG, Asphaug E (2004) Simulations of impact ejecta and regolith accumulation on asteroid Eros. *Icarus* 171:110–119
86. Chapman C (2004) Space weathering of asteroid surfaces. *Ann. Rev. Earth Planet. Sci.* 32:539–567
87. Durda DD, Charpman CR, Merline WJ et al (2012) Detecting crater ejecta-blanket boundaries and constraining source crater regions for boulder tracks and elongated secondary craters on Eros. *Meteorit. Planet. Sci.* 47:1087–1097
88. Bottke WF Jr, Melosh HJ (1996) Binary asteroids and the formation of doublet craters. *Icarus* 124:372–391
89. Miljković K, Collins GS, Mannick S, Bland PA (2013) Morphology and population of binary asteroid impact craters. *Earth Planet. Sci. Lett.* 363:121–132
90. Halamek P (1988) Motion in the potential of a thin bar. University of Texas at Austin, Texas
91. Arnold VI (2010) Mathematical methods of classical mechanics. Springer, New York
92. Riaguas A, Elipe A, López-Moratalla T (2001) Non-linear stability of the equilibria in the gravity field of a finite straight segment. *Celest. Mech. Dyn. Astron.* 81:235–248
93. Riaguas A, Elipe A, Lara M (1999) Periodic orbits around a massive straight segment. *Celest. Mech. Dyn. Astron.* 73:169–178
94. Liu X, Baoyin H, Ma X (2011) Periodic orbits in the gravity field of a fixed homogeneous cube. *Astrophys. Space Sci.* 334:357–364
95. Liu X, Baoyin H, Ma X (2011) Equilibria, periodic orbits around equilibria, and heteroclinic connections in the gravity field of a rotating homogeneous cube. *Astrophys. Space Sci.* 333:409–418
96. Liu X, Baoyin H, Ma X (2013) Dynamics of surface motion on a rotating massive homogeneous body. *Sci. China Phys. Mech. Astron.* 56:818–829
97. Ostro SJ, Hudson RS, Benner LAM (2002) Asteroid radar astronomy. In: William F et al (ed) *Asteroids III*. University of Arizona Press, Tucson
98. Kammeyer PC (1978) Periodic orbits around a rotating ellipsoid. *Celest. Mech.* 17:37–48
99. Yu Y, Baoyin H (2012) Orbital dynamics in the vicinity of asteroid 216 Kleopatra. *Astron. J.* 143:62–71
100. Yu Y, Baoyin H (2013) Resonant orbits in the vicinity of asteroid 216 Kleopatra. *Astrophys. Space Sci.* 343:75–82
101. Yu Y, Baoyin H (2012) Generating families of 3D periodic orbits about asteroids. *Mon. Not. Royal Astron. Soc.* 427:872–881

102. Arnold VI (2006) In: Qi M (ed) Mathematical methods of classical mechanics, 4th edn. Higher Education Press, Beijing, pp iii–v (Trans.)
103. Gutiérrez-Romero S, Palacín JF, Yanguas P (2004) The invariant manifolds of a finite straight segment. Monografías de la Real Academia de Ciencias de Zaragoza 25:137–148
104. Jiang Y, Baoyin H, Li J, Li H (2014) Orbits and manifolds near the equilibrium points around a rotating asteroid. *Astrophys. Space Sci.* 349:83–106
105. Maruskin JM, Scheeres DJ, Bloch AM (2009) Dynamics of symplectic subvolumes. *Siam J. Appl. Dyn. Syst.* 8:180–201
106. Tsuda Y, Scheeres DJ (2009) Computation and applications of an orbital dynamics symplectic state transition matrix. *J. Guid. Control Dyn.* 32:1111–1123

# Chapter 2

## Modelling Orbital Dynamics in the Potential of Small Bodies

**Abstract** The research of orbital dynamics highly relies on the preliminary modelling work of target system, and an appropriate model comes from full understanding of the physics of the system. Two remarkable features of the dynamics problem around a small body should be noticed: first, the influences of different kinds of perturbations become relatively strong since the gravity from the small body is usually weak; second, the gravitational field of a real asteroid could be geometrically complex due to its irregular shape. Starting from these two points, this chapter discusses the modelling issues of orbital dynamics around a small body. An analysis of the perturbation magnitudes is presented first, and then described is the numeric methods to approximate the gravity from a small body. We compare these methods and show the advantages and disadvantages, respectively. Section 2.4 discusses about the orbital equations in the gravitational field of a small body. The basic form of the equation is first presented with the potential described by a homogenous polyhedron, and several transformations are listed to identify the general properties of this kind of systems, which is taken as the beginning to understand the following chapters. Section 2.5 deduces the unitless form of the motion equations and proposes a basic dynamical factor  $\kappa$ . Through qualitative analysis and numerical verifications of specific asteroids, we show this factor has a crucial influence on the global scheme of the orbital behaviors. Reference values of  $\kappa$  are listed for some real Solar System small bodies.

**Keywords** Extended body · Gravity · Reference systems · Integrability · Hamiltonian systems · Planets and satellites · Fundamental parameters

### 2.1 Introduction

The research of orbital dynamics highly relies on the preliminary modelling work of target system, and an appropriate model comes from full understanding of the physics of the system. Two remarkable features of the dynamics problem around an small body should be noticed: first, the influences of different kinds of perturbations become relatively strong since the gravity from the small body is usually weak;

second, the gravitational field of a real asteroid could be geometrically complex due to its irregular shape. Starting from these two points, this chapter discusses the modelling issues of orbital dynamics around a small body. An analysis of the perturbation magnitudes is presented first, and then described is the numeric methods to approximate the gravity from a small body. We compare these methods and show the advantages and disadvantages, respectively.

Section 2.4 discusses about the orbital equations in the gravitational field of a small body. The basic form of the equation is first presented with the potential described by a homogenous polyhedron, and several transformations are listed to identify the general properties of this kind of systems, which is taken as the beginning to understand the following chapters.

Section 2.5 deduces the unitless form of the motion equations and proposes a basic dynamical factor  $\kappa$ . Through qualitative analysis and numerical verifications of specific asteroids, we show this factor has a crucial influence on the global scheme of the orbital behaviours. Reference values of  $\kappa$  are listed for some real Solar System small bodies.

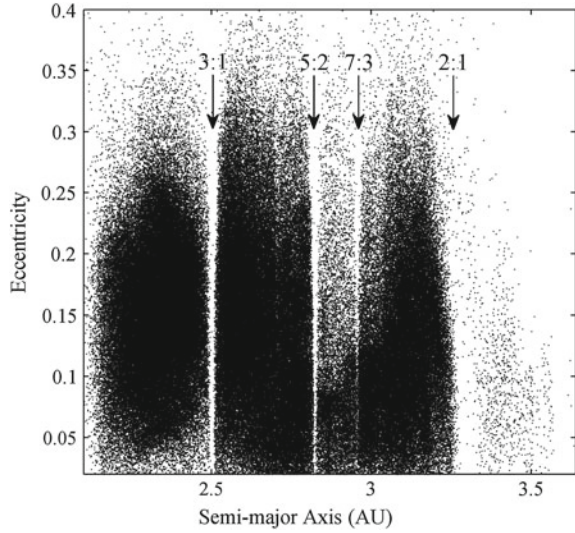
## 2.2 Mechanical Environment in the Vicinity of Small Bodies

About 90 % of known small bodies locate at the main asteroid belt which is roughly between the orbits of the planets Mars and Jupiter,  $2.17 \sim 3.64$  AU away from the Sun. A major part of remained 10 % small bodies belong to near-Earth objects (NEOs), which are widely concerned because of their potential hazard to the Earth. NEA observing plans like Lincoln Near-Earth Asteroid Research (LINEAR) and Near-Earth Asteroid Tracking (NEAT) have monitored these small bodies for long terms [1]. According to the orbital features, NEAs are generally divided into three categories: Amor asteroids, whose orbits approach but do not cross Earth orbit, and whose orbits are further from the Sun than Earth's orbit (e.g., Eros); Apollo asteroids, whose orbits cross Earth's orbit, within Mars' orbit, and some of which have high eccentricities (e.g., 1892 Apollo); Aten asteroids, whose orbits also cross Earth's orbit, but unlike Apollos, Atens spend most of their time inside Earth orbit (e.g., 2062 Aten).

Since the number of Solar System small bodies is tremendous, their orbits are widely distributed, we are in lack of knowledge about the real spatial environment around them to date. Among the known perturbations, the gravitational perturbations from the Sun and planets, the solar radiation pressure and collisions from ejected debris and dust (from meteorite impacts) may have significant effects on the short-term motion of spacecraft. This section will not involve the influence of ejecta collision due to its randomness and uncertainty. Rather, we pay attention to more general perturbation forms, the third-body gravitational perturbation and solar radiation pressure.

The research on the effects of planetary gravity can date back to 1866, when American astronomer Kirkwood found the narrow gaps in the distribution of the

**Fig. 2.1** The semi-major axis distribution of main-belt asteroids and Kirkwood gaps



semi-major axis of the orbits of main-belt asteroids (named Kirkwood Gap) [2], as illustrated in Fig. 2.1. These gaps are resulted from the orbital resonances with Jupiter, which has cleared the asteroids out of these regions over a long term. All asteroids with orbital distances that form a simple ratio with that of Jupiter will be affected by such gravitational perturbations, e.g., the gaps occur at the 2:1, 3:1, 5:2 and 7:3 orbital resonances.

Similarly, the 1:1 resonance with Jupiter leads to a clearance effect on the objects running on its orbit, which are finally concentrated around the  $L_4$ ,  $L_5$  Lagrange points of Sun–Jupiter system, called Jupiter Trojan asteroids. Accordingly, Trojans have also been found at the  $L_4$ ,  $L_5$  of Earth, Mars and Uranus. Thus the effects of orbital resonance could be significant from a secular perspective, while in the work of this thesis, the time span of our concern is much shorter (days to months). Reference [3] confirmed the solar tide is the major perturbation in our case, and the planetary influence can be ignored for the study of short-term motion.

The acceleration of a mass point orbiting around a small body can be represented as

$$\frac{d^2}{dt^2} \mathbf{r} \approx \mathbf{a} + \mathbf{a}_s + \mathbf{a}_{\odot}, \quad (2.1)$$

where  $\mathbf{r}$  indicates the position vector of the mass point,  $\mathbf{a}$  indicates the gravitational acceleration from the small body,  $\mathbf{a}_s$  indicates the acceleration of solar radiation pressure, and  $\mathbf{a}_{\odot}$  indicates the solar tidal acceleration. Equation 2.1 presents two major forms of perturbations, solar radiation pressure and solar tide. We will analysis the order of magnitudes of these perturbations. Formula 2.2 presents the general definition of the radius of influential sphere of a small body.

$$R = D \left( \frac{M_A}{M_\odot} \right)^\alpha, \quad (2.2)$$

in which,  $D$  is the mean distance from the small body to the Sun,  $M_A$ ,  $M_\odot$  are the masses of the small body and the Sun, respectively. The exponent parameter  $\alpha$  discriminates the boundaries of these spherical regions. Equation 2.3 gives three common ways to define the radius  $R$ :  $\alpha = 1/3$  corresponds to  $R_1$ , which is like the definition of Hill Sphere, meaning the magnitude of the solar tide equals to the small body's gravity at the boundary;  $\alpha = 2/5$  corresponds to  $R_2$ , which is the classical definition of Sphere of Influence in astrodynamics, describes the boundary of the region in which the dominant gravity on an orbiting object is from the small body;  $\alpha = 1/2$  corresponds to  $R_3$ , which means the magnitude of the solar gravity equals to that from the small body at the boundary.

$$R = \begin{cases} R_1 & \alpha = 1/3 \\ R_2 & \alpha = 2/5 \\ R_3 & \alpha = 1/2 \end{cases} \quad (2.3)$$

According to Eq. 2.3,  $R_1 > R_2 > R_3$ . Table 2.1 lists the values of these three radii for 23 asteroids with the latest mass information. The maximum radius  $R_1$  is usually hundreds of times than the size of the asteroid, and the minimum radius  $R_3$  is only tens of times, which is a strict estimation of the range dominated by the asteroid.

Hamilton et al. studied the orbital stability of natural satellites of the small bodies, and suggested that Hill radius can be used to estimate the region where a satellite might exist, i.e., the asteroidal gravity dominates the orbital motion within this region [3]. We compare the magnitudes of solar tide and solar radiation pressure at the boundaries of the spherical regions defined above. Equation 2.4 presents the dimensionless solar tide and solar radiation pressure, scaled by the asteroidal gravity. Combining Eq. 2.2, the scaled perturbations depend on the mass ratio of the small body and the Sun like

$$\begin{aligned} a_s/a &\approx \beta \frac{GM_\odot}{D^2} / \frac{GM_A}{R^2} = \beta \left( \frac{M_A}{M_\odot} \right)^{2\alpha-1}, \\ a_\odot/a &\approx \frac{R}{D} \frac{GM_\odot}{D^2} / \frac{GM_A}{R^2} = \left( \frac{M_A}{M_\odot} \right)^{3\alpha-1}. \end{aligned} \quad (2.4)$$

In which  $a$ ,  $a_s$ ,  $a_\odot$  indicate the magnitudes of  $\mathbf{a}$ ,  $\mathbf{a}_s$ ,  $\mathbf{a}_\odot$ , respectively.  $\beta$  is the ratio of the radiation pressure force to the gravitational force of the Sun [4], and in our analysis, we only need to apply the general magnitude of  $\beta$  for a spacecraft. According to Ref. [5], we adopt  $\beta = 3.37 \times 10^{-4}$ . The scaled mass of known small bodies  $M_A/M_\odot$  ranges from  $5.03 \times 10^{-21}$  to  $4.74 \times 10^{-10}$  due to Table 2.1. Figure 2.2 shows the magnitudes of scaled solar tide (a) and solar radiation pressure (b) over this range at  $R_1$ ,  $R_2$  and  $R_3$ , respectively. The value above  $10^0$  indicates the perturbation is greater than the gravity, and that below  $10^0$  indicates the perturbation is smaller

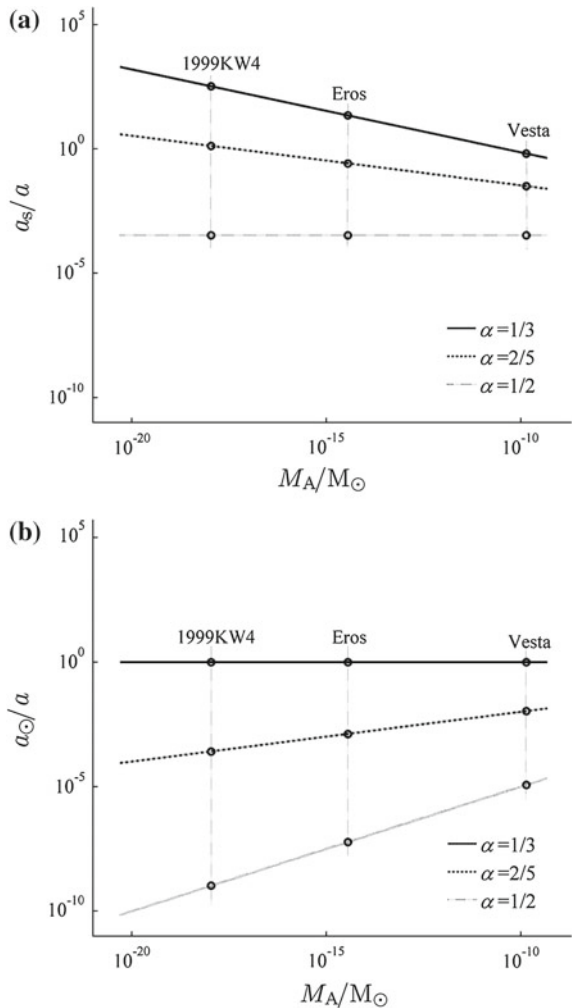
**Table 2.1** The values of  $R_1$ ,  $R_2$  and  $R_3$  for some asteroids

Asteroid	$M_A/M_\odot$	$R_1$ (km)	$R_2$ (km)	$R_3$ (km)
1 Ceres	$4.81 \times 10^{-10}$	$2.25 \times 10^5$	$7.77 \times 10^4$	$9.09 \times 10^3$
2 Pallas	$1.00 \times 10^{-10}$	$1.33 \times 10^5$	$4.15 \times 10^4$	$4.15 \times 10^3$
4 Vesta	$1.38 \times 10^{-10}$	$1.27 \times 10^5$	$4.02 \times 10^4$	$4.15 \times 10^3$
10 Hygiea	$5.60 \times 10^{-11}$	$1.25 \times 10^5$	$3.72 \times 10^4$	$3.51 \times 10^3$
11 Parthenope	$2.56 \times 10^{-12}$	$3.48 \times 10^4$	$8.47 \times 10^3$	$5.87 \times 10^2$
15 Eunomia	$1.20 \times 10^{-11}$	$6.27 \times 10^4$	$1.69 \times 10^4$	$1.37 \times 10^3$
16 Psyche	$9.00 \times 10^{-12}$	$6.30 \times 10^4$	$1.67 \times 10^4$	$1.31 \times 10^3$
20 Massalia	$2.44 \times 10^{-12}$	$3.36 \times 10^4$	$8.16 \times 10^3$	$5.63 \times 10^2$
45 Eugenia	$3.00 \times 10^{-12}$	$4.07 \times 10^4$	$1.00 \times 10^4$	$7.05 \times 10^2$
52 Europa	$2.60 \times 10^{-11}$	$9.52 \times 10^4$	$2.70 \times 10^4$	$2.36 \times 10^3$
87 Sylvia	$7.60 \times 10^{-12}$	$7.13 \times 10^4$	$1.87 \times 10^4$	$1.44 \times 10^3$
88 Thisbe	$7.00 \times 10^{-12}$	$5.49 \times 10^4$	$1.43 \times 10^4$	$1.10 \times 10^3$
90 Antiope	$4.14 \times 10^{-13}$	$2.44 \times 10^4$	$5.27 \times 10^3$	$3.04 \times 10^2$
121 Hermione	$4.70 \times 10^{-12}$	$5.99 \times 10^4$	$1.52 \times 10^4$	$1.12 \times 10^3$
216 Kleopatra	$2.33 \times 10^{-12}$	$1.98 \times 10^4$	$3.33 \times 10^3$	$2.28 \times 10^3$
243 Ida	$2.20 \times 10^{-14}$	$8.32 \times 10^3$	$1.47 \times 10^3$	$6.35 \times 10^1$
253 Mathilde	$5.19 \times 10^{-14}$	$1.02 \times 10^4$	$1.92 \times 10^3$	$9.02 \times 10^1$
433 Eros	$3.60 \times 10^{-15}$	$2.32 \times 10^3$	$3.64 \times 10^2$	$1.31 \times 10^1$
444 Gyptis	$4.00 \times 10^{-12}$	$4.56 \times 10^4$	$1.14 \times 10^4$	$8.29 \times 10^2$
511 Davida	$5.60 \times 10^{-11}$	$1.26 \times 10^5$	$3.75 \times 10^4$	$3.54 \times 10^3$
704 Interamnia	$3.50 \times 10^{-11}$	$1.04 \times 10^5$	$3.01 \times 10^4$	$2.71 \times 10^3$
762 Pulcova	$1.28 \times 10^{-12}$	$3.56 \times 10^4$	$8.26 \times 10^3$	$5.34 \times 10^2$
766391 1999KW4	$1.10 \times 10^{-18}$	$6.88 \times 10^1$	$6.30 \times 10^0$	$1.01 \times 10^{-1}$

than the gravity. To make sense of the variation of perturbations with the mass, three typical asteroids are marked on the curves in Fig. 2.2, including Vesta ( $\sim 525.4$  km), Eros ( $\sim 16.8$  km) and 1999KW4 ( $\sim 1.4$  km).

Figure 2.2 shows both solar radiation pressure and solar tide can not be neglected for the study of orbital motion beyond  $R_1$ , when the former is greater than the gravity, and the latter is equivalent with the gravity. And at a distance of  $R_2$ , solar tide is ignorable, and the relative effect of solar radiation pressure depends on the mass of small body: it is ignorable for big objects like Vesta, and considerable for smaller ones like Eros. At a distance of  $R_3$ , the solar tide perturbation is smaller than that of solar radiation pressure, which is much smaller than the gravity. Therefore, we confirm the gravity of the small body is the dominant force governing the motion within the spherical region of radius  $R_3$  (usually tens of the small body's diameter), when the perturbations of solar tide and solar radiation pressure are negligible for short-term orbital motion.

**Fig. 2.2** The magnitudes of scaled perturbations varying as the mass of the small body. **a** Solar radiation pressure. **b** Solar tide



### 2.3 Descriptions of the Gravitational Field

Solar system small bodies are composed of meteorite material, and their masses are usually small so that the gravity is quite weak, which is insufficient to maintain a spherical overall shape against the interior strength. Thus differing from planets, small bodies are various in shape and most of them have irregular outlooks and pockmarks on the surface due to meteorite impacts (Fig. 2.3). Besides, the interior structures of the small bodies, as well as the surface landforms, have also been modified by different kinds of weathering mechanisms in space. It is an established fact that most asteroids have “rubble pile” structures, i.e. aggregates of rocks gathered

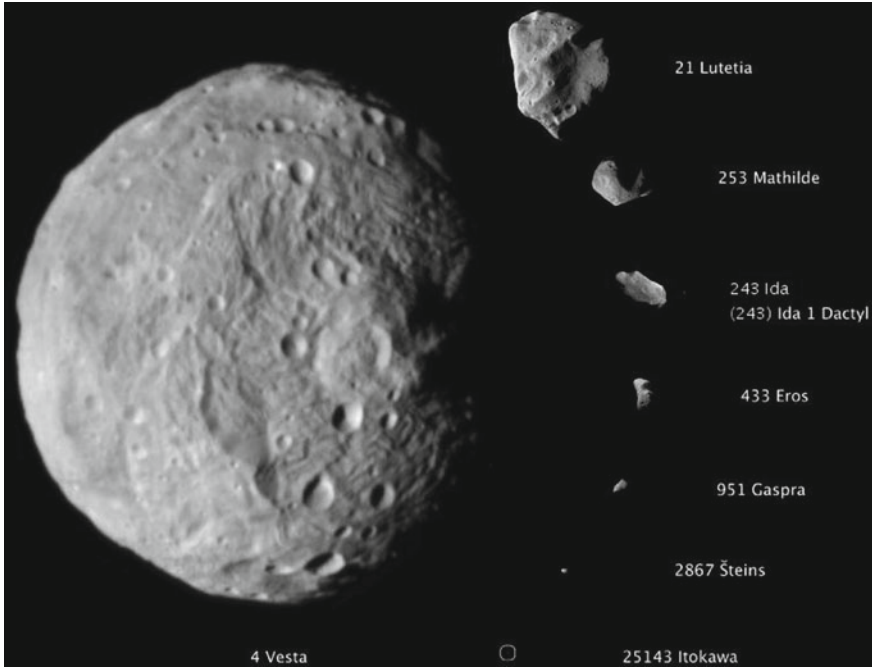


**Fig. 2.3** Some small bodies with images of high resolution (scaled in equal proportion). Reprinted from Ref. [6], copyright 2015 by NASA

only by their mutual gravities. All these matters contribute to asymmetric and irregular gravitational field around the small bodies, therefore to choose an appropriate method to describe the gravity is a crucial work for the study orbital dynamics near the small bodies.

### 2.3.1 Mass Point Cluster

Mass point cluster (also known as “mascon”) is a direct method to approximate the gravitational field of arbitrary object. According to this method, a small body is discretised into a series of voxels, and the gravity/potential from each of these voxels can be estimated using a mass point locating at its centre. Then the sum of the unit gravity/potential from all voxels will be taken as the result from the target object.

Particularly, consider a division of  $N$  voxels.  $\mathbf{d}_i, M_i$  indicate the position and the mass of  $i$ th voxel, respectively. The gravitational acceleration from the target body can be represented as

$$\mathbf{a} = \sum_{i=1}^N \frac{GM_i(\mathbf{r} - \mathbf{d}_i)}{|\mathbf{r} - \mathbf{d}_i|^3}, \quad (2.5)$$

where the voxel mass  $M_i$  subject to

$$\sum_{i=1}^N M_i = M_A, \quad (2.6)$$

and the gravitational potential from the unit voxel is

$$U = \sum_{i=1}^N \frac{GM_i}{|\mathbf{r} - \mathbf{r}_i|}. \quad (2.7)$$

The method of mass point cluster has several obvious advantages. First, the algorithm is simple and operable; and second, its convergence is evident that the approximate accuracy increases as the number of voxels  $N$  [7]; third, this method is quite portable to the real states of an asteroid, e.g. for asteroids of rubble pile interiors, the arrangement of the voxels in the cluster can be alternated with a meshless scheme, and the mass of the voxels  $M_i$  can be conveniently modified to fit the nonuniform distribution of the density of a real small body.

Figure 2.4 shows the stated advantages with an example solid ellipsoid of triaxial ratio 0.8:1.0:0.4 (a). A uniform division of about 1,000 equal-sized spherical voxels is shown in Fig. 2.4b, which is achieved using hexagonal close packing, i.e. a pattern of the best space utilization rate for equal-sized spheres. Figure 2.4c shows a division of bimodal-sized spherical voxels in meshless packing which is achieved by randomly piling these spheres up in a natural way.

The method of mass point cluster has been successfully applied to the analysis of binary motion, and Llanos et al. applied it to their studies of an ESA sampling mission concept, which involves the hovering control of spacecraft near the target asteroid 341843 2008EV5 based on a gravitational field model.

In spite of the great potential in applications, the method of mass point cluster does not perfectly fit for our problem: first, the convergence of this method is quite slow, and the calculated amount increases rapidly as the voxel number of the division; second, Eqs. 2.5 and 2.7 indicate great cumulated errors for the terms within the sum, which could be another obstacle during practical calculation; third, as the study of orbital motion near a small body, an issue that cannot be avoided is collision detection, which is to find out whether the object has entered inside the body, however, this method provides no efficient information about that, and a collisional routine must be employed in parallel, which will cost computational wastes.

### 2.3.2 Spherical/Ellipsoidal Harmonics

The method of spherical harmonics is mature and efficient in describing the gravitational field of planets, which is widely used in the study of orbital dynamics

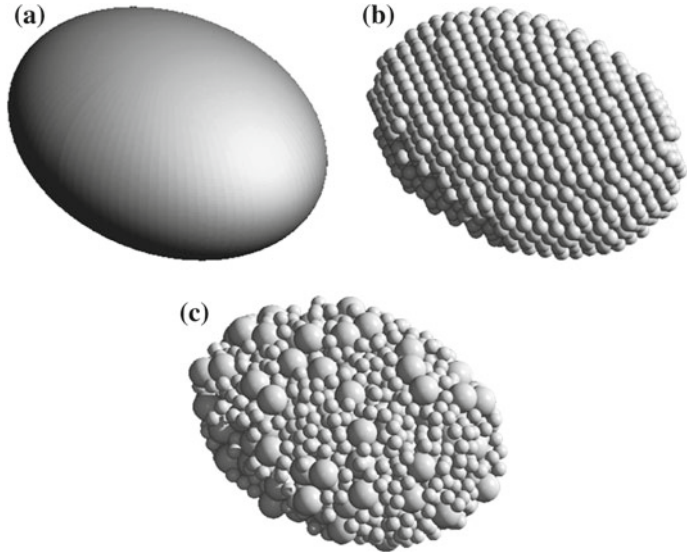


**Fig. 2.4** Divisions to an ellipsoid with the method of mass point cluster. **a** Solid triaxial ellipsoid. **b** Uniform division of equal-sized voxels. **c** Meshless division of bimodal-sized voxels

of man-made satellite. As a general approach, it also applies to the non-spherical perturbations of gravitational field around a small body. Equation 2.8 presents the expansion of the potential at a massless mass point by spherical harmonics.

$$U = \frac{GM_A}{r} \left\{ 1 + \sum_{n=1}^{\infty} \sum_{m=0}^n \left( \frac{r_e}{r} \right)^n P_{nm}(\sin\varphi) [C_{nm} \cos m\lambda + S_{nm} \sin m\lambda] \right\}, \quad (2.8)$$

in which  $r$ ,  $\varphi$  and  $\lambda$  are the spherical coordinates of the mass point,  $P_{nm}$  indicate associated Legendre polynomials, and  $C_{nm}$ ,  $S_{nm}$  are the coefficients of spherical harmonics, representing the non-spherical terms of the gravitational field.  $r_e$  indicates the radius of the reference sphere, defining the convergence domain, i.e. Eq. 2.8 fails inside the reference sphere. Since there is no explicit expression of the mass distribution inside the small body, the coefficients  $C_{nm}$  and  $S_{nm}$  can not be derived directly by integration. The estimation of these coefficients is the major part of gravitational field modelling, and the common approaches involve inversion from the flight data and approximation through the body's shape and density.

The method of ellipsoidal harmonics is an improved version of the spherical harmonics, aiming at better approximation to the irregular gravitational fields. Equation 2.9 presents the expansion of the potential at a massless mass point by ellipsoidal harmonics.

$$U = GM_A \sum_{n=0}^{\infty} \sum_{m=1}^{2n+1} \alpha_{nm} \frac{F_{nm}(\lambda_1)}{F_{nm}(\lambda_e)} F_{nm}(\lambda_2) F_{nm}(\lambda_3), \quad (2.9)$$

where  $\lambda_1, \lambda_2, \lambda_3$  are orthogonal ellipsoidal coordinates [8],  $\lambda_e$  indicates the reference ellipsoid (or Brillouin ellipsoid), which defines the convergence domain of Eq. 2.9.  $F_{nm}$  are the canonical solutions to Lamé equation, which are continuous functions when  $\lambda_1 \geq \lambda_e$ .  $\alpha_{nm}$  indicate ellipsoidal coefficients. The corresponding gravity forms of these two methods are determined by gradients of Eqs. 2.8 and 2.9, respectively.

Figure 2.5 illustrates a comparison between the convergence domains of these two methods about asteroid Castalia. Since Castalia has a dumbbell-like shape, Fig. 2.5a shows the reference sphere employed in the spherical harmonics, which excludes a large area around Castalia that may be traversed by the orbits; and Fig. 2.5b shows the reference ellipsoid, which fits the overall shape of Castalia better and widens the convergence domain of the gravitational formulas.

As shown in Fig. 2.5, the method of ellipsoidal harmonics has some sort of advantage in describing the gravitational field of a small body, and it has been successfully applied to fitting the gravity data of Eros returned by NEAR Shoemaker [9], and the method of spherical harmonics, which is usually used together with the polyhedral method (see Sect. 2.3.3), works well for the orbital segments far from the small body and is efficient in computing. While a common disadvantage of the methods of harmonics is the convergence that depends on the distance away from the central body, i.e. the closer to the boundary of convergence domain, the lower the approximating precision becomes. This essentially affects the global accuracy of this type of methods, because the close approaches to the small body is hard to avoid in our study of orbital dynamics. Besides, similarly as the mass point cluster, the methods of harmonics provide no clues to collision detection, and to make it work, a parallel collisional routine will be necessary.

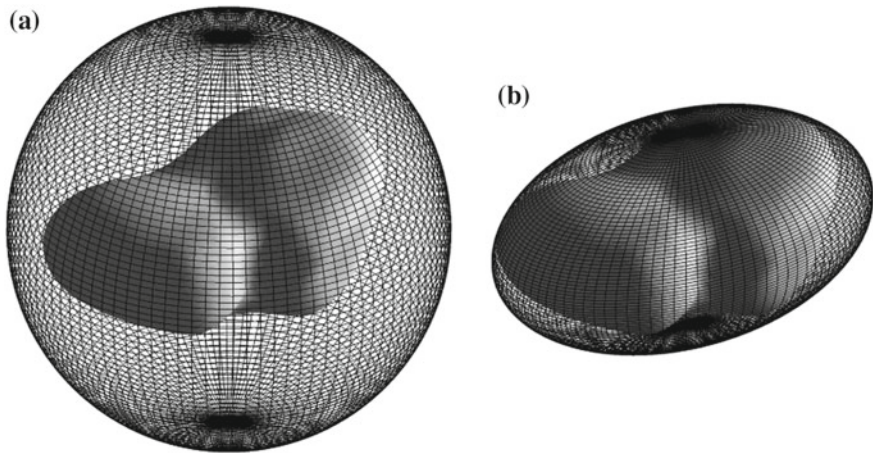


**Fig. 2.5** The reference sphere and ellipsoid about asteroid 4769 Castalia. **a** Reference sphere of spherical harmonics. **b** Reference ellipsoid of ellipsoidal harmonics

### 2.3.3 Polyhedral Method

The polyhedral method applied in geological modelling can date back to the early time, but it was only applied in describing the small body's shape and calculating the gravity as late as twenty-nineties. Werner et al. derived the expressions of the gravitational potential, attraction and gradient matrix of a homogenous polyhedron based on dyads of the second order [10], which is known as the classic polyhedral method to describe the irregular gravitational field of a small body, and we take it as the major tool to construct the field model of the target small body in this thesis.

The rest of this section will present some fundamentals of the polyhedral method, in order to construct the gravitational model of a small body. Figure 2.6 shows a tetrahedron as the simplest example of arbitrary polyhedron P of a uniform bulk density  $\sigma$ . The potential induced by P at any position of its exterior  $\mathbf{r}$  is

$$U = G\sigma \iiint_P \frac{1}{r} dV. \quad (2.10)$$

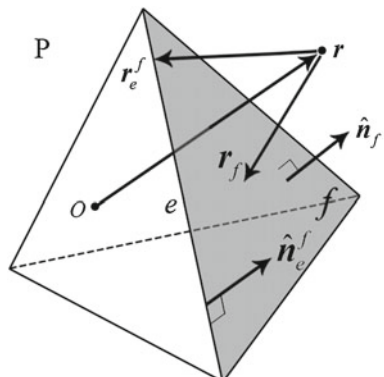
By applying Gaussian divergence theorem to Eq. 2.10, we have Eq. 2.11.

$$U = \frac{1}{2}G\sigma \sum_{f \in FS} \hat{\mathbf{n}}_f \cdot \mathbf{r}_f \iint_f \frac{1}{r} dS, \quad (2.11)$$

where  $\hat{\mathbf{n}}_f$  is the outward normal vector of facet  $f$ , as shown in Fig. 2.6, and the hat symbol  $\hat{\cdot}$  indicates a unit vector in this thesis.  $\mathbf{r}_f$  indicates the vector from  $\mathbf{r}$  to any point on the facet  $f$ , and  $FS$  indicates the set of all facets of P. Then the areal integral term in Eq. 2.11 can be written as

$$\iint_f \frac{1}{r} dS = \sum_{e \in ES_f} L_e^f \mathbf{r}_e^f \cdot \hat{\mathbf{n}}_e^f - \theta_f \hat{\mathbf{n}}_f \cdot \mathbf{r}_f, \quad (2.12)$$

**Fig. 2.6** The tetrahedron as an example of the polyhedral method



in which  $L_e^f$  indicates the line integral term about the edge  $e$  of facet  $f$ ,  $\theta_f$  is the solid angle corresponding to facet  $f$  whose sign is defined as:  $\theta_f > 0$  if  $\mathbf{r}_f \cdot \mathbf{n}_f < 0$ ;  $\theta_f = 0$  if  $\mathbf{r}_f \cdot \mathbf{n}_f = 0$ ;  $\theta_f < 0$  if  $\mathbf{r}_f \cdot \mathbf{n}_f > 0$ . Besides,  $\mathbf{r}_e^f$  indicates the vector from  $\mathbf{r}$  to any point on the edge  $e$ , and  $\hat{\mathbf{n}}_e^f$  indicates the outwarding unit vector of edge  $e$ , lying inside the plane of facet  $f$ .  $ES_f$  is the set of the all edges of facet  $f$ . Then substituting Eq. 2.12 into Eq. 2.11, we have

$$U = \frac{1}{2}G\sigma \sum_{f \in FS} \sum_{e \in ES_f} L_e^f \mathbf{r}_f \cdot \hat{\mathbf{n}}_f \hat{\mathbf{n}}_e^f \cdot \mathbf{r}_e^f - \frac{1}{2}G\sigma \sum_{f \in FS} \theta_f \mathbf{r}_f \cdot \hat{\mathbf{n}}_f \hat{\mathbf{n}}_f \cdot \mathbf{r}_f. \quad (2.13)$$

Equation 2.13 can be simplified by reducing the terms of common edges of adjacent facets. For instance,  $e$  is the common edge of facet  $f_1$  and facet  $f_2$ . By introducing the dyad  $\mathbf{E}_e = \hat{\mathbf{n}}_{f_1} \hat{\mathbf{n}}_e^{f_1} + \hat{\mathbf{n}}_{f_2} \hat{\mathbf{n}}_e^{f_2}$  and the dyad  $\mathbf{F}_f = \hat{\mathbf{n}}_f \hat{\mathbf{n}}_f$ , and by noticing  $L_e^{f_1} = L_e^{f_2}$  (unified as  $L_e$ ) and  $\mathbf{r}_f \cdot \hat{\mathbf{n}}_f = \mathbf{r}_e^f \cdot \hat{\mathbf{n}}_f$ , Eq. 2.13 turns into

$$U = \frac{1}{2}G\sigma \left( \sum_{e \in ES} L_e \mathbf{r}_e \cdot \mathbf{E}_e \cdot \mathbf{r}_e - \sum_{f \in FS} \theta_f \mathbf{r}_f \cdot \mathbf{F}_f \cdot \mathbf{r}_f \right), \quad (2.14)$$

in which  $ES$  indicates the set of all edges of the polyhedron  $P$ . Equation 2.14 presents a closed form of the potential in the exterior of  $P$ , and accordingly the gradient and gradient tensor of Eq. 2.14 determine the gravity and its gradient matrix, respectively, as shown in Eqs. 2.15 and 2.16 (see Ref. [10] for more details).

$$\nabla U = -G\sigma \left( \sum_{e \in ES} L_e \mathbf{E}_e \cdot \mathbf{r}_e - \sum_{f \in FS} \theta_f \mathbf{F}_f \cdot \mathbf{r}_f \right), \quad (2.15)$$

$$\nabla \nabla U = G\sigma \left( \sum_{e \in ES} L_e \mathbf{E}_e - \sum_{f \in FS} \theta_f \mathbf{F}_f \right). \quad (2.16)$$

The advantages of polyhedral method are obvious: first, the closed forms of Eqs. 2.14–2.16 avoid truncation errors during the computing, i.e. the major part of the errors comes from modelling precess (e.g., the bias of estimation for the shape and density distribution), and the accuracy of the polyhedral method is compatible with the resolution of the polyhedron employed as the shape model; second, differing from the methods of harmonics, the approximating precession of polyhedral method does not depend on the distance away from the small body, which is uniformly effective at places even close to the polyhedron; third, this method enables a quick and convenient judgement of whether a point has entered the interior of a polyhedron  $P$ , i.e. recalling the sum of all solid angles  $\Omega$  as defined in Eq. 2.17, the position of the point  $\mathbf{r}$  lies inside  $P$  if  $\Omega = 4\pi$ , else  $\Omega = 0$ .

$$\mathcal{Q} = \sum_{f \in FS} \theta_f. \quad (2.17)$$

In addition, the polyhedral method based on the target's shape is well suited to the practical mission, that during the approaching segment, the shape model of target small body is obtained firstly by optical measurement, based on which a preliminary gravity model can be built using this method. This model will contribute to the early approaching operations, which are of high risks since the dynamical environment has not been well understood. Then the flight data of the spacecraft will be analyzed, tending to build a more accurate gravity model.

We prefer the polyhedral method and take it as the major methodology in this study because it can provide good approximation close to the surface of an irregular body. However, it is notable the advantage is not unique, e.g. the methods of harmonics could be much more computationally efficient than the polyhedral method when the spacecraft is far away from the target body (say tens of times of its radius).

## 2.4 Motion Equations

The motion equations of a test mass point in the vicinity of a small body (within radius  $R_3$ ) are given in this section, considering the irregular gravitational field calculated with the polyhedral method. The vectors of the small body's angular velocity and acceleration are denoted by  $\omega$  and  $\alpha$ , respectively, and frames are defined as follows (Fig. 2.7):

1. Mass centre inertia frame  $OXYZ$ : a translational frame with the origin at the mass centre of the small body  $O$ , axis  $X$  pointing at J2000 mean equinox,  $XY$  plane parallel with the Earth's orbital plane, and axes  $Z$ ,  $Y$ ,  $X$  forming a right-handed system.
2. Mass centre body-fixed frame  $Oxyz$ : the origin locates at the mass centre  $O$ , and axes  $x$ ,  $y$ ,  $z$  indicate the principal axes of minimum, medium, maximum inertia, respectively, forming a right-handed system.

Considering a massless point, i.e. the gravity from the mass point has no influence on the small body, the motion equation of the mass point is

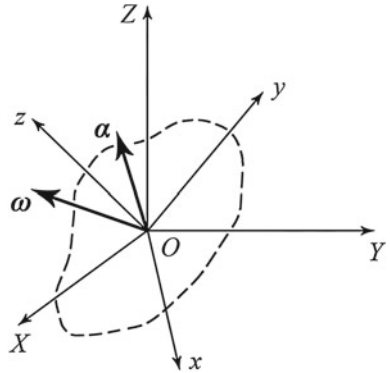
$$\frac{d^2}{dt^2} \mathbf{r} = -\nabla U. \quad (2.18)$$

Then the left hand side of Eq. 2.18 represented in relative derivatives yields

$$\ddot{\mathbf{r}} + 2\omega \times \dot{\mathbf{r}} + \omega \times (\omega \times \mathbf{r}) + \alpha \times \mathbf{r} = -\nabla U, \quad (2.19)$$

where “ $d/dt$ ” indicates the absolute derivative about time  $t$ , and “ $\cdot\cdot$ ” indicates the relative derivative about  $t$ . Furthermore, most of the small bodies are supposed to be

**Fig. 2.7** The frames and rotational vectors of a small body



rotating around the principal axis, and the variation of angular velocity is quite slow [11]. Approximately we assume  $\alpha = 0$ , Eq. 2.19 turns into

$$\ddot{\mathbf{r}} + 2\boldsymbol{\omega} \times \dot{\mathbf{r}} + \boldsymbol{\omega} \times (\boldsymbol{\omega} \times \mathbf{r}) = -\nabla U, \quad (2.20)$$

Defining the efficient potential of a rotating body Eq. 2.21, we have a simplified form of the motion equation Eq. 2.22.

$$V = -\frac{1}{2}(\boldsymbol{\omega} \times \mathbf{r}) \cdot (\boldsymbol{\omega} \times \mathbf{r}) + U, \quad (2.21)$$

$$\ddot{\mathbf{r}} + 2\boldsymbol{\omega} \times \dot{\mathbf{r}} = -\nabla V. \quad (2.22)$$

Equation 2.22 describes a complete system, including a Coriolis force term and a potential force term, which is apparently also a conserved system. Define a state variable  $\mathbf{x}$  (Eq. 2.23), Eq. 2.22 is restated in a general form Eq. 2.24.

$$\mathbf{x} = \begin{bmatrix} \mathbf{r} \\ \dot{\mathbf{r}} \end{bmatrix}, \quad (2.23)$$

$$\dot{\mathbf{x}} = f(\mathbf{x}). \quad (2.24)$$

Introducing the canonical variables  $\mathbf{q} = \mathbf{r}$ ,  $\mathbf{p} = \boldsymbol{\omega} \times \mathbf{r} + \dot{\mathbf{r}}$ , the Hamiltonian form of system Eq. 2.24 is derived using Legendre transformation [12]:

$$\mathbf{q} = \frac{\partial H}{\partial \mathbf{p}}, \quad \mathbf{p} = -\frac{\partial H}{\partial \mathbf{q}}, \quad (2.25)$$

in which  $H$  is the Hamiltonian function

$$H = \frac{1}{2}\mathbf{p} \cdot \mathbf{p} - (\boldsymbol{\omega} \times \mathbf{q}) \cdot \mathbf{p} + U. \quad (2.26)$$

The Hamiltonian function is independent on time  $t$  (Eq. 2.27), thus it determines a general energy integral  $C$ , called Jacobi integral.

$$\frac{d}{dt} H = 0. \quad (2.27)$$

The symplectic structure of system Eq. 2.25 forms the basis of understanding the orbital behaviours around the small body

1. Equation 2.25 has only one first integral  $C$  and has no cyclic coordinates;
2. Liouville theorem ensures the invariance of the infinitesimal phase space volume, namely there is no asymptotic behaviours in the flow field of such a system;
3. Liouville theorem also suggests all the stable periodic orbits of system Eq. 2.25 are of the critical case.

As an aside, we may refer to one of these forms of the motion equation as necessary (Eqs. 2.20, 2.22, 2.24 and 2.25) in following chapters of this thesis.

## 2.5 Dynamical Factor $\kappa$

In order to simplify the expressions, we present the dimensionless form of Eq. 2.20, taking the rotational period  $T_A$  as the time scaler  $[T]$ , and the equivalent radius (the radius of a sphere with the same volume) as the length scaler  $[L]$  (Eq. 2.28).

$$[T] = T_A, [L] = \sqrt[3]{\frac{3V_A}{4\pi}}. \quad (2.28)$$

Introducing scaled time  $\tau = t/[T]$ , and combining Eqs. 2.15 and 2.20, we have

$$\tilde{r}'' + 4\pi\hat{\omega}\times\tilde{r} + 4\pi^2\hat{\omega}\times(\hat{\omega}\times\tilde{r}) = \kappa \left( \sum_{e \in ES} L_e \mathbf{E}_e \cdot \tilde{r}_e - \sum_{f \in FS} \theta_f \mathbf{F}_f \cdot \tilde{r}_f \right), \quad (2.29)$$

where “ $'$ ” indicates the relative derivative about the scaled time  $\tau$ , and “ $\sim$ ” indicates scaled length vectors. The dimensionless parameter on the right hand side of Eq. 2.29 is defined as

$$\kappa = GT_A^2\sigma. \quad (2.30)$$

We regard  $\kappa$  as an important indicator for the orbital behaviours around the small body. The bracketed terms on the right hand side of Eq. 2.29 correspond to the polyhedral shape of the target small body, and  $\kappa$  is a comprehensive reflection of the influence of the small body's rotational period and bulk density, i.e. it describes the combination of the asteroidal gravity and centrifugal force due to the rotation.

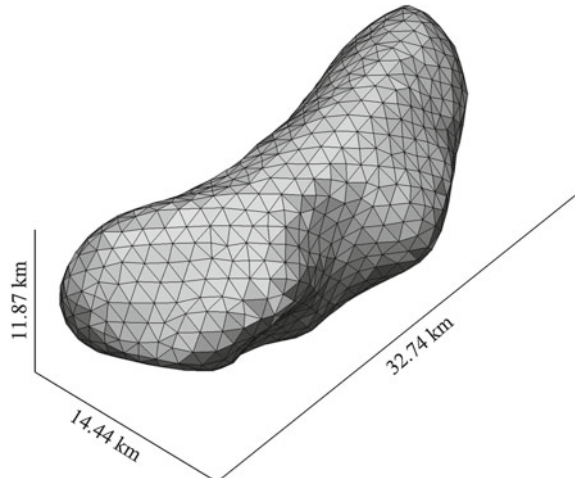
Qualitatively, large  $\kappa$  value can respond to a large bulk density, or a slow rotational speed of the target body.

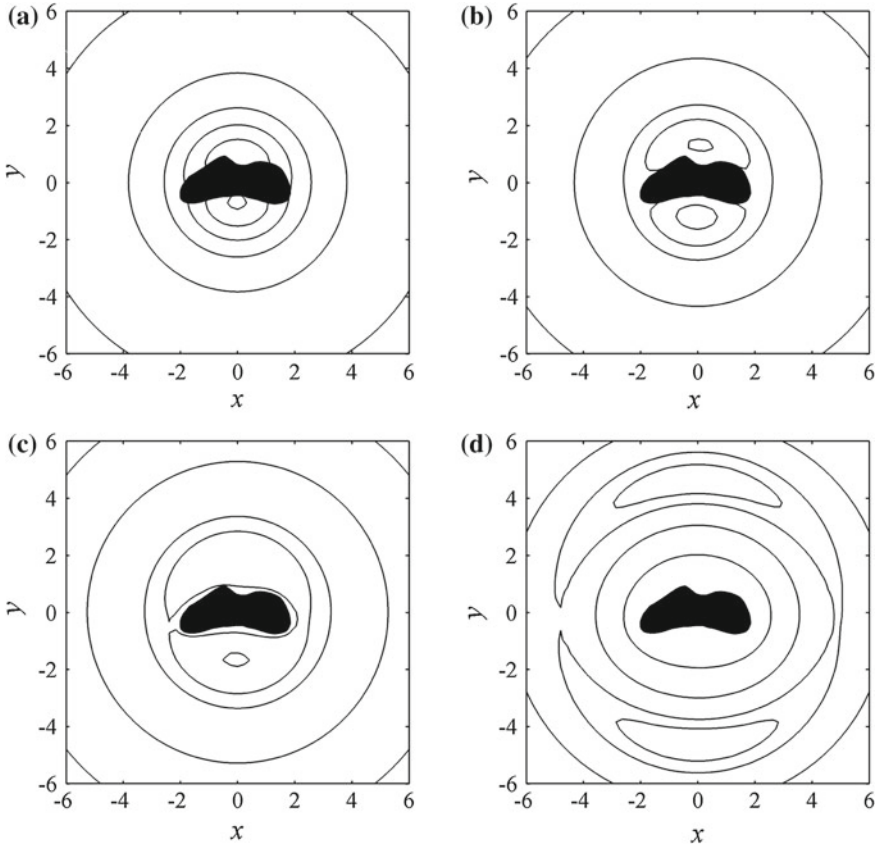
The dependence of the system dynamics on parameter  $\kappa$  is checked for a specific asteroid 433 Eros. Figure 2.8 show the polyhedral shape model of Eros, including 856 vertices and 1708 triangle facets. Eros has an elongated shape, with a narrow “neck” in the middle (supposed to be formed by a meteorite impact), box size of  $11.87 \times 14.44 \times 32.74$  km. According to the data returned by NEAR Shoemaker, Eros has a bulk density of 2.67 g/cc, and is rotating uniformly around the principal axes of maximum inertia with the period 5.27 h.

Figure 2.9 illustrates the variation of efficient potential  $V$  on the equatorial plane as  $\kappa$  increasing, in which the contour lines of  $V$  are shown at  $\kappa = 10$  (a),  $\kappa = 30$  (b),  $\kappa = 64$  (c) and  $\kappa = 990$  (d), respectively. The singular points of the contour lines indicate the stationary values of function  $V(x, y)$ , or namely, the equilibrium points of gravity and centrifugal force (stationary orbit in inertia frame). As shown in Fig. 2.9, (a) when  $\kappa = 10$ , there exists only 1 equilibrium point in the exterior of Eros, which is close to the surface, suggesting a strong centrifugal effect that the surface material can cannot accumulate if there is no coherence force; (b) when  $\kappa = 30$ , the gravitational effect of Eros is stronger, and there appear 2 equilibrium points close to the surface; (c) when  $\kappa = 64$  (close to the actual value of Eros 64.10), there are 4 equilibrium points (the 2 along the long axis are close to the surface), in which case the regolith material can stay on the surface of Eros relying on the gravity; (b) when  $\kappa = 990$ , the 4 equilibrium points are far away from Eros, showing the gravity is the dominant role in the near-field regime of Eros in this case.

The above discussion shows the altitude of stationary orbit (distance from the equilibrium to the surface of the small body) is a crucial indicator, which determines the dynamics of system to some extent. Here we give a general approximate analysis:

**Fig. 2.8** The polyhedral shape model of asteroid 433 Eros





**Fig. 2.9** The contour lines of efficient potential  $V$  on the equatorial plane of asteroid 433 Eros (plotted in scaled axes). **a**  $\kappa = 10$ . **b**  $\kappa = 30$ . **c**  $\kappa = 64$  (close to the actual value). **d**  $\kappa = 990$

assuming the target body is a solid sphere of radius  $[L]$ , the altitude of stationary orbit  $h$  satisfies

$$h = \left( \sqrt[3]{\frac{\kappa}{3\pi}} - 1 \right) [L]. \quad (2.31)$$

According to Eq. 2.31,  $h$  and  $\kappa$  are correlated:  $h \geq 0$  if  $\kappa \geq 3\pi$ , in which case the equilibrium points locate outside the target body, and divide the regions dominated by the gravity and that by the centrifugal force;  $h < 0$  if  $\kappa < 3\pi$ , in which case the equilibrium points locate inside the target body, and the self-gravity of the body is not sufficient to hold the surface materials, which are aggregated by coherence force within the matter. Note that most Solar System small bodies (especially those of diameter greater than 300 m) have “rubble pile” interiors, therefore bodies of  $\kappa < 3\pi$  should be quite rare in reality.

**Table 2.2** The bulk densities, rotational periods and  $\kappa$  values of 24 asteroids

Asteroid	$\sigma$ (g/cc)	$T_A$ (h)	$\kappa$
1 Ceres	2.12	9.07	150.7583
2 Pallas	2.71	7.81	142.9999
4 Vesta	3.44	5.34	84.8588
10 Hygiea	2.76	27.62	1820.4620
11 Parthenope	2.72	9.43	209.0851
15 Eunomia	0.96	6.08	30.7070
16 Psyche	2.00	4.20	30.4391
20 Massalia	3.26	8.10	184.8009
22 Kalliope	2.50	4.15	37.1833
45 Eugenia	1.20	5.70	33.6907
87 Sylvia	1.62	5.18	37.6336
90 Antiope	1.30	16.50	305.9441
121 Hermione	1.96	6.00	60.9943
216 Kleopatra	3.60	5.39	90.2412
243 Ida	2.60	4.63	48.2632
253 Mathilde	1.30	8.17	75.0099
433 Eros	2.67	5.27	64.1008
704 Interamnia	4.40	8.69	287.2255
762 Pulcova	1.80	5.84	53.0494
804 Hispania	4.90	7.40	231.9479
1620 Geographos	2.00	5.22	47.1088
2063 Bacchus	2.44	14.90	468.2667
66391 1999KW4	2.39	2.77	15.7950
2000UG11	1.47	4.44	25.0504

Table 2.2 lists the  $\kappa$  values of 24 asteroids with known bulk densities and rotational periods. It shows the  $\kappa$  of these real small bodies distributes over a wide range from 15.79 to 1820.46, and over 70 % are concentrated within the range from 20 to 200. The results of all these 24 asteroids conform with  $\kappa \geq 3\pi$ , which supports the theory of “rubble pile” structure with solid evidences in dynamics.

## 2.6 Summary

This chapter discussed the methodologies of dynamic modelling for a spacecraft (or small natural objects) orbiting around a small body, and special attentions are paid to the mathematical essence and parameter dependence of the motion equations.

The first part of this chapter presents an analysis on two major forms of perturbations (solar radiation pressure and the solar tide), including the perturbative magnitudes varying as the mass of target body and the distance away from it. The near-field region dominated by the gravity of the small body is defined by recalling and comparing three typical definitions of the influential sphere. In the second part, this chapter surveyed the major approaches to describe the gravitational field of a celestial body, clarified the advantages of polyhedral method and discussed the probabilities to apply other approaches as supplement means.

We proposed a crucial dynamical factor  $\kappa$  and checked the dependence of system behaviours on it, showing the following points:

1. For a given shape model, the value of  $\kappa$  determines the geometric properties of the efficient potential  $V$ , whose topology changes as  $\kappa$ ;
2. The value of  $\kappa$  determines the number and positions of the equilibrium points, and the spatial area dominated by the gravity of the small body;
3. All the asteroids we checked (with known bulk density and rotational period) satisfy  $\kappa > 3\pi$ , which supports the “rubble pile” structures of SSSBs in statistics.

## References

1. NEAT (Near-Earth Asteroid Tracking). Issue (2014). available at <http://neat.jpl.nasa.gov/>
2. Bowell E, Virtanen J, Muinonen K (2002) Asteroid orbit computation. In: William F et al Asteroids III. University Arizona Press, Tucson, AZ, pp 27–44
3. Hamilton DP, Burns JA (1991) Orbital stability zones about asteroids. II. The destabilizing effects of eccentric orbits and of solar radiation. *Icarus* 96:43–64
4. Gong S (2009) Study on dynamics and control of sail-craft. Tsinghua University, Beijing
5. Chen Q, Chen Z, Wang H (2013) Method of modeling solar radiation pressure based on attitude control law of navigation satellites. In: 4th national satellite guidance academic annual conference, Wuhan, China, 15–18 May 2013
6. NASA (National Aeronautics and Space Administration). Issue (2015). available at [http://www.nasa.gov/multimedia/imagegallery/image\\_feature\\_2010.html](http://www.nasa.gov/multimedia/imagegallery/image_feature_2010.html)
7. Werner RA, Scheeres DJ (1997) Exterior gravitation of a polyhedron derived and compared with harmonic and mascon gravitation representations of asteroid 4769 castalia. *Celest. Mech. Dyn. Astron.* 65:313–344
8. Romain G, Jean-Pierre B (2001) Ellipsoidal harmonic expansions of the gravitational potential: theory and application. *Celest. Mech. Dyn. Astron.* 19:235–275
9. Garmier R, Barriot J, Konopliv AS et al (2002) Modeling of the Eros gravity field as an ellipsoidal harmonic expansion from the NEAR Doppler tracking data. *Geophys Res Lett* 29:721–723
10. Werner RA (1994) The gravitational potential of a homogeneous polyhedron or don't cut corners. *Celest. Mech. Dyn. Astron.* 59:253–278
11. Pravec P, Harris AW, Michalowski T (2002) Asteroid rotations. In: William F et al Asteroids III. University, Arizona Press, Tucson, AZ, pp 113–122
12. Arnold VI (2006) Mathematical methods of classical mechanics. In: Translated by Qi M (ed), vol 4, Higher Education Press, Beijing, pp. iii–v

# Chapter 3

## Stability of Equilibrium Points and Behaviour of Nearby Trajectories

**Abstract** In physics, an equilibrium point means the positions in body-fixed frame  $Oxyz$  where the gravity from the small body and the centrifugal force balance. For a real small body which has irregular overlook, the equilibrium points are usually isolated and of finite number. This chapter takes the equilibria as a start of surveying the system dynamic behaviours, not only because of its simplicity, but also that the equilibria may be a key to understand the global orbital behaviours. As shown by Eq. 3.1, an equilibrium point is also a critical point of the contour surfaces of the efficient potential  $V$ , which is correlated to the topological evolution of these surfaces (see Sect. 2.5 for the discussion on  $\kappa$ ). In this chapter, we take a specific asteroid for example, and discuss the orbital motion within the neighbourhoods of equilibrium points using the polyhedral gravity model. Section 3.2 calculates the equilibrium points of the target body, and presents the geometry and topology of the contour surfaces of efficient potential  $V$ . Sections 3.3 and 3.4 use the linearized theory to determine the stability and type of an equilibrium point, and reveal the orbital motion on local invariant manifolds. Based on the analysis of local manifolds, Sect. 3.5 further discusses the general orbital patterns in the neighbourhoods of the equilibrium points.

**Keywords** Hamiltonian systems · Asteroid 216 Kleopatra · Methods: numerical · Methods: analytical · Stability · Periodic orbits

### 3.1 Introduction

For the system described in Eq. 2.22, an equilibrium point means the constant solution, which is independent on time  $t$  and satisfies

$$\nabla V(\mathbf{r}) = \mathbf{0}, \dot{\mathbf{r}} = \mathbf{0}, \ddot{\mathbf{r}} = \mathbf{0}. \quad (3.1)$$

In physics, an equilibrium point means the positions in body-fixed frame  $Oxyz$  where the gravity from the small body and the centrifugal force balance. For a real small body which has irregular overlook, the equilibrium points are usually isolated

and of finite number. This chapter takes the equilibria as a start of surveying the system dynamic behaviours, not only because of its simplicity, but also that the equilibria may be a key to understand the global orbital behaviours. As shown by Eq. 3.1, an equilibrium point is also a critical point of the contour surfaces of the efficient potential  $V$ , which is correlated to the topological evolution of these surfaces (see Sect. 2.5 for the discussion on  $\kappa$ ).

In this chapter, we take a specific asteroid for example, and discuss the orbital motion within the neighbourhoods of equilibrium points using the polyhedral gravity model. Section 3.2 calculates the equilibrium points of the target body, and presents the geometry and topology of the contour surfaces of efficient potential  $V$ . Sections 3.3 and 3.4 use the linearized theory to determine the stability and type of an equilibrium point, and reveal the orbital motion on local invariant manifolds. Based on the analysis of local manifolds, Sect. 3.5 further discusses the general orbital patterns in the neighbourhoods of the equilibrium points.

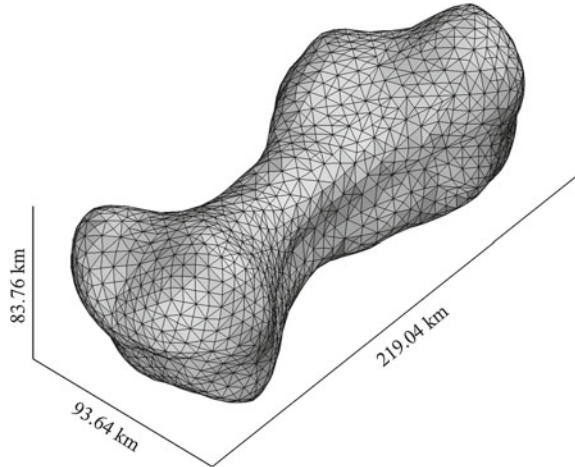
## 3.2 Equilibrium Points of Asteroid 216 Kleopatra

In this chapter, we take a specific asteroid 216 Kleopatra as an example for the discussion on equilibria. Compared with a general abstract model, we pay more attention to the influence of individual differences on the near-field orbital dynamics. The choice of Kleopatra is based on following reasons: first, Kleopatra has been long noticed because of its relatively high spin rate, and in 2000, Ostro et al. derived its light-curve shape model from radar observations [1], which enables the application of polyhedral method in estimating its gravitational field; second, Kleopatra has a prolate dumb-like shape, which is representative of a large group of small bodies, such as 4769 Castalia, 4179 Toutatis, 243 Ida, 433 Eros and 113 Amaltea etc.; third, French astronomer Franck found in 2008 that Kleopatra has two moons, Alexhelios (S/2008 (216) 1) and Cleoselene (S/2008 (216) 2) [2], and Descamps measured the rotational speed and total mass of Kleopatra, and the orbits of the moons. In general, as a real physical system, Kleopatra provides an opportunity to validate our theoretical analysis.

### 3.2.1 *Equilibrium Points*

Figure 3.1 shows the polyhedral shape model of Kleopatra, including 2048 vertices and 4096 triangle facets, box size of  $219.04 \times 93.64 \times 83.76$  km. Kleopatra has a bulk density of  $\sim 3.6 \pm 0.4$  g/cc, corresponding to a total mass  $4.64 \times 10^{18}$  kg, and the moment of inertia around three principal axes  $x$ ,  $y$ ,  $z$  are

**Fig. 3.1** The polyhedral shape model of asteroid 216 Kleopatra



$$\begin{aligned} I_x &= 1.68 \times 10^{27} \text{ kg} \cdot \text{m}^2 \\ I_y &= 1.14 \times 10^{28} \text{ kg} \cdot \text{m}^2 \\ I_z &= 1.15 \times 10^{28} \text{ kg} \cdot \text{m}^2 \end{aligned}$$

And according to the shape index of small body defined by Scheeres et al. (Eq. 3.2), Kleopatra is of shape index  $\sim 0.99$ , which suggests it has typical dynamics of prolate bodies.

$$\rho = \frac{I_y - I_x}{I_z - I_x}. \quad (3.2)$$

The spherical coefficients of second order and degree can be derived directly from the momentums of inertia about principal axes, and for Kleopatra, we have (the unit of  $r_e$ : km)

$$\begin{aligned} C_{20} &= -1.07 \times 10^3 / r_e^2, \\ C_{22} &= 5.24 \times 10^2 / r_e^2. \end{aligned}$$

$C_{20}$  and  $C_{22}$  indicate the magnitude of non-spherical perturbation, and is usually employed as a rough model of the small body's gravitational field. Besides, the measurement shows Kleopatra is rotating uniformly around the principal axis of maximum inertia with the period 5.39 h. Then, the specific form of Eq. 3.1 yields

$$\sum_{e \in ES} L_e \mathbf{E}_e \cdot \mathbf{r}_e - \sum_{f \in FS} \theta_f \mathbf{F}_f \cdot \mathbf{r}_f - \frac{1}{G\sigma} \boldsymbol{\omega} \times (\boldsymbol{\omega} \times \mathbf{r}), \quad (3.3)$$

in which  $L_e$ ,  $\theta_f$ ,  $\mathbf{r}_e$ ,  $\mathbf{r}_f$  are vector functions of  $\mathbf{r}$ ,  $\mathbf{E}_e$ ,  $\mathbf{F}_f$  are constant dyads,  $\boldsymbol{\omega}$  is constant vector, and  $G$ ,  $\sigma$  are constants. The key step to solve the nonlinear equation Eq. 3.3 is guessing the initial values. Here, we present a brief analysis on the feasible region of the initial guess:

1. The shape of Kleopatra is largely symmetric about the equatorial plane ( $xy$  plane) as shown in Fig. 3.1, and consider that the centrifugal force is always parallel with the equator, thus the  $z$  component of the resultant can only disappear when the filed point lies close to the equatorial plane;
2. The centrifugal force is a radial force, i.e., it is of the same direction with  $\mathbf{r}$ , and the asteroidal gravity that balances the centrifugal force must point to the body centre  $O$ , which ought to be around  $x$  and  $y$  axes;
3. The equilibrium points are the critical points of efficient potential  $V$ , namely, the nodal points of the contour lines in the equatorial plane (see Sect. 2.5), as illustrated in Fig. 3.2.

As stated above, Fig. 3.2 shows the positions of the initial guess for 4 equilibrium points in the exterior of Kleopatra, which are  $(-142, 0, 0)$ ,  $(142, 0, 0)$  on  $x$  axis and  $(0, -100, 0)$ ,  $(0, 100, 0)$  on  $x$  axis. Then, approaching the solutions of Eq. 3.3 by iterations, we obtain the precise solution to the equilibrium points. Table 3.1 lists the coordinates of the equilibrium points in the body-fixed frame  $Oxyz$ .

As shown in Table 3.1, due to the irregular shape of the small body, the gravitational field is not strictly symmetric and all 4 equilibrium points are offset from the axes at small distances. The dynamical factor  $\kappa$  for Kleopatra is 90.24, which is close to that of Eros (see Table 2.2), and thus, the distribution of the 4 equilibrium points is also like Eros, that  $E_1$ ,  $E_2$  are close to the surface along  $x$  axis and  $E_3$ ,  $E_4$  are

**Fig. 3.2** The contour lines of the efficient potential  $V$  in the equatorial plane of asteroid 216 Kleopatra (“ $\times$ ” indicates the initial guess of the equilibrium points)

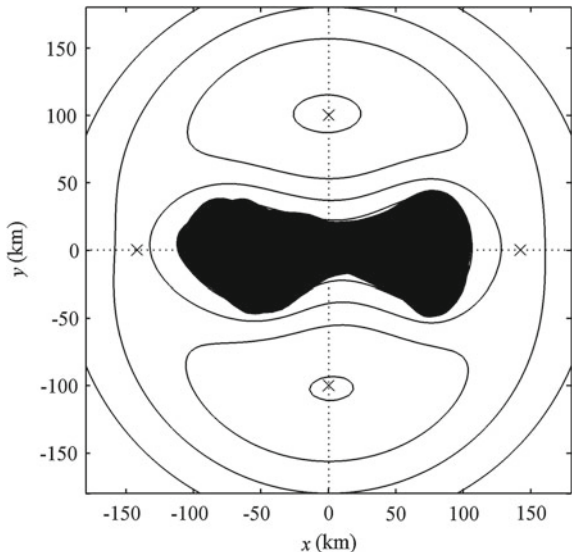


**Table 3.1** The positions of 4 equilibrium points of Kleopatra

Equilibrium point	$x$ (km)	$y$ (km)	$z$ (km)
$E_1$	142.8443	2.4414	1.1818
$E_2$	-144.6762	5.1889	-0.2726
$E_3$	2.2304	-102.0919	0.2719
$E_4$	-1.1637	100.7297	-0.5460

further from the surface along  $y$  axis. Accordingly, these elongated bodies of similar  $\kappa$  are supposed to have similar dynamic properties. The discussion of this chapter on Kleopatra will serve as a case study of a large group of SSSBs.

### 3.2.2 Zero-Velocity Surface

Equilibrium points  $E_1-E_4$  are the nodal points where the contour surface of the efficient potential  $V$  changes in topology, called zero-velocity surface that limits the accessible region of orbital motion with isotropic energetic level. Given, the Jacobi integral  $C$ , combining Eqs. 2.21 and 2.26, we have

$$V(\mathbf{r}) + \frac{1}{2}\dot{\mathbf{r}} \cdot \dot{\mathbf{r}} = C, \quad (3.4)$$

and apparently

$$V(\mathbf{r}) \leq C. \quad (3.5)$$

Equation 3.5 maps out a region in the configuration space in frame  $Oxyz$ , that limits the accessible region of all the orbits with Jacobi integral  $C$ ; in contrary, the leftover of the configuration space, named forbidden region, means the area where orbits of integral  $C$  can never enter. Zero-velocity surface is defined by the boundary of this division,  $V(\mathbf{r}) = C$ , so called for orbits of integral  $C$  approaching it will have speeds dropped to zero.

Zero-velocity surface provides a division of the solutions to dynamical system Eq. 2.22 based on energetic level. The geometry and topology of such surfaces are correlated with the behaviours of motion set with specified Jacobi integral. Figure 3.3 illustrates the zero-velocity surfaces of Kleopatra at different values of the Jacobi integral  $C$ , over a range from  $-2.57 \times 10^{-3} \text{ km}^2/\text{s}^2$  to  $-1.65 \times 10^{-3} \text{ km}^2/\text{s}^2$ , covering the values at 4 equilibrium points.

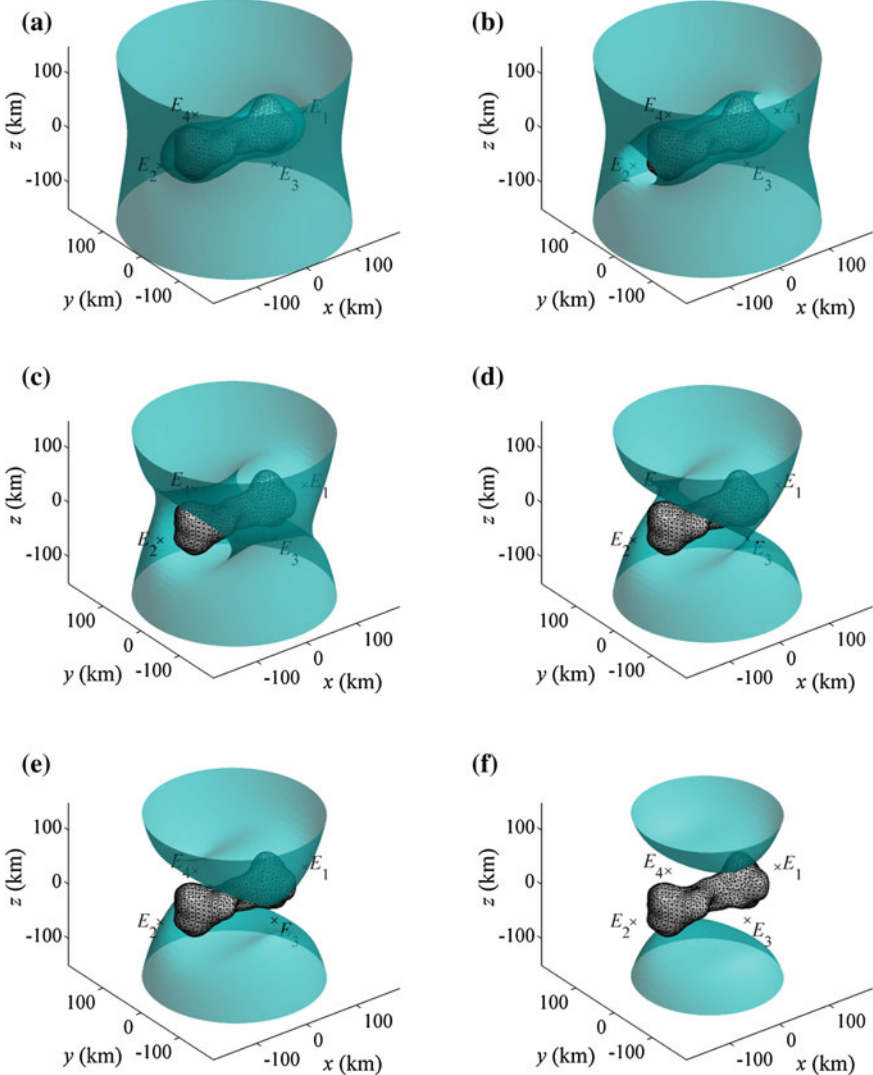


**Fig. 3.3** The zero-velocity surfaces of Kleopatra at different values of the Jacobi integral (“ $\times$ ” indicate the positions of equilibrium points  $E_1-E_4$ ). **a**  $C = -2.57 \times 10^{-3} \text{ km}^2/\text{s}^2$ . **b**  $C = -2.47 \times 10^{-3} \text{ km}^2/\text{s}^2$ . **c**  $C = -2.17 \times 10^{-3} \text{ km}^2/\text{s}^2$ . **d**  $C = -1.99 \times 10^{-3} \text{ km}^2/\text{s}^2$ . **e**  $C = -1.95 \times 10^{-3} \text{ km}^2/\text{s}^2$ . **f**  $C = -1.65 \times 10^{-3} \text{ km}^2/\text{s}^2$

Figure 3.3 includes 4 special cases:

1.  $C < -2.57 \times 10^{-3} \text{ km}^2/\text{s}^2$  (Fig. 3.3a), the surface splits into two leaves, the inner leaf is close to the surface of Kleopatra, and the shape of outer leaf looks like a rotational hyperboloid. The accessible region is also separated into two parts,

an orbit starting from the wide region outside the outer leaf will never access the surface of Kleopatra, and that starting from the narrow space between the inner leaf and Kleopatra will collide with the asteroid eventually.

2.  $-2.47 \times 10^{-3} \text{ km}^2/\text{s}^2 < C < -1.99 \times 10^{-3} \text{ km}^2/\text{s}^2$  (Fig. 3.3b, c), the inner leaf and outer leaf merge at  $E_1$  and  $E_2$ , and there appears a narrow channel through which the orbit starting from the inside region may escape to the wide outside region, or conversely, orbits starting from the outside may enter the narrow space and collide with the surface.
3.  $-1.99 \times 10^{-3} \text{ km}^2/\text{s}^2 < C < -1.95 \times 10^{-3} \text{ km}^2/\text{s}^2$  (Fig. 3.3d, e), the surface splits into two leaves once again, the upper leaf and lower leaf are basically symmetric about the equatorial plane, tending to touch each other at  $E_3$  and  $E_4$ . In this case, the region near the equatorial plane is all accessible, and that right above the two poles is the forbidden region.
4.  $C > -1.65 \times 10^{-3} \text{ km}^2/\text{s}^2$  (Fig. 3.3f), the two leaves shrink further and tend to disappear, and in this case the accessible region is connected and expanding.

Beside, Eq. 2.21 suggests that the whole configuration space will be accessible if  $C \geq 0 \text{ km}^2/\text{s}^2$ . Two points should be highlighted out of the above analysis: first, it is the distribution of equilibrium points that determines the branches of the zero-velocity surface; second, the special geometry of the surface around the equilibrium points (Fig. 3.3b, d) could be seen as an intuitive explanation for the surrounding orbits' sensibility to the initial conditions.

### 3.3 Stability of the Equilibrium Points

This section checks for the stability of the equilibrium points in the body-fixed frame  $Oxyz$ , or that of the stationary orbit in the inertia frame  $OXYZ$ . Defining the position vector of arbitrary equilibrium point  $\mathbf{r}_E$ , the state of disturbed equilibrium point is  $\mathbf{r} = \mathbf{r}_E + \delta\mathbf{r}$ ,  $\dot{\mathbf{r}} = \delta\dot{\mathbf{r}}$ , and the disturbed form of motion equation near the equilibrium point is

$$\begin{aligned}\delta\dot{\mathbf{r}} &= \delta\dot{\mathbf{r}}, \\ \delta\ddot{\mathbf{r}} &= -(\nabla\nabla U + \boldsymbol{\Omega}\boldsymbol{\Omega})\delta\mathbf{r} - 2\boldsymbol{\Omega}\delta\dot{\mathbf{r}},\end{aligned}\tag{3.6}$$

where  $\nabla\nabla U$  is the gradient matrix of gravity,  $\boldsymbol{\Omega}$  is the skew-symmetric matrix of the angular velocity vector  $\boldsymbol{\omega}$ , defined as

$$\nabla\nabla U = \begin{bmatrix} U_{xx} & U_{xy} & U_{xz} \\ U_{xy} & U_{yy} & U_{yz} \\ U_{xz} & U_{yz} & U_{zz} \end{bmatrix}, \quad \boldsymbol{\Omega} = \begin{bmatrix} 0 & -\omega_z & \omega_y \\ \omega_z & 0 & -\omega_x \\ -\omega_y & \omega_x & 0 \end{bmatrix}.\tag{3.7}$$

The coefficient matrix of Eq. 3.6 is

$$\mathbf{B} = \begin{bmatrix} \mathbf{O} & \mathbf{I} \\ -\nabla\nabla U - \boldsymbol{\Omega}\boldsymbol{\Omega} & -2\boldsymbol{\Omega} \end{bmatrix}.\tag{3.8}$$

**Table 3.2** The eigenvalues of linearized matrix  $\mathbf{B}$  at the equilibrium points of Kleopatra  $E_1-E_4$ 

Eigenvalue	$E_1 (10^{-3}/\text{s})$	$E_2 (10^{-3}/\text{s})$	$E_3 (10^{-3}/\text{s})$	$E_4 (10^{-3}/\text{s})$
$\lambda_1$	0.3761	0.4225	$0.2022 + 0.3040i$	$0.2018 + 0.3060i$
$\lambda_2$	-0.3761	-0.4225	$0.2022 - 0.3040i$	$0.2018 - 0.3060i$
$\lambda_3$	0.4251i	0.4665i	$-0.2022 + 0.3040i$	$-0.2018 + 0.3060i$
$\lambda_4$	-0.4251i	-0.4665i	$-0.2022 - 0.3040i$	$-0.2018 - 0.3060i$
$\lambda_5$	0.4134i	0.4135i	0.3270i	0.3227i
$\lambda_6$	-0.4134i	-0.4135i	-0.3270i	-0.3227i

The matrix  $\mathbf{B}$  is the linearized matrix of system Eq. 2.22 at equilibrium point  $\mathbf{r}_E$ , and its eigenvalues  $\lambda_i$  ( $i = 1, 2, \dots, 6$ ) determine the stability of the equilibrium point, s.t.

$$\det(\lambda \mathbf{I} - \mathbf{B}) = \prod_{i=1}^6 (\lambda - \lambda_i). \quad (3.9)$$

Substituting Eq. 3.8 into Eq. 3.9, it yields

$$\lambda^6 + b_4\lambda^4 + b_2\lambda^2 + b_0 = 0, \quad (3.10)$$

where  $b_0, b_3, b_4$  are real coefficients. Equation 3.10 is even polynomial, and the solution  $\lambda$  satisfies: if  $\lambda$  is an eigenvalue of  $\mathbf{B}$ , then  $-\lambda, \bar{\lambda}$  are also eigenvalues of  $\mathbf{B}$ . Thus the 6 eigenvalues of  $\mathbf{B}$  must be composed of the following cases:

1. Two opposite real numbers;
2. Two opposite purely imaginary numbers;
3. Four opposite conjugate complex numbers.

And the combination determines the topology of the equilibrium point. Table 3.2 lists the eigenvalues of linearized matrix  $\mathbf{B}$  at the equilibrium points of Kleopatra  $E_1-E_4$ . As shown,  $E_1$  and  $E_2$  are topologically equivalent, i.e., both have two opposite real eigenvalues and two pairs of opposite purely imaginary eigenvalues;  $E_3$  and  $E_4$  are topologically equivalent, i.e., both have four opposite conjugate complex eigenvalues and two opposite purely imaginary eigenvalues.

In order to check the stability of the equilibrium points, define the characteristic factor

$$\Xi = \max_{1 \leq i \leq 6} \operatorname{Re}(\lambda_i), \quad (3.11)$$

According to Lyapunov stability theory, the equilibrium point is asymptotically stable if  $\Xi < 0$ ; the equilibrium point is critically stable if  $\Xi = 0$ ; the equilibrium point is unstable if  $\Xi > 0$ .

Obviously, all the 4 equilibrium points of Kleopatra  $E_1-E_4$  are unstable due to the eigenvalues of positive real parts. Then, applying Lyapunov's second method [3], the linearly unstable equilibrium points  $E_1-E_4$  are also unstable with respect to the original system Eq. 2.22. Thus due to the asteroidal category of dynamical properties, Kleopatra is a type II asteroid.

### 3.4 Structure of Local Manifolds

Consider, the linearized system at arbitrary equilibrium point  $\mathbf{x}_0$

$$\dot{\mathbf{x}} = \mathbf{B}\mathbf{x}, \quad \mathbf{x} \in \mathbb{R}^6. \quad (3.12)$$

The linear system Eq. 3.12 is tangent with the original system Eq. 2.22 at  $\mathbf{x}_0$ , the centre manifold theorem ensures the local manifolds of Eq. 2.22 are also tangent with the corresponding subspaces of Eq. 3.12 at the equilibrium points [4]. In particular, supposing  $\mathbf{B}$  has  $n_s$  eigenvalues of negative real parts,  $n_c$  eigenvalues of zero real parts,  $n_u$  eigenvalues of positive real parts, then we define  $\mathbf{u}_i^s$  ( $i = 1, 2, \dots, n_s$ ),  $\mathbf{u}_j^c$  ( $j = 1, 2, \dots, n_c$ ) and  $\mathbf{u}_k^u$  ( $k = 1, 2, \dots, n_u$ ) the independent eigenvectors affiliated with the three types of eigenvalues, respectively (The conjugate complex eigenvectors are replaced with their real part and imaginary part, and general eigenvectors are adopted for the multiple cases). These three group of eigenvectors span the stable subspace  $T_s$ , centre subspace  $T_c$  and unstable subspace  $T_u$  of system Eq. 3.12:

$$\begin{aligned} T_s &= \text{span} \{ \mathbf{u}_1^s, \mathbf{u}_2^s, \dots, \mathbf{u}_{n_s}^s \}, \\ T_c &= \text{span} \{ \mathbf{u}_1^c, \mathbf{u}_2^c, \dots, \mathbf{u}_{n_c}^c \}, \\ T_u &= \text{span} \{ \mathbf{u}_1^u, \mathbf{u}_2^u, \dots, \mathbf{u}_{n_u}^u \}. \end{aligned} \quad (3.13)$$

The subspaces  $T_s$ ,  $T_c$  and  $T_u$  satisfy

$$\mathbb{R}^6 = T_s \oplus T_c \oplus T_u. \quad (3.14)$$

Then according to the centre manifold theorem:

1. There exist a unique  $n_s$  dimensional stable manifold  $W_s$  tangent with  $T_s$  at  $\mathbf{x}_0$ , defined as

$$W_s = \{ \mathbf{X} \in \Delta \mid \mathbf{x}(t, \mathbf{X}) \in \Delta \text{ for } \forall t \leq 0, \text{ and } \mathbf{x}(t, \mathbf{X}) \rightarrow \mathbf{x}_0 \text{ when } t \rightarrow \infty \}, \quad (3.15)$$

where  $\Delta$  is a neighbourhood of  $\mathbf{x}_0$  in phase space.

2. There exist a unique  $n_u$  dimensional unstable manifold  $W_u$  tangent with  $T_u$  at  $\mathbf{x}_0$ , defined as

$$W_u = \{X \in \Delta \mid \mathbf{x}(t, X) \in \Delta \text{ for } \forall t \leq 0, \text{ and } \mathbf{x}(t, X) \rightarrow \mathbf{x}_0 \text{ when } t \rightarrow -\infty\}. \quad (3.16)$$

3. There exist  $n_c$  dimensional centre manifold  $W_c$  tangent with  $T_c$  at  $\mathbf{x}_0$ , while the centre manifold might not be unique.

### 3.4.1 Three Types of Invariant Manifolds at $E_1$ and $E_2$

Section 3.3 shows the equilibrium points  $E_1$  and  $E_2$  have the same topology, and corresponding linearized systems can be decomposed into stable subspace  $T_s$ , unstable subspace  $T_u$ , centre subspace  $T_c$  of dimensions  $n_s = 1, n_u = 1, n_c = 4$ , respectively. Tables 3.3 and 3.4 list the normalized eigenvectors spanning these three types of subspaces at  $E_1$  and  $E_2$ , respectively.

Since the local manifolds  $W_s, W_u, W_c$  are tangent with the subspaces  $T_s, T_u, T_c$ , respectively, the basis vectors of these linear subspaces could be used to determine corresponding local manifolds at  $E_1$  and  $E_2$ . Figure 3.4 presents the projections of  $W_s, W_u$ , and two periodic motion families on  $W_c$  (4 dimensional) at  $E_1$  and  $E_2$ .

As illustrated in Fig. 3.4a, b,  $W_s$  and  $W_u$  at  $E_1/E_2$  form a local saddle manifold, corresponding to a pair of opposite real eigenvalues (see Table 3.2). Motion on the saddle manifold will approach or depart from  $E_1/E_2$  asymptotically. In order to

**Table 3.3** The normalized eigenvectors of linearized matrix  $\mathbf{B}$  at  $E_1$

$\hat{\mathbf{u}}_1^s$	$\hat{\mathbf{u}}_1^u$	$\hat{\mathbf{u}}_1^c$	$\hat{\mathbf{u}}_2^c$	$\hat{\mathbf{u}}_3^c$	$\hat{\mathbf{u}}_4^c$
0.6206	0.6416	-0.0127	-0.8510	-0.1805	-0.5418
0.7842	-0.7669	0.9264	0.0000	0.6116	-0.8405
-0.0015	-0.0149	-0.3763	-0.5251	0.7703	0.0000
-0.0002	0.0002	0.0002	0.0000	0.0001	-0.0002
-0.0003	-0.0003	0.0000	0.0008	0.0002	0.0005
0.0000	0.0000	0.0001	-0.0003	0.0000	0.0007

**Table 3.4** The normalized eigenvectors of linearized matrix  $\mathbf{B}$  at  $E_2$

$\hat{\mathbf{u}}_1^s$	$\hat{\mathbf{u}}_1^u$	$\hat{\mathbf{u}}_1^c$	$\hat{\mathbf{u}}_2^c$	$\hat{\mathbf{u}}_3^c$	$\hat{\mathbf{u}}_4^c$
-0.7118	0.6697	0.0229	-0.9979	0.0128	0.7615
-0.7024	-0.7425	0.9969	0.0000	-0.1352	0.6481
-0.0010	-0.0133	-0.0750	-0.0652	-0.9907	0.0000
-0.0003	0.0003	0.0002	0.0000	0.0000	0.0001
-0.0003	-0.0003	0.0000	0.0010	0.0000	-0.0007
0.0000	0.0000	0.0000	-0.0001	0.0000	-0.0054

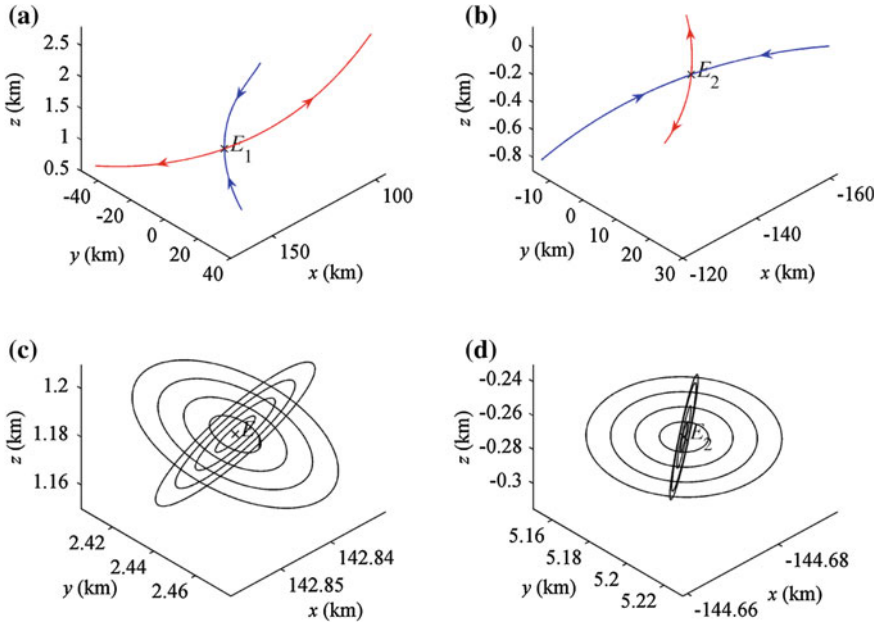


**Fig. 3.4** The stable, unstable, centre local manifolds at  $E_1$  and  $E_2$ , projected into the configuration space (blue/red lines indicate the stable/unstable manifolds respectively). **a**  $E_1$ :  $W_s$  and  $W_u$ . **b**  $E_2$ :  $W_s$  and  $W_u$ . **c**  $E_1$ : two periodic motion families on  $W_c$ . **d**  $E_2$ : two periodic motion families on  $W_c$

measure the approaching/departing speed, we introduce the characteristic time, that for a local manifold affiliated with the eigenvalues of form  $\lambda = \pm\alpha \pm \beta i$ , define

$$\Gamma_\alpha = 2\pi|\alpha|^{-1}, \quad \Gamma_\beta = 2\pi|\beta|^{-1}. \quad (3.17)$$

Then for  $W_s$  and  $W_u$  at equilibrium point  $E_1$ ,  $\Gamma_\alpha = 4.64$  h,  $\Gamma_\beta = \infty$ , and for  $W_s$  and  $W_u$  at equilibrium point  $E_2$ ,  $\Gamma_\alpha = 4.13$  h,  $\Gamma_\beta = \infty$ , meaning the general motion on the saddle manifold has no spiral component.

Figure 3.4c, d illustrate the periodic motion families  $c_1$  and  $c_2$  on the centre manifold  $W_c$  at equilibrium point  $E_1/E_2$ , and each family corresponds to a pair of purely imaginary eigenvalues (see Table 3.2). The characteristic times of family  $c_1$  at  $E_1$ :  $\Gamma_\alpha = \infty$ ,  $\Gamma_\beta = 4.22$  h; the characteristic times of family  $c_2$  at  $E_1$ :  $\Gamma_\alpha = \infty$ ,  $\Gamma_\beta = 4.11$  h; the characteristic times of family  $c_1$  at  $E_2$ :  $\Gamma_\alpha = \infty$ ,  $\Gamma_\beta = 4.22$  h; the characteristic times of family  $c_2$  at  $E_2$ :  $\Gamma_\alpha = \infty$ ,  $\Gamma_\beta = 3.74$  h. Orbits in the same family have similar periods;  $c_1$  at  $E_1$  and  $c_1$  at  $E_2$  are periodic motion out of the equatorial plane with similar periods. Besides, the centre manifold  $W_c$  also contains quasi-periodic motion composed of components of both periods of  $c_1$  and  $c_2$ , which is a general form of the motion on the centre manifold.

### 3.4.2 Three Types of Invariant Manifolds at $E_3$ and $E_4$

The equilibrium points  $E_3$  and  $E_4$  have the same topology, and corresponding linearized systems can be decomposed into stable subspace  $T_s$ , unstable subspace  $T_u$ , centre subspace  $T_c$  of dimensions  $n_s = 2$ ,  $n_u = 2$ ,  $n_c = 2$ , respectively. Tables 3.5 and 3.6 list the normalized eigenvectors spanning these three types of subspaces at  $E_3$  and  $E_4$ , respectively.

Since the local manifolds  $W_s$ ,  $W_u$ ,  $W_c$  are tangent with the subspaces  $T_s$ ,  $T_u$ ,  $T_c$ , respectively, the basis vectors of these linear subspaces could be used to determine corresponding local manifolds at  $E_1$  and  $E_2$ . Figure 3.5 presents the projections of  $W_s$ ,  $W_u$ , and periodic motion family on  $W_c$  at  $E_1$  and  $E_2$ .

As illustrated in Fig. 3.5a, b,  $W_s$  and  $W_u$  are both 2 dimensional at  $E_3/E_4$ , corresponding to four opposite conjugate complex eigenvalues (see Table 3.2), suggesting that orbits on  $W_s$  and  $W_u$  will approach or depart from  $E_3/E_4$  in a spiral way. Recalling the definition of characteristic times defined in Sect. 3.4.1, for  $W_s$  and  $W_u$  at equilibrium point  $E_3$ ,  $\Gamma_\alpha = 8.63$  h,  $\Gamma_\beta = 5.74$  h, and for  $W_s$  and  $W_u$  at equilibrium point  $E_4$ ,  $\Gamma_\alpha = 8.65$  h,  $\Gamma_\beta = 5.70$  h, meaning the orbits on  $W_s$  and  $W_u$  spiral into and away from  $E_3/E_4$ , respectively. Figure 3.5c, d illustrate the periodic motion family on the centre manifold  $W_c$  at equilibrium point  $E_3/E_4$ , corresponding to a pair of opposite purely imaginary eigenvalues: for the family at  $E_3$ ,  $\Gamma_\alpha = \infty$ ,  $\Gamma_\beta = 5.34$  h, and for the family at  $E_3$ ,  $\Gamma_\alpha = \infty$ ,  $\Gamma_\beta = 5.41$  h.

**Table 3.5** The normalized eigenvectors of linearized matrix  $\mathbf{B}$  at  $E_3$

$\hat{u}_1^s$	$\hat{u}_2^s$	$\hat{u}_1^u$	$\hat{u}_2^u$	$\hat{u}_1^c$	$\hat{u}_2^c$
0.9931	0.0000	0.9867	0.0000	0.0380	0.2628
-0.1171	0.9998	0.1628	0.9998	-0.0045	0.9647
-0.0088	-0.0177	-0.0030	0.0191	0.9993	0.0000
-0.0002	0.0004	0.0002	0.0004	0.0000	0.0005
-0.0002	-0.0003	-0.0002	0.0003	0.0000	-0.0001
0.0000	0.0000	0.0000	0.0000	0.0000	0.0136

**Table 3.6** The normalized eigenvectors of linearized matrix  $\mathbf{B}$  at  $E_4$

$\hat{u}_1^s$	$\hat{u}_2^s$	$\hat{u}_1^u$	$\hat{u}_2^u$	$\hat{u}_1^c$	$\hat{u}_2^c$
0.9914	0.0000	0.9904	0.0000	0.0042	-0.9787
-0.1308	0.9999	0.1384	0.9999	0.0104	0.2306
-0.0050	0.0037	0.0062	-0.0004	-0.9999	0.0000
-0.0002	0.0004	0.0002	0.0004	0.0000	0.0001
-0.0002	-0.0003	-0.0002	0.0003	0.0000	0.0003
0.0000	0.0000	0.0000	0.0000	0.0000	-0.0263

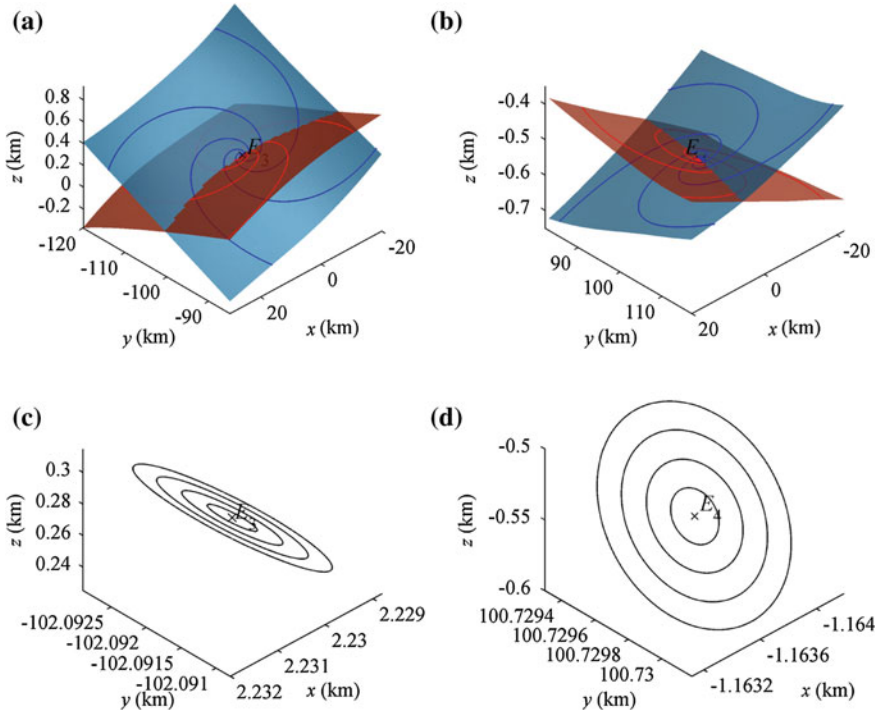


**Fig. 3.5** The stable, unstable, centre local manifolds at  $E_3$  and  $E_4$ , projected into the configuration space (blue/red surfaces indicate the stable/unstable manifolds respectively). **a**  $E_3$ :  $W_s$  and  $W_u$ . **b**  $E_4$ :  $W_s$  and  $W_u$ . **c**  $E_3$ : two periodic motion families on  $W_c$ . **d**  $E_4$ : two periodic motion families on  $W_c$

As for the general motion around the equilibrium points of Kleopatra, the unstable manifolds play a dominant role. Comparing the characteristic time  $\Gamma_\alpha$  of  $W_u$  at  $E_1-E_4$ , we find  $E_1, E_2$  are more unstable than  $E_3, E_4$ , i.e., the orbits around  $E_1/E_2$  will diverge faster than those around  $E_3/E_4$ .

### 3.4.3 Periodic Orbital Families Determined from Central Manifolds

The periodic orbits around the equilibrium points of small bodies are significant to designing hovering orbits of spacecrafts. Sections 3.4.1 and 3.4.2 present the periodic orbits of sizes smaller than 100 m around  $E_1-E_4$  of Kleopatra based on the linearized system. In practice, the feasible region of such periodic orbits could be much larger, e.g., the Halo orbits around Lagrange points in the Circular Restricted Three Body Problem (CRTBP).

This section surveys the periodic orbits around  $E_1-E_4$  in greater scale. The initial guess is still given by the basis vectors of corresponding centre subspace  $k\hat{u}_j^c$  ( $j = 1, 2, \dots, n_c$ ), in which  $k$  indicates the size of the periodic orbit. For a large  $k$ , the approximating of linearized system Eq. 3.12 to original system Eq. 2.22 is not perfect, thus an effective iteration is necessary to achieve periodic motion on the centre manifold of larger scale.

Figure 3.6 show the iteration results around equilibrium points  $E_1-E_4$  of Kleopatra, including 6 periodic families  $c_1-c_6$ . Apparently, these 6 families can be seen as extension of the local families obtained in Sects. 3.4.1 and 3.4.2 (see Figs. 3.4c, d and 3.5c, d), and because the size has grown up to magnitude of 10 km, these orbits are not ellipse-shaped any more.

Table 3.7 lists the parameter ranges of orbital families  $c_1-c_6$ , which are indicated with the initial guess vectors of corresponding local centre manifold. The value of  $k$

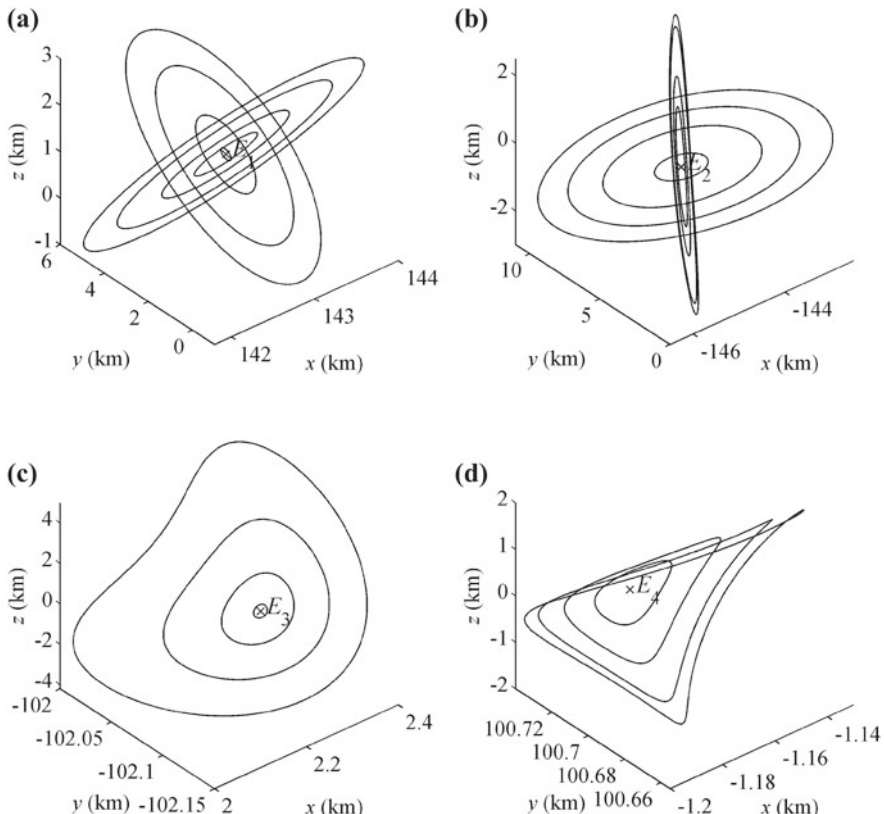


**Fig. 3.6** The periodic orbit families of a large scale around the equilibrium points of Kleopatra. **a** Equilibrium point  $E_1$ . **b** Equilibrium point  $E_2$ . **c** Equilibrium point  $E_3$ . **d** Equilibrium point  $E_4$

**Table 3.7** The parameter ranges of periodic orbit families  $c_1$ – $c_6$ 

Family	Initial guess	$k$ (km)	Period (h)	Jacobi integral ( $10^{-3}$ km $^2$ /s $^2$ )
$c_1$	$E_1, \hat{\mathbf{u}}_3^c$	0.1–3.0	4.2168–4.2219	–2.5408–2.5336
$c_2$	$E_1, \hat{\mathbf{u}}_1^c$	0.5–2.5	4.1058–4.1061	–2.5408–2.5376
$c_3$	$E_2, \hat{\mathbf{u}}_3^c$	0.5–2.5	4.1948–4.2207	–2.5603–2.5587
$c_4$	$E_2, \hat{\mathbf{u}}_1^c$	0.5–2.5	3.7411–3.7425	–2.5602–2.5554
$c_5$	$E_3, \hat{\mathbf{u}}_1^c$	0.1–2.5	5.3367–5.3370	–1.9902–1.9902
$c_6$	$E_4, \hat{\mathbf{u}}_1^c$	0.5–3.0	5.4080–5.4081	–1.9976–1.9976

reflects the size ranges of these orbital families, and the ranges of period and Jacobi integral are also listed.

As shown in Table 3.7, the ranges of period and Jacobi integral are small (particularly for  $c_5$  and  $c_6$ ), and the relative change ratio are below 6 and 2 %, respectively. Besides, different families around the same equilibrium point have neither close periods nor periods of simple ratios, namely there is no resonance between these families, and Lissajous orbits are hard to form in this case.

Hu et al. examined the relationship between stability of equilibrium points and that of periodic orbits around them based on gravitational field of the second order and degree, and pointed out the stability of nearby periodic orbits highly relies on the topology of the equilibrium point [5]. Here, we check the stability of these periodic orbits of greater scales.

Define a periodic solution  $\mathbf{x}^*$  to Eq. 2.24 with period  $T$ . Then following similar routines with Eqs. 3.6–3.8, we get the perturbed form of equation around  $\mathbf{x}^*$ , which is a linear system of periodic coefficients Eq. 3.18.

$$\delta\dot{\mathbf{x}} = \mathbf{B}(t) \delta\mathbf{x}, \quad 0 \leq t \leq T. \quad (3.18)$$

According to Floquet theorem, the linearized stability of  $\mathbf{x}^*$  depends on the eigen structure of state transfer matrix  $\mathbf{M}$ , which is also employed to judge the stability of periodic orbit in original system Eq. 2.24 [6]. The state transfer matrix  $\mathbf{M}$ , which is also known as monodromy matrix, is defined by Eq. 3.19.  $\mathbf{M}$  determines the transfer pattern of a perturbation on periodic orbit  $\mathbf{x}^*$  (see Sect. 4.3 for more details).

$$\mathbf{M} = \int_0^T \mathbf{B}(t) dt. \quad (3.19)$$

Define the characteristic factor  $\Theta$ , satisfying

$$\Theta = \max_{1 \leq i \leq 6} |\eta_i|, \quad (3.20)$$

**Table 3.8** The stability of periodic orbit families  $c_1$ – $c_6$  (“US” indicates unstable)

Family	$\Theta$	Stability
$c_1$	301.85–305.36	US
$c_2$	259.09–259.82	US
$c_3$	590.46–614.19	US
$c_4$	291.81–296.04	US
$c_5$	48.53–48.62	US
$c_6$	50.80–50.84	US

where  $\eta_i$  ( $i = 1, 2, \dots, 6$ ) are eigenvalues of  $\mathbf{M}$ . Then according to Floquet theorem, the periodic orbit  $\mathbf{x}^*$  is stable if  $\Theta > 1$ ;  $\mathbf{x}^*$  is unstable if  $\Theta < 1$ ; and  $\Theta = 1$  is the critical case.

Table 3.8 presents the range of characteristic factor  $\Theta$  for the 6 periodic orbit families around Kleopatra’s equilibrium points, showing family  $c_1$ – $c_6$  are all unstable. Moreover, the magnitude of  $\Theta$  in Table 3.8 suggests the periodic orbits around  $E_1/E_2$  are more unstable than those around  $E_3/E_4$ , which is consistent with the analysis of characteristic time in Sects. 3.4.1 and 3.4.2. Briefly, the stability properties of these large-scale periodic orbits prove to be consistent with that of corresponding equilibrium point.

### 3.5 Orbital Behaviours in the Neighbourhood of Equilibrium Points

This section focuses on the general motion in the neighbourhood of an equilibrium point, based on the analysis of the three types of local manifolds (stable, unstable, centre), and special attention will be paid to the morphologies of the general orbital motion. The orbital behaviours within a small neighbourhood is approximated by the linearized system Eq. 3.12 at the equilibrium point. The general form of solutions to Eq. 3.12 is

$$\mathbf{x}(t) = e^{\mathbf{B}t} \mathbf{x}_0, \quad (3.21)$$

where  $\mathbf{x}_0$  is the initial state. For the  $6 \times 6$  linearized matrix  $\mathbf{B}$ , Sect. 3.3 has stated its eigenvalues  $\lambda_i$  ( $i = 1, 2, \dots, 6$ ) are composed of following cases: I. opposite real numbers; II. conjugate complex numbers (including the purely imaginary case). Block diagonalization of  $\mathbf{B}$  is achieved by applying similarity transformation  $\mathbf{P}$ :

$$\mathbf{B} = \mathbf{P} \begin{bmatrix} \mathbf{B}_1 & & \mathbf{O} \\ & \mathbf{B}_2 & \\ & & \ddots \\ \mathbf{O} & & \mathbf{B}_m \end{bmatrix} \mathbf{P}^{-1}, \quad (3.22)$$

where  $\mathbf{B}_j$  ( $j = 1, 2, \dots, m$ ) could be either a  $1 \times 1$  block, corresponding to a real eigenvalue  $\lambda$ :

$$\mathbf{B}_j = \lambda, \quad (3.23)$$

or a  $2 \times 2$  block, corresponding to a pair of conjugate complex eigenvalues  $\alpha \pm \beta i$ :

$$\mathbf{B}_j = \begin{bmatrix} \alpha & -\beta \\ \beta & \alpha \end{bmatrix}. \quad (3.24)$$

By using Taylor expansion to Eqs. 3.21 and 3.22, we have

$$e^{\mathbf{B}t} = \mathbf{P} \begin{bmatrix} e^{\mathbf{B}_1 t} & & \mathbf{O} \\ & e^{\mathbf{B}_2 t} & \\ & & \ddots \\ \mathbf{O} & & e^{\mathbf{B}_m t} \end{bmatrix} \mathbf{P}^{-1}, \quad (3.25)$$

And the diagonalized blocks in Eq. 3.25 yield

$$e^{\mathbf{B}_j t} = \begin{cases} e^{\lambda t} & \text{if } \mathbf{B}_j = \lambda \\ e^{\alpha t} \begin{bmatrix} \cos \beta t & -\sin \beta t \\ \sin \beta t & \cos \beta t \end{bmatrix} & \text{if } \mathbf{B}_j = \begin{bmatrix} \alpha & -\beta \\ \beta & \alpha \end{bmatrix} \end{cases} \quad (3.26)$$

In which the case of multiple eigenvalues is not included. Define  $\mathbf{y}$  the transformed initial state, and divide  $\mathbf{y}$  in the same blocking as follows.

$$\mathbf{y} = \mathbf{P}^{-1} \mathbf{x}_0 = \begin{bmatrix} \mathbf{y}_1 \\ \mathbf{y}_2 \\ \vdots \\ \mathbf{y}_m \end{bmatrix}. \quad (3.27)$$

Then the general form of solution to Eq. 3.12 is represented as

$$\mathbf{x}(t) = \mathbf{P} \begin{bmatrix} e^{\mathbf{B}_1 t} \mathbf{y}_1 \\ e^{\mathbf{B}_2 t} \mathbf{y}_2 \\ \vdots \\ e^{\mathbf{B}_m t} \mathbf{y}_m \end{bmatrix}. \quad (3.28)$$

Equation 3.28 shows the general orbit  $\mathbf{x}(t)$  around the equilibrium point is the linear combination of the motion modes corresponding to above blocks. Based on this point, Sects. 3.5.1 and 3.5.2 will take a detailed look into the general motion patterns around 4 equilibrium points of Kleopatra, respectively.

As an aside, the topological equivalence between original system Eq. 2.24 and the linearized system Eq. 3.12 has not been completely addressed. Since the equilibrium points of Hamiltonian systems are structurally unstable, we can only ensure the numeric approximation of linearization methodology to original system in small neighbourhoods around the equilibrium points.

### 3.5.1 Behaviours of Trajectories Near $E_1$ and $E_2$

The linearized matrix  $\mathbf{B}$  at equilibrium point  $E_1/E_2$  has a pair of opposite real eigenvalues  $\pm\lambda$  and two pairs of opposite purely imaginary eigenvalues  $\pm\beta_1 i, \pm\beta_2 i$ . The motion modes corresponding to these blocks are

$$e^{\lambda t}, e^{-\lambda t}, \begin{bmatrix} \cos\beta_1 t & -\sin\beta_1 t \\ \sin\beta_1 t & \cos\beta_1 t \end{bmatrix}, \begin{bmatrix} \cos\beta_2 t & -\sin\beta_2 t \\ \sin\beta_2 t & \cos\beta_2 t \end{bmatrix}, \quad (3.29)$$

which correspond to the motion on the unstable subspace  $T_u$ , stable subspace  $T_s$  and centre subspace  $T_c^1, T_c^2$ . The general motion in the neighbourhoods of  $E_1$  and  $E_2$  is composed of these patterns, as illustrated in Fig. 3.7:

1. Define the non-centre subspace  $T_{nc} = T_u \oplus T_s$ , then  $\dim(T_{nc}) = 2$ . Figure 3.7a shows the motion patterns on  $T_{nc}$ , i.e., the orbits initialized with a state  $\mathbf{y}$  on  $T_{nc}$ .  $T_u$  and  $T_s$  form a saddle point at the equilibria  $E$  (representative for  $E_1$  or  $E_2$ ), and the double arrows indicate the local manifolds tangent with  $T_u$  and  $T_s$ , forming the asymptotics of arbitrary orbit on  $T_{nc}$ . Thus the general motion form on  $T_{nc}$  is to depart from the unstable manifold and approach the stable manifold asymptotically.
2. Figure 3.7b shows the general pattern of an orbit initialized with both components on  $T_s$  and  $T_c$ , where the periodic circle indicates the centre manifold. The general motion form in this case is to approach the centre manifold along the stable one.
3. Figure 3.7c shows the general pattern of an orbit initialized with both components on  $T_u$  and  $T_c$ , in which case the unstable manifold takes the dominant role and the general motion form is to escape from the centre manifold along the unstable one.
4. Figure 3.7d shows the general pattern of an orbit initialized with both components on  $T_c^1$  and  $T_c^2$ , when the orbit lies on the local centre manifold, and the general motion form is quasi-periodic including circles of frequencies  $\beta_1$  and  $\beta_2$  at the same time.

As a summary, in the neighbourhoods of  $E_1/E_2$  of Kleopatra, the motion on  $T_c$  is bounded periodic or quasi-periodic; the component on  $T_s$  will converge to 0 as

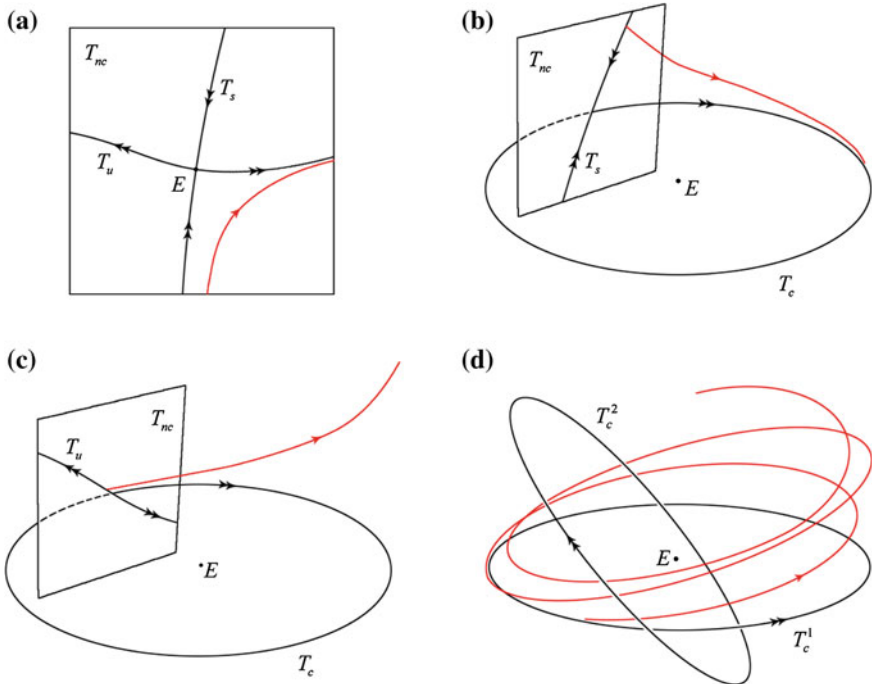


**Fig. 3.7** The behaviours of general orbits in the neighbourhoods of equilibrium points  $E_1$  and  $E_2$ . The double arrows indicate the local manifolds tangent with corresponding subspaces, and the red lines indicate a general orbit. **a** Motion on  $T_{nc}$ . **b** Motion initialized with components on  $T_s$  and  $T_c$ . **c** Motion initialized with components on  $T_u$  and  $T_c$ . **d** Motion on  $T_c$ .

$t \rightarrow \infty$ ; and the component on  $T_u$  will be dominant as  $t \rightarrow \infty$ , leading to a divergence from the equilibrium point.

### 3.5.2 Behaviours of Trajectories Near $E_3$ and $E_4$

The linearized matrix  $\mathbf{B}$  at equilibrium point  $E_3/E_4$  has four opposite conjugate eigenvalues  $\pm\alpha \pm \beta_1 i$  and a pair of opposite purely imaginary eigenvalues  $\pm\beta_2 i$ . The motion modes corresponding to these blocks are

$$e^{\alpha t} \begin{bmatrix} \cos\beta_1 t & -\sin\beta_1 t \\ \sin\beta_1 t & \cos\beta_1 t \end{bmatrix}, e^{-\alpha t} \begin{bmatrix} \cos\beta_1 t & -\sin\beta_1 t \\ \sin\beta_1 t & \cos\beta_1 t \end{bmatrix}, \begin{bmatrix} \cos\beta_2 t & -\sin\beta_2 t \\ \sin\beta_2 t & \cos\beta_2 t \end{bmatrix}, \quad (3.30)$$

which correspond to the motion on the unstable subspace  $T_u$ , stable subspace  $T_s$  and centre subspace  $T_c$ . The general motion in the neighbourhoods of  $E_3$  and  $E_4$  is composed of these patterns, as illustrated in Fig. 3.8:

- Figure 3.8a shows the motion patterns on  $T_{nc}$  ( $\dim(T_{nc}) = 4$ ). The initial state  $y$  includes both components on  $T_u$  and  $T_s$ , which form a saddle-focus point at the equilibria  $E$  (representative for  $E_3$  or  $E_4$ ). Thus, the general motion form on  $T_{nc}$  is to spiral out from the unstable manifold and spiral into the stable manifold.
- Figure 3.8b shows the general pattern of an orbit initialized with both components on  $T_s$  and  $T_c$ , where the periodic circle indicates the centre manifold. The general motion form in this case is to approach the centre manifold in a spiral way.
- Figure 3.8c shows the general pattern of an orbit initialized with both components on  $T_u$  and  $T_c$ , in which case the unstable manifold takes the dominant role and the general motion form is to escape from the centre manifold in a spiral way.

As a summary, in the neighbourhoods of  $E_3/E_4$  of Kleopatra, the motion on  $T_c$  is bounded and periodic; the component on  $T_u$  is the dominant role, leading to a

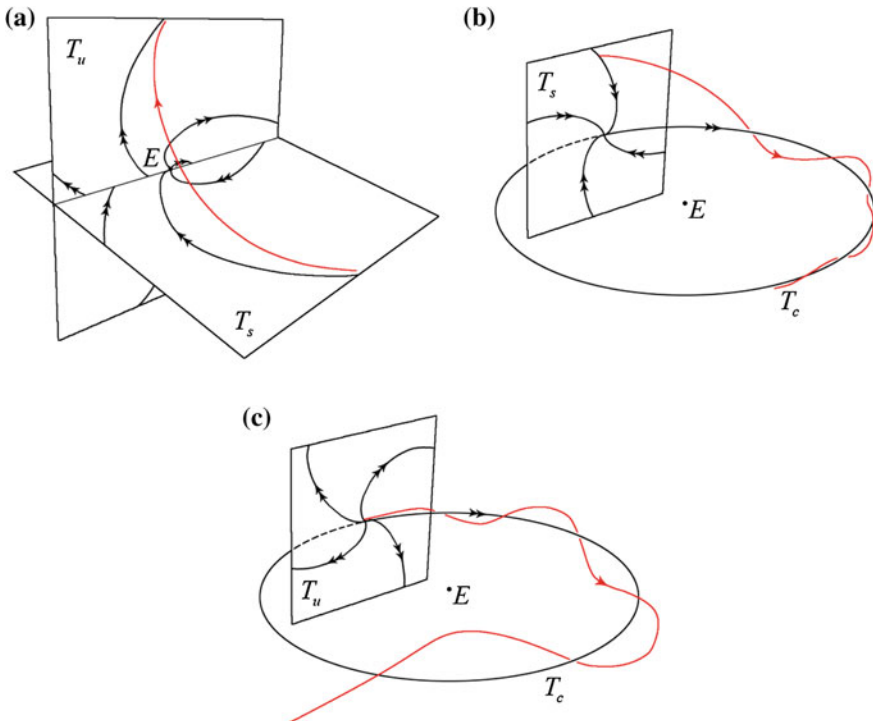


**Fig. 3.8** The behaviours of general orbits in the neighbourhoods of equilibrium points  $E_3$  and  $E_4$ . The double arrows indicate the local manifolds tangent with corresponding subspaces, and the red lines indicate a general orbit. **a** Motion on  $T_{nc}$ . **b** Motion initialized with components on  $T_s$  and  $T_c$ . **c** Motion initialized with components on  $T_u$  and  $T_c$ .

divergence from the equilibrium point, and the divergence speed is slower than that of  $E_1/E_2$ ; and the component on  $T_s$  will converge to 0 as  $t \rightarrow \infty$ .

### 3.6 Summary

This chapter discussed the orbital behaviours at and near the equilibrium points of small bodies. Four equilibrium points were found around asteroid Kleopatra with its gravitational field approximated by polyhedral method. Then via analysing the geometric dependence of zero-velocity surface on Jacobi integral, we determined the accessible region around Kleopatra with special attention paid to the corresponding special orbits.

The 4 equilibrium points of Kleopatra  $E_1-E_4$  prove to be unstable using Lyapunov stability theory, and we present  $E_1$ ,  $E_2$  are topologically equivalent, and  $E_3$ ,  $E_4$  are topologically equivalent. The motion around the equilibrium point is decomposed into three types of local manifolds, stable manifold, unstable manifold and centre manifold, and by extending the periodic motion on centre manifolds, we have found 6 periodic orbit families around  $E_1-E_4$ , which exist in relatively large scales. And we prove the all these periodic orbit families are unstable, consistent with the stabilities of corresponding equilibrium points.

Furthermore, at the last section a qualitative analysis of the general motion around the equilibrium points  $E_1-E_4$  is presented. Based on linearization methodology, we showed 4 typical motion patterns in the neighbourhoods of  $E_1/E_2$ : the motion on non-centre manifold, the motion approaching centre manifold, the motion departing from centre manifold and the motion on centre manifold, which sketch out the general orbital behaviours around  $E_1$  and  $E_2$ . Likewise, we showed 3 typical motion patterns in the neighbourhoods of  $E_3/E_4$ : the motion on non-centre manifold, the motion approaching and departing from centre manifold, which determine the general orbital behaviours around  $E_3$  and  $E_4$ .

As an aside, the discussion of this chapter is mostly based on asteroid Kleopatra, while the ideas and approaches employed can be portable to a large group of small bodies described by Eq. 2.22, especially for those involving qualitative properties of such systems.

## References

1. Ostro SJ, Hudson RS, Nolan MC et al (2000) Radar observations of asteroid 216 Kleopatra. *Science* 288:836–839
2. Descamps P, Marchis F, Berthier J et al (2011) Triplicity and physical characteristics of asteroid (216) Kleopatra. *Icarus* 211:1022–1033
3. Szebehely V (1967) Theory of orbits: the restricted problem of three bodies. Academic Press Inc., New York
4. Liu Y, Chen L (2001) Nonlinear vibration. Higher Education Press, Beijing

5. Hu W, Scheeres DJ (2004) Numerical determination of stability regions for orbital motion in uniformly rotating second degree and order gravity fields. *Planetary and Space Science* 52:685–692
6. Perko L (1991) Differential equation and dynamical system. Springer, New York

# Chapter 4

## Topological Classification and Stability of Large-Scale Periodic Orbits

**Abstract** Periodic orbit is one of the most important issues among all kinds of large-scale motion types, and has been regarded as the breakthrough of three-body problem by Poincaré. Specifically, to orbital dynamics around small bodies, there are at least two reasons for us to focus on the periodic motion, which is related to orbital evolution of real small body system, and is crucial for mission design of approaching the target body. Differing from equilibrium points, to search periodic orbits in the phase space is still an art to date, especially for the highly dimensional systems like Eq. 2.23. The orbital motion equation near a small body Eq. 2.22 has similar formulation with the equation of CRTBP, which suggests that it might include periodic motion of the same level of abundance as the latter. This chapter starts with a specific asteroid. Section 4.2 proposes an algorithm to search large-scale periodic orbits around irregular bodies, which is then applied to find out the periodic orbital families of the target small body. Section 4.3 surveys the stabilities of these orbits, and Sect. 4.4 further describes the topologies of different orbital families, based on which a classification method is proposed to track the topological evolution. Section 4.5 discusses the general motion forms about the periodic orbits, which discriminates different orbital patterns according to the linearized map on the section.

**Keywords** Hamiltonian systems · Asteroid 216 Kleopatra · Periodic orbits · Computer methods · Continuation methods · Methods: analytical · Methods: data analysis · Stability

### 4.1 Introduction

The transition form the motion near equilibria to large-scale motion is a common train of thought for the study of nonlinear dynamics. Periodic orbit is one of the most important issues among all kinds of large-scale motion types, and has been regarded as the breakthrough of three-body problem by Poincaré. Specifically to orbital dynamics around small bodies, there are at least two reasons for us to focus on the periodic motion: first, periodic orbits are related with orbital evolution of small body system, e.g. the formation of natural satellites; second, to understand the

distribution of periodic orbits is crucial for mission design of approaching the target body, and a stable periodic orbit serve as the common reference for parking orbit around a small body.

Differing from equilibrium points, to search periodic orbits in the phase space is still an art to date, especially for the highly dimensional systems like Eq. 2.23 (in fact, even to determine the upper bound for the number of limit cycles in 2 dimensional system remains unsolved, known as Hilbert's 16th problem) [1]. The orbital motion equation near a small body Eq. 2.22 has similar formulation with the equation of CRTBP, which suggests it might include periodic motion of the same level of abundance as the latter. While the biggest difference of system Eq. 2.22 compared to CRTBP is the breaking of symmetries, i.e. there is no symmetric planes for the gravitational field of a real small body, thus several mature techniques developed for searching periodic orbits of CRTBP will be invalid in this case.

The chapter starts with a specific asteroid. Section 4.2 proposes an algorithm to search large-scale periodic orbits around irregular bodies, which is then applied to find out the periodic orbital families of the target small body. Section 4.3 surveys the stabilities of these orbits, and Sect. 4.4 further describes the topologies of different orbital families, based on which a classification method is proposed to track the topological evolution. Section 4.5 discusses the general motion forms about the periodic orbits, which discriminates different orbital patterns according to the linearized map on the section.

## 4.2 Periodic Orbits Around 216 Kleopatra

Most previous studies on the large-scale orbital behaviours around small bodies are based on simple gravitational models, e.g. massive line segment, homogenous ellipsoid, etc. And in these cases, detail loss of system dynamics can be inevitable due to the rough approximation. Considering the effects of non-spherical perturbation on the orbital motion, this chapter continues using the polyhedral gravitational model and take Kleopatra as an example (reasons described in Sect. 3.2).

Given arbitrary periodic orbit of system Eq. 2.24,  $\mathbf{x}^*$  with period  $T$ , that is

$$\mathbf{x}^*(t) = \mathbf{x}^*(t + T), \quad \forall t \in \mathbb{R}. \quad (4.1)$$

According to the analysis in Sects. 2.4 and 3.2,  $\mathbf{x}^*$  has following features:

1. All the states on  $\mathbf{x}^*$  correspond to the same Jacobi integral  $C$ , and the position of  $\mathbf{x}^*$  in configuration space is constrained by the forbidden region determined by  $C$ . Thus, Jacobi integral will be taken as an important index for considering the dependence of periodic orbit.
2. Equation 2.24 describes a conserved Hamiltonian system, which ensures the periodic solution  $\mathbf{x}^*$  is not isolated, i.e. other periodic solutions exist within arbitrarily small neighbourhood around  $\mathbf{x}^*$ .

Besides, CRTBP takes the similar form of motion equations as Eq. 2.24, and for the former system, Poincaré conjectured that periodic orbits are dense in phase space, i.e. periodic motion exists within arbitrarily small neighbourhood in phase space, which is supported by a lot of evidences in numeric and theory, while has not been proved to date [2]. It may suggest that periodic orbits of system Eq. 2.24 could also be dense, which leads to the idea that periodic motion can be employed as the reference of the general forms of large-scale motion. And this gives clue to understanding the global dynamics of such systems in the following studies.

### 4.2.1 Hierarchical Grid Search Method

The grid search of periodic orbits was proposed during the studies on CRTBP [3], and has been applied successfully as the development of computing techniques. The basic idea of this algorithm is to divide a feasible range into meshes, and check the values at the nodes to approach the periodic solution. It gives a global search scheme within specified ranges, and the efficiency could be improved with optimized strategies.

The grid search is appropriate for planar CRTBP because the problem cloud be reduced to two dimensions based on symmetry and the Jacobi constant. However, searching 3-dimensional periodic orbits around asteroids is complicated because of the irreducibility of system Eq. 2.24. A straight grid search performed over this high-dimensional system would be inefficient due to the vast computational cost.

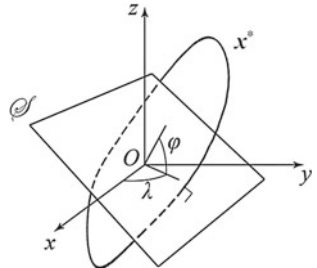
In this section, we combined the classical grid search method with a hierarchical parametrization to implement a systematic global search of 3-dimensional periodic orbits around asteroids with any multiplicity. Briefly, a special kind of Poincaré section is defined, based on which the Cartesian position and velocity are represented in the form of hierarchical parameters, and then divide the new parameter space into meshes and calculate the orbits extending from each node. The results at the nodes will present the initial guess for the periodic solution, and the precise periodic orbit will be obtained by iteration. These individual periodic orbits, serving as seeds, will be further applied in the continuation, which leads to a continuous orbital family for each iterative result. The algorithm is detailed as follows:

#### 1. Re-parameterization

For given periodic motion  $\mathbf{x}^*$ , define a Poincaré section  $\mathcal{S}$  in the body fixed frame  $Oxyz$ , subject to: I. plane  $\mathcal{S}$  spreading through the origin  $(0, 0, 0)$ ; II.  $\mathcal{S}$  is perpendicular to  $\mathbf{x}^*$ . Define the tangential direction of  $\mathbf{x}^*$  at the vertical intersection is the positive normal direction of  $\mathcal{S}$ , as shown in Fig. 4.1.

It is worth noting that such section exists for arbitrary smooth periodic orbit  $\mathbf{x}^*$ . Here is a concise proof: it is equivalent to the proposition that for any smooth spatial closed curve  $\mathbf{r}(l)$ , there exists  $0 < l < L$  so that  $\mathbf{r} \cdot \mathbf{r}' = 0$  ( $l$  is the arc length,  $L$  is the circumference of  $\mathbf{r}(l)$ , and  $\mathbf{r}'$  indicates the derivative of  $\mathbf{r}$  to  $l$ ).

**Fig. 4.1** Poincaré section associated with periodic orbit  $\mathbf{x}^*$



If  $\mathbf{r} \cdot \mathbf{r}' = 0.5(\mathbf{r} \cdot \mathbf{r})' = 0.5(|\mathbf{r}|^2)'$  never turns to 0, the radial length  $|\mathbf{r}|$  would monotonically vary as  $l$ , which is in conflict with the premise “closed curve”. Resetting the start time to the vertical intersection point,  $\mathbf{x}^*$  could be mapped to a 5-dimensional parameter set: the angles  $\lambda, \varphi$  describe the orientation of section  $S$ , which also defines the local frame of  $S$  by two rotations. The initial position of  $\mathbf{x}^*$  is determined by  $\lambda, \varphi$  and local coordinates  $u, v$ , and the initial speed is determined by Jacobi integral  $C$ .

$$\begin{aligned} \begin{bmatrix} x_0 \\ y_0 \\ z_0 \end{bmatrix} &= \begin{bmatrix} -v \cos \lambda \sin \varphi - u \sin \lambda \\ -v \sin \lambda \sin \varphi + u \cos \lambda \\ v \cos \varphi \end{bmatrix}, \\ \begin{bmatrix} \dot{x}_0 \\ \dot{y}_0 \\ \dot{z}_0 \end{bmatrix} &= \sqrt{2(C - V)} \begin{bmatrix} \cos \lambda \cos \varphi \\ \sin \lambda \cos \varphi \\ \sin \varphi \end{bmatrix}. \end{aligned} \quad (4.2)$$

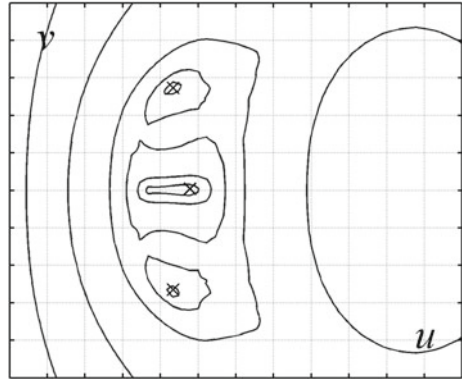
Equation 4.2 presents the map from the Cartesian initial state  $(x_0, y_0, z_0, \dot{x}_0, \dot{y}_0, \dot{z}_0)$  to the hierarchical parameters  $(C, \lambda, \varphi, u, v)$ , which has a lot of advantages: first, the number of parameters is reduced to 4 (the Jacobi integral is not included in grid search); second, it is easy to estimate the feasible ranges for all the 5 parameters, i.e. the value of  $C$  is limited by the accessible regions (see Sect. 3.2),  $\lambda, \varphi$  are angles and  $u, v$  reflect the radial distance to the small body; third, the repetitive search over the Cartesian initial states those belong to the same orbit could be avoided by using hierarchical parameters.

## 2. Global search for initial guess

Within the search for initial guess, the Jacobi integral  $C$  is fixed, and then a dual grid search over parameter pairs  $(\lambda, \varphi)$  and  $(u, v)$  is performed in loops:  $-\pi < \lambda < \pi$ ,  $-\pi/2 < \varphi < \pi/2$  for the outer loop, and  $-R_3 < u < R_3$ ,  $-R_3 < v < R_3$  for the inner loop (the upper limit  $R_3$  is defined as in Sect. 2.2). Since the periodic orbits affiliated to a specific section are isolated on  $S$ , the inner loop gives the rough solutions to these periodic orbits. Equation 4.3 defines the state residual of an orbit with multiplicity  $N$ .

$$\mathbf{x}_{res} = \mathbf{x}_N - \mathbf{x}_0, \quad (4.3)$$

**Fig. 4.2** An example of the contour lines of  $|\mathbf{x}_{res}|$  in local frame. The *mesh grid* indicate the division over parameters  $u$  and  $v$ , and the *cross* indicates the possible periodic orbits



in which  $\mathbf{x}_0, \mathbf{x}_N$  are the starting and final states when the orbit starts and returns to the section for  $N$  times along the positive normal direction. Obviously, a periodic orbit has residual  $\mathbf{x}_{res}^* = 0$ , and the distribution of  $|\mathbf{x}_{res}|$  shows the possible locations of periodic solutions on  $\mathcal{S}$ . Figure 4.2 illustrates the counter lines of  $|\mathbf{x}_{res}|$  over  $uv$ -plane as an example.

As shown in Fig. 4.2, under the expression of new parameter set, periodic orbits of specified Jacobi integral are assigned to a lot of sections determined by the orientation angles, thus only isolated solutions of finite number exist on each section. Namely, it provides a systematic scheme to search over the parameter space, which is a comprehensive one that efficiently avoids omission and duplication.

### 3. Local iteration

The systematic search on the section's mesh grid gives the initial guess for periodic orbits, and the exact solutions are obtained by local iterative algorithm. In this chapter we employ a modified Powell's hybrid method to solve the equations of periodic orbits:

$$\begin{aligned} \mathbf{x}_0 &= \mathbf{x}(T; \mathbf{x}_0), \\ H(\mathbf{x}_0) &= C. \end{aligned} \tag{4.4}$$

Equation 4.4 includes 7 variants  $\{T; \mathbf{x}_0\}$ . Besides, in case of low iterative efficiency, a relaxation of the constant  $C$  might be necessary to improve the convergence speed.

### 4. Numeric continuation of periodic orbits

The composition of periodic motion set with specified Jacobi integral  $C$  is determined in numeric from above steps. Then, the last step of our strategy is to extend the obtained orbits into periodic families over a range of  $C$ , which is ensured to exist due to the continuous dependence of periodic motion on Jacobi integral.

For a given periodic orbit with the initial state,  $\mathbf{x}_0^i$ , Eq. 4.5 presents the steepest decent direction of Jacobi integral at  $\mathbf{x}_0^i$ .

$$\xi = \frac{\partial H}{\partial x} = \begin{bmatrix} \nabla V \\ \dot{r} \end{bmatrix}. \quad (4.5)$$

Equation 4.6 presents the initial guess of a neighbour periodic orbit, in which the step length  $\epsilon$  is chosen based on the convergence domain of the iterative algorithm.

$$x_0^{i+1} = x_0^i + \epsilon \hat{\xi}. \quad (4.6)$$

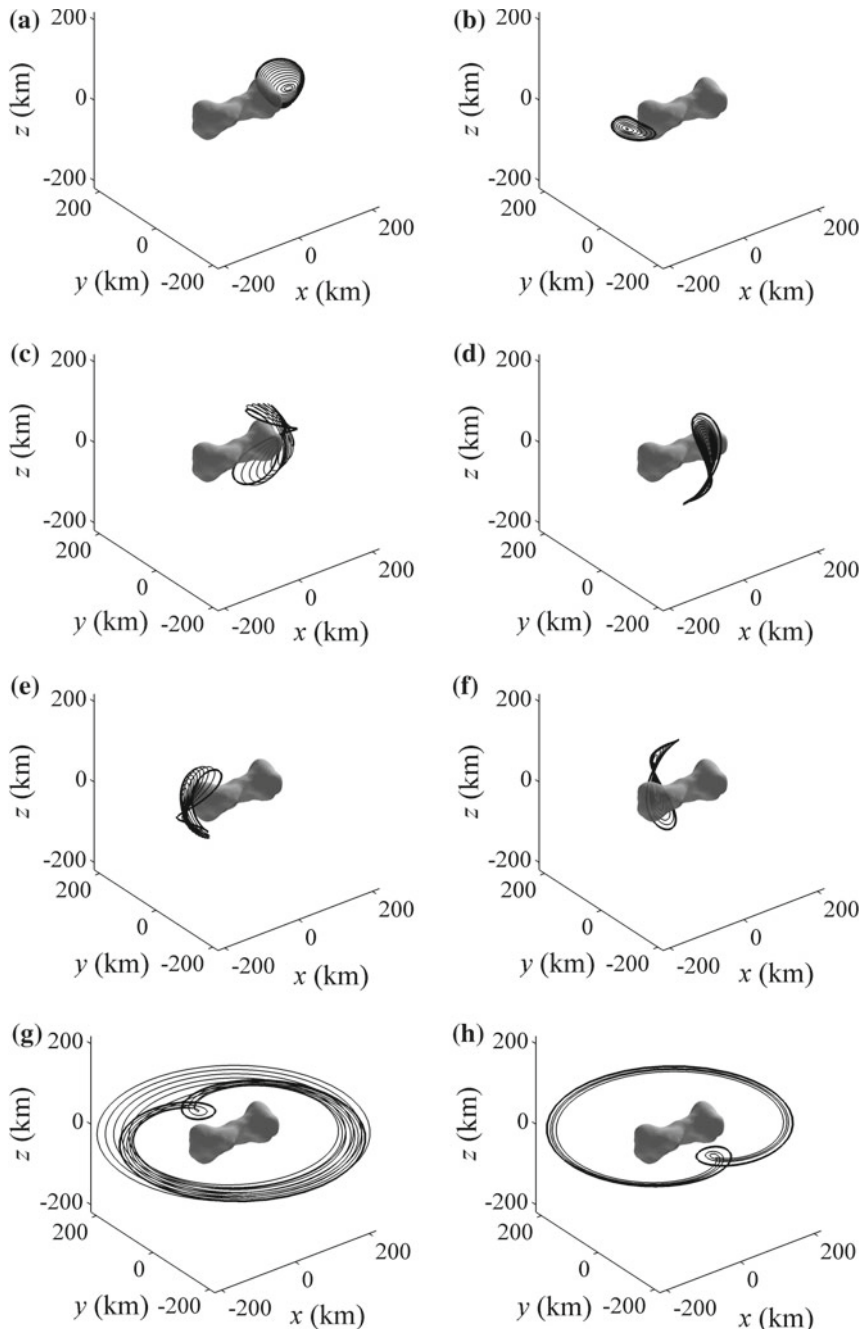
Then by performing the local iteration as described in step 3, the precise solution to the extended periodic orbit will be settled on in numeric. And recall these routines, a continuous family of periodic orbits will be exposed out of the phase space.

These 4 steps described a complete strategy for searching periodic orbits around a small body. Besides, it is worth noticing the global search could be speed up through a preliminary screening, i.e. the nodes as follows could be skipped: I. lying inside the small body or the forbidden region outlined by Jacobi integral; II. with orbital energy much greater than 0 (escaping orbit).

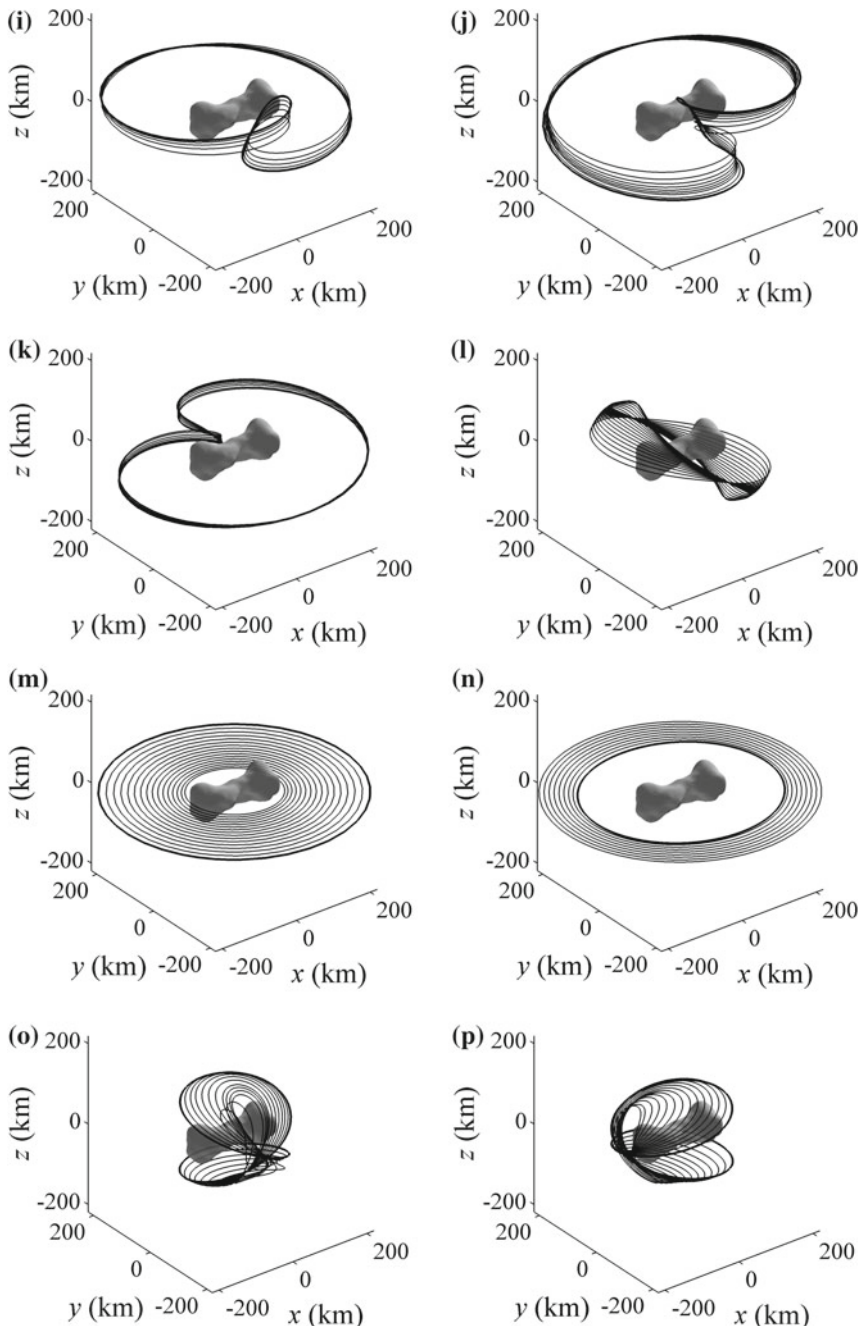
#### 4.2.2 Families Generated Around Kleopatra

A FORTRAN code of the Hierarchical Grid Search Method is developed and applied to asteroid Kleopatra. Scheeres et al. have ever presented 6 periodic orbit families around Castalia, which has a similar prolate shape. This section shows the results of our search over a wide range. The parameters of Kleopatra have been stated in Sect. 3.2.1. Special attention is paid to the simple periodic orbits, defined as the number of returns  $N < 3$  (a “return” is counted when the orbit passing through the section in positive direction). Global searches are performed respectively at  $C = -3.0 \times 10^{-3} \text{ km}^2/\text{s}^2, -2.5 \times 10^{-3} \text{ km}^2/\text{s}^2, -2.0 \times 10^{-3} \text{ km}^2/\text{s}^2$  and  $-0.5 \times 10^{-3} \text{ km}^2/\text{s}^2$ . A  $36 \times 36$  mesh is adopted for the outer loop of angles  $-\pi < \lambda < \pi$ ,  $-\pi/2 < \varphi < \pi/2$ , and a  $100 \times 100$  mesh is used for the inner loop over local coordinates  $-228 \text{ km} \leq u \leq 228 \text{ km}, -228 \text{ km} \leq v \leq 228 \text{ km}$  ( $R_3 = 228 \text{ km}$  for Kleopatra, see Sect. 2.2). Thus for a specific value of Jacobi integral,  $\sim 1.3 \times 10^7$  mesh nodes need to be checked, which takes approximately 12 days on an Intel Core i7 PC with 2 GB RAM. The results, after processed with Steps 3 and 4, eventually boil down to 29 periodic orbit families, as illustrated in Fig. 4.3.

Figure 4.3 shows a morphological classification of the periodic orbits: families 1–6 can be viewed as continuation of the local periodic orbits about the equilibria of Kleopatra, or perturbed stationary orbits in the inertia frame  $OXYZ$ ; families 7 and 8 are quasi-equatorial elliptic orbits with  $180^\circ$  phase differences in  $OXYZ$ ; families 9–11 are orbits out of the equatorial plane, viewed as the superposition of an in-plane quasi-elliptic motion and a vertical motion; family 12 indicates the incline orbits out of the equatorial plane; families 13 and 14 are retrograde and prograde quasi-circular



**Fig. 4.3** (continued)

**Fig. 4.3** (continued)

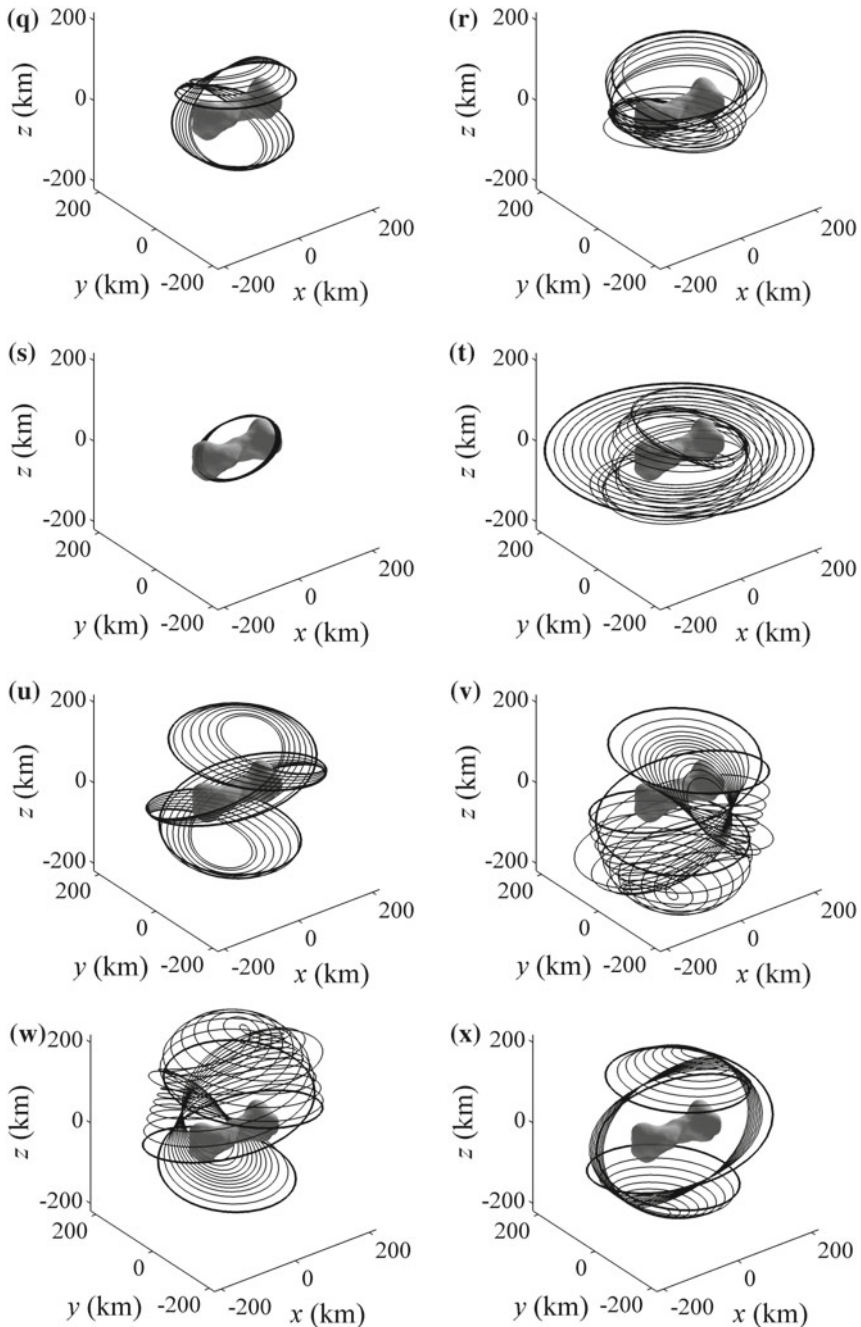
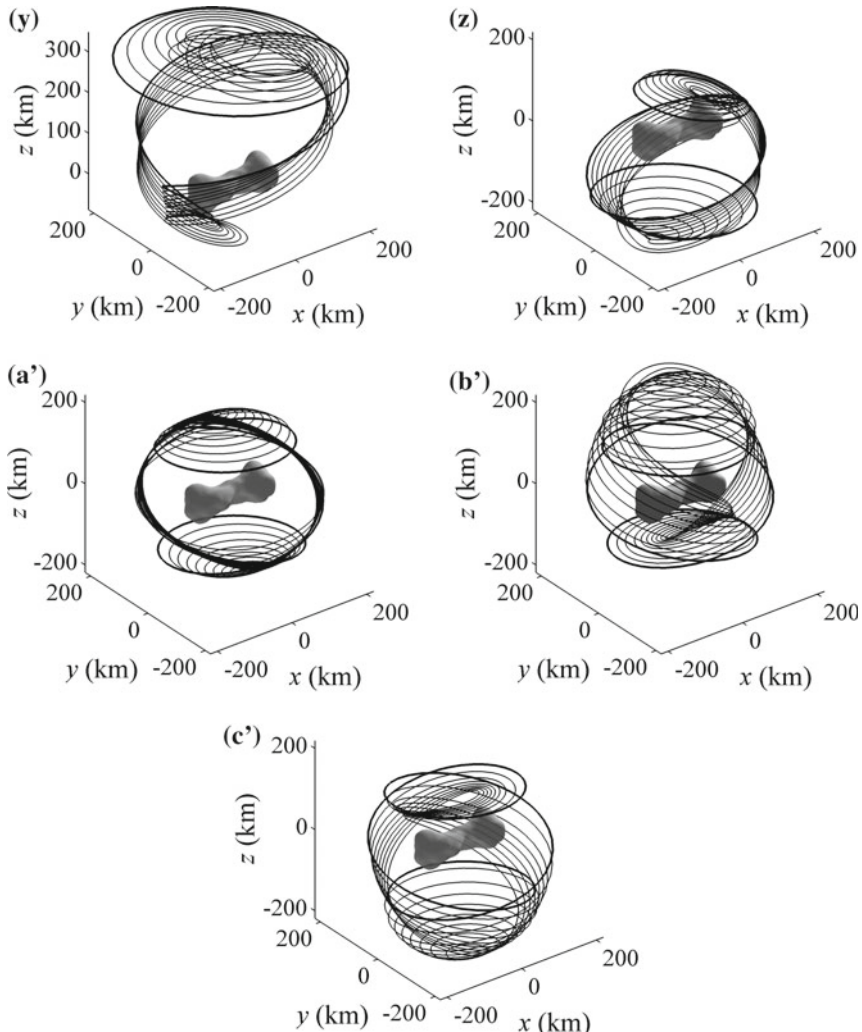


Fig. 4.3 (continued)



**Fig. 4.3** 29 families of periodic orbits in the vicinity of Kleopatra. The *bold line* indicates the representative orbit out of each family. **a** Family. **b** Family 2. **c** Family 3. **d** Family 4. **e** Family 5. **f** Family 6. **g** Family 7. **h** Family 8. **i** Family 9. **j** Family 10. **k** Family 11. **l** Family 12. **m** Family 13. **n** Family 14. **o** Family 15. **p** Family 16. **q** Family 17. **r** Family 18. **s** Family 19. **t** Family 20. **u** Family 21. **v** Family 22. **w** Family 23. **x** Family 24. **y** Family 25. **z** Family 26. **a'** Family 27. **b'** Family 28. **c'** Family 29

orbits near the equatorial plane, and the retrograde family includes stable members close to the surface of Kleopatra; families 15–17 correspond to families 5, 6 and 4, respectively, and their periods are nearly twice as much as the rotational period of Kleopatra; families 18 and 19 present two types of asymmetric double orbits, and

the latter extends to the equatorial plane as Jacobi integral increasing; family 20 is a special type of incline orbits with a narrow range of Jacobi integral, which cycles around the “neck” of Kleopatra close to the surface; and families 21–29 are multiple periodic orbits, which are quasi-elliptic in  $OXYZ$  with different inclinations.

As listed, the periodic orbits found around Kleopatra are far more than those found around Castalia in previous studies. It is a numeric validation of our method, and on the other side, it also gives some clues to the diversity of periodic motion around small bodies. In fact, the numeric searching algorithms can never traverse all patterns of periodic motion, and the sample orbits listed in this section should be only a tip of the iceberg. The aim of this work is to provide examples as various as possible, to feed to our understanding of large-scale motion near the small bodies, and to verify the theoretical explorations.

### 4.3 Stability of Families 1–29

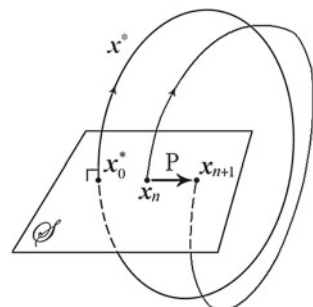
In order to determine the stability of the periodic orbit  $\mathbf{x}^*$  in system Eq. 2.24, we check the orbital behaviours in its neighbourhood using Poincaré map. The section  $\mathcal{S}$  defined in Sect. 4.2.1 is adopted here, and the initial state of a periodic orbit  $\mathbf{x}_0^*$  lies in  $\mathcal{S}$ . According to the continuous dependence of solutions to Eq. 2.24 on the initial condition, orbits starting from a sufficiently small neighbourhood of  $\mathbf{x}_0^*$  will pass through  $\mathcal{S}$  again after  $\sim 1T$ . Assuming the  $n$ th intersection of arbitrary orbit  $\mathbf{x}$  with  $\mathcal{S}$  to be  $\mathbf{x}_n$  (Fig. 4.4), Poincaré map is defined as

$$P : \mathbf{x}_n \rightarrow \mathbf{x}_{n+1}, \quad n \in \mathbb{N}. \quad (4.7)$$

Equation 4.7 describes a discrete dynamical system, and obviously,  $\mathbf{x}_0^*$  forms an equilibria of  $P$ . Then the stability of periodic orbit  $\mathbf{x}^*$  is equivalently transformed to that of the equilibria  $\mathbf{x}_0^*$  in system Eq. 4.7.

Following a similar process as presented in Sect. 3.4, the map Eq. 4.7 will be linearized at  $\mathbf{x}_0^*$ . Since the state transformation function of system Eq. 2.24 satisfies

**Fig. 4.4** The Poincaré map



$$\phi(T; \mathbf{x}_0^*) = \mathbf{x}_0^*, \quad (4.8)$$

the linearized matrix of Eq. 4.7 at  $\mathbf{x}_0^*$  yields

$$\mathbf{M} = \frac{\partial \phi(T; \mathbf{x}_0^*)}{\partial \mathbf{x}_0}. \quad (4.9)$$

In which  $\mathbf{M}$  is the monodromy matrix. Note that for system Eq. 2.24, the definition Eq. 4.9 is equivalent with that by Eq. 3.19, which describes the propagation of an initial disturb  $\delta \mathbf{x}$  within one period  $T$ . The linearized map is written as

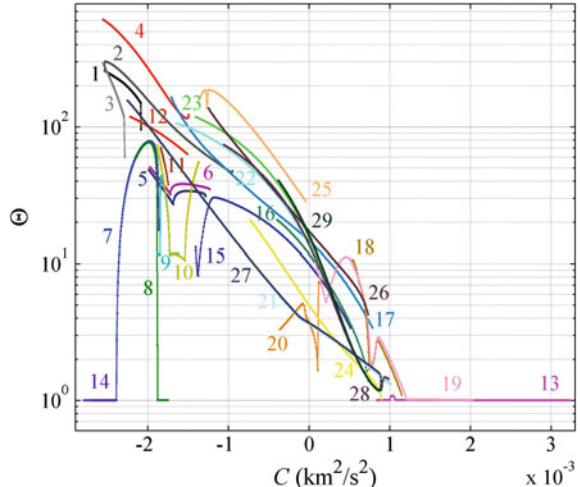
$$\delta \dot{\mathbf{x}} = \mathbf{M} \delta \mathbf{x}. \quad (4.10)$$

Then the eigenvalues  $\eta_i$  ( $i = 1, 2, \dots, 6$ ) of matrix  $\mathbf{M}$  are defined to be the multipliers of periodic orbit  $\mathbf{x}^*$ . Reference [4] have stated that  $\mathbf{M}$  is symplectic, and recall some important properties:

1. If  $\eta$  is an eigenvalue of  $\mathbf{M}$ , then  $\eta^{-1}, \bar{\eta}, \bar{\eta}^{-1}$  are also the eigenvalues of the same multiplicity;
2.  $\text{set}(\mathbf{M}) = 1$ , and the multiplicity of eigenvalues  $\pm 1$  (if existent) must be even;
3.  $\mathbf{M}$  has a trivial eigenvalue  $+1$  with a multiplicity of at least 2.

In Sect. 3.4.3, we have discussed about the stability of a periodic orbit  $\mathbf{x}^*$  by using the characteristic factor  $\Theta$ . As for the structurally stable orbits (none of the multipliers lies on the unit circle), that method has been validated. However, since all the periodic orbits of system Eq. 2.24 prove to be structurally unstable (see the properties above), the critical cases must be faced in the stability analysis.

**Fig. 4.5** The characteristic factor of 29 families around Kleopatra varying as Jacobi integral. The orbital families are marked in *different colours* and indicated with corresponding numbers



Specifically, the 29 families of periodic orbits around Kleopatra include few orbits with multiple multipliers (except the trivial multiplier +1). Under the non-resonant cases, periodic orbits with  $\Theta = 1$  are regarded to be stable [5], and those with  $\Theta > 1$  are regarded to be unstable.

Figure 4.5 shows the variations of  $\Theta$  of the 29 families as Jacobi integral  $C$  increasing. As illustrated, the symmetrically located families show similar trends, e.g. families 1 and 2, 3 and 4, 5 and 6, 7 and 8, 15 and 16. Most families have  $\Theta > 1$  (unstable), and the orbits in families 13, 14 and part in families 7, 8, 19 satisfy  $\Theta = 1$  (stable).

**Table 4.1** The parameters of periodic orbit families 1–29 around Kleopatra (US for “unstable”, S for “stable”)

Family	$T$ (h)	$C$ ( $10^{-3}$ km $^2$ /s $^2$ )	Stability
1	3.94 – 4.11	–2.54 – –2.09	US
2	4.11 – 4.72	–2.54 – –0.95	US
3	3.74 – 3.79	–2.56 – –2.29	US
4	4.15 – 4.33	–2.56 – –1.49	US
5	5.34 – 5.62	–1.99 – –1.28	US
6	5.41 – 5.69	–1.97 – –1.24	US
7	6.93 – 10.06	–2.70 – –1.87	S → US
8	9.21 – 10.44	–2.15 – –1.74	US → S
9	10.34 – 10.44	–1.88 – –1.62	US
10	10.32 – 10.52	–1.88 – –1.37	US
11	10.48 – 10.49	–1.84 – –1.75	US
12	10.37 – 10.55	–2.22 – –1.51	US
13	2.33 – 4.98	–0.84 – 3.23	S
14	6.65 – 8.96	–2.79 – –2.40	S
15	4.79 – 6.13	–1.41 – 0.51	US
16	6.02 – 6.14	–0.40 – 0.78	US
17	4.21 – 6.02	–1.71 – 0.78	US
18	6.04 – 6.45	0.54 – 1.14	US
19	6.04 – 8.52	0.07 – 2.02	US → S
20	2.39 – 2.43	–0.36 – 0.15	US
21	10.79 – 11.06	–0.38 – 0.89	US
22	10.70 – 11.12	–1.65 – 1.01	US
23	10.80 – 11.12	–1.41 – 0.88	US
24	10.76 – 11.07	–0.73 – 0.90	US
25	15.19 – 16.13	–1.35 – –0.04	US
26	9.94 – 11.05	–1.25 – 0.73	US
27	10.48 – 11.05	–2.25 – 0.89	US
28	10.89 – 11.11	–1.06 – 0.98	US
29	11.05 – 11.11	–0.38 – 0.88	US

Table 4.1 lists the parameters of orbital families 1–29, including the period, Jacobi integral and stability. As illustrated, families 1–6 have periods of  $\sim 1T$ , and corresponding topology of the accessible region is shown as Fig. 3.3b–e; families 7–12 have periods of  $\sim 2T$ , and corresponding topology also covers the cases Fig. 3.3b–e; the retrograde orbits in family 13 have short periods and large Jacobi integral; the periods of the prograde orbits in family 14 range from  $1T$  to  $2T$ , and corresponding topology of the accessible region is shown as Fig. 3.3a and b; families 15–17 have periods of  $\sim 1T$ , and corresponding topology of the accessible region is like Fig. 3.3f; families 18, 19 are asymmetric retrograde families, with the period ranging from  $1T$  to  $2T$ ; family 20 has very short period and relatively large integral value; families 21–29 have periods of  $\sim 2T$ , and corresponding topology of the accessible region covers the cases Fig. 3.3c–f.

Among the 29 families of periodic orbits, only the equatorial families 13 and 14 are always stable; families 7 and 8 lead to an alteration of stability, which is correlated with the renounce of multipliers (see Sect. 4.4 for details).

## 4.4 Topological Classification of Periodic Orbits

Shilnikov proved in Ref. [6] that for any autonomous system, the eigenvalues of monodromy matrix  $\mathbf{M}$  are metric invariants, which are conserved under arbitrary smooth coordinate transformation. Namely, the characteristic multipliers  $\eta_i$  are intrinsic properties of periodic orbit  $\mathbf{x}^*$ , and the topology of  $\mathbf{x}^*$  completely depends on the 6 multipliers  $\eta_i$  ( $i = 1, 2, \dots, 6$ ). And for system Eq. 2.24, due to the existence of the double trivial multiplier +1, the topology of  $\mathbf{x}^*$  is actually determined by the other 4 multipliers  $\eta_1, \eta_2, \eta_3, \eta_4$ .

According to the symplectic properties of  $\mathbf{M}$ , the compositions of multipliers  $\eta_1\text{--}\eta_4$  are limited. Figure 4.6 shows a topological category of the periodic orbits, including 7 distributions of the 4 non-trivial multipliers.

As illustrated in Fig. 4.6a–d, the periodic orbits of saddle types are unstable, including the complex saddle, real saddle, central saddle and degenerated saddle; the general centre type (Fig. 4.6e) is stable; the degenerated centre type is a critical case, which could be stable like a general centre, or unstable due to the resonance; periodic orbits of identity type are special and usually appear in complete integrable systems.

Checking the 29 families about Kleopatra, 4 topological types are found according to this category: complex saddle (a), real saddle (b), central saddle (c) and general centre (e). Table 4.2 lists the paths of the topological transformations within these orbital families (as Jacobi integral  $C$  increasing).

The common features of the topological transformations are summarized as follows:

1. All the transformations are reversible, and two types may alternate in one family as Jacobi integral increasing, e.g. families 9, 10, 16, 21, 22, 23 and 28;

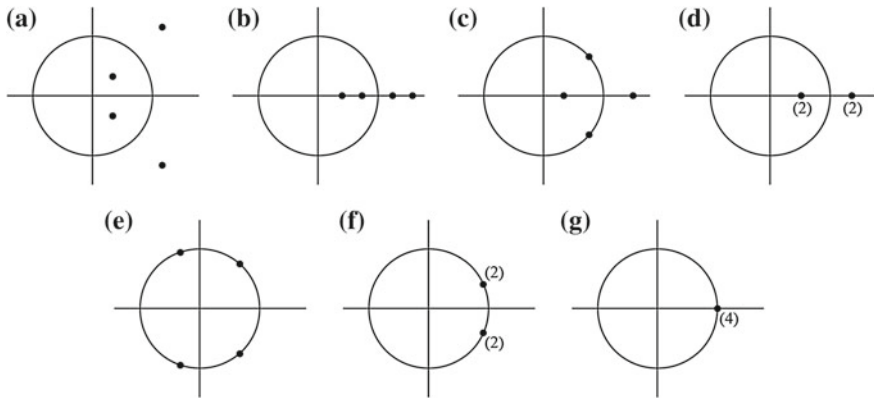


**Fig. 4.6** The distribution of 4 non-trivial multipliers on the complex plane. The *dots* indicate the positions of the multipliers relative to the *unit circle*, and the *bracketed number* indicates the multiplicity. **a** Complex saddle. **b** Real saddle. **c** Central saddle. **d** Degenerated saddle. **e** General center. **f** Degenerated center. **g** Identity

2. The approximately symmetric families show similar topological transformation, e.g. families 1 and 2, 3 and 4, 5 and 6, 7 and 8, 15 and 16, which is consistent with the stability analysis in Sect. 4.3;
3. All the stable periodic orbits out of the 29 families are found to be of general centre type (the critical case has not been found around Kleopatra).

Another information included in Table 4.2 is about the transform paths that the topological transformation does not occur between every two types. As for the 29 families, it exists between the complex saddle (a) and real saddle (b), real saddle (b) and central saddle (c), central saddle (c) and general centre (e). The topology sequence of each family is composed of these basic transformations. Figure 4.7 shows

**Table 4.2** The topological transformations of the 29 families around Kleopatra

1: c	11: b	21: b→a→b
2: c	12: c	22: c→b→c
3: c	13: e	23: c→b→c→b→c
4: c	14: e	24: c
5: a→b	15: b→c	25: b
6: a→b	16: c→b→c	26: b
7: e→c	17: b	27: b
8: c→e	18: b→c	28: c→b→c
9: a→b→a	19: b→c→e	29: b→c
10: b→a→b→c	20: a→b	

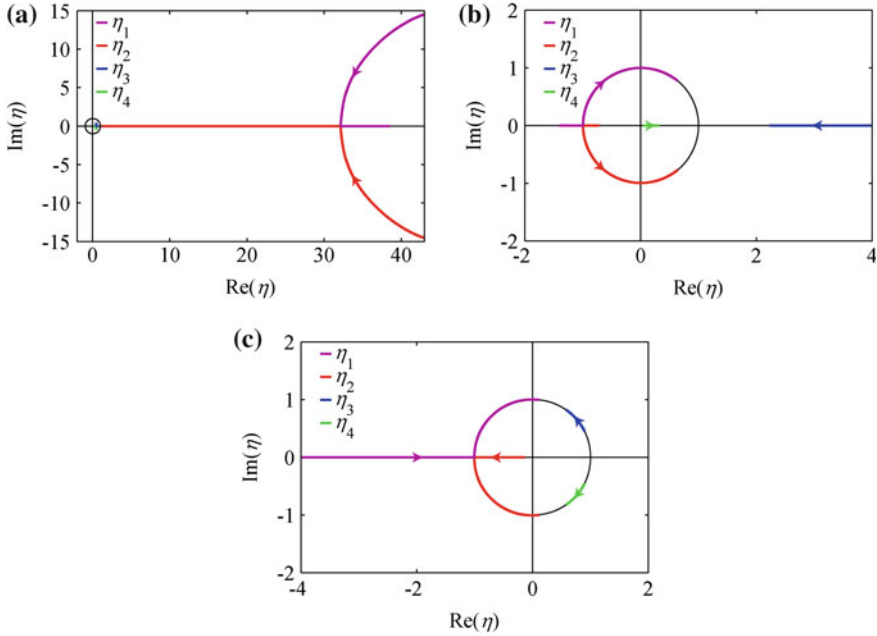


**Fig. 4.7** The example loci of 4 multipliers on the complex plane as  $C$  increasing, generated based on families 6, 15 and 7, respectively. **a** Family 6:  $a \rightarrow b$ . **b** Family 15:  $b \rightarrow c$ . **c** Family 7:  $c \rightarrow e$

examples for the three types of basic transformations: family 6 for type  $a \rightarrow b$ , family 15 for type  $b \rightarrow c$ , family 7 for type  $c \rightarrow e$ .

As illustrated in Fig. 4.7, the critical state between complex saddle and real saddle is a degenerated saddle (d); likewise, the critical state between real saddle and central saddle, or between centre saddle and general centre, is a multiple  $\pm 1$ . Beyond the critical states, all the periodic orbits from the 29 families fall into 4 types: a, b, c and e. The next section will discuss these topological types in detail.

## 4.5 Behaviours of Trajectories Near Periodic Orbits of 216 Kleopatra

This section discusses the general motion in the neighbourhood of periodic orbit  $x^*$ . As stated in Sect. 4.3, it is equivalent to studying the local behaviours of Poincaré map Eq. 4.7 at the equilibria  $x_0^*$ . Beginning with a linearized map  $T$ , due to Eq. 4.10, the perturbative form of Poincaré map  $P$  at  $x_0^*$  is

$$T : y_{n+1} = M y_n, \quad n \in \mathbb{N}. \quad (4.11)$$

In which  $\mathbf{y}_n = \mathbf{x}_n - \mathbf{x}_0^*$  defines the residual state of  $n^{\text{th}}$  return to section  $\mathcal{S}$ . The behaviours of discrete dynamical system Eq. 4.11 depend on the eigen structure of monodromy matrix  $\mathbf{M}$ . As for a real matrix,  $\mathbf{M}$  can be represented as its Jordan canonical form via similitude transformation, i.e. applying a transformation matrix  $\mathbf{N}$  subject to

$$\mathbf{M} = \mathbf{N} \begin{bmatrix} \mathbf{M}_1 & & \mathbf{O} \\ & \mathbf{M}_2 & \\ & & \ddots \\ \mathbf{O} & & \mathbf{M}_m \end{bmatrix} \mathbf{N}^{-1}, \quad (4.12)$$

where  $\mathbf{M}_j$  ( $j = 1, 2, \dots, m$ ) could be either a  $1 \times 1$  block, corresponding to a real multiplier  $\eta$ :

$$\mathbf{M}_j = \eta, \quad (4.13)$$

or a  $2 \times 2$  block, corresponding to a pair of conjugate complex multipliers  $e^{\alpha \pm \beta i}$ :

$$\mathbf{M}_j = e^\alpha \begin{bmatrix} \cos \beta & -\sin \beta \\ \sin \beta & \cos \beta \end{bmatrix}. \quad (4.14)$$

In which the case of multiple eigenvalues is not included. The general form of solution to Eq. 4.11 is represented as

$$\mathbf{y}_n = \mathbf{M}^n \mathbf{y}_0 = \mathbf{N} \begin{bmatrix} \mathbf{M}_1^n & & \mathbf{O} \\ & \mathbf{M}_2^n & \\ & & \ddots \\ \mathbf{O} & & \mathbf{M}_m^n \end{bmatrix} \mathbf{N}^{-1} \mathbf{y}_0 \quad (4.15)$$

And the diagonalized blocks satisfy

$$\mathbf{M}_j^n = \begin{cases} \eta^n & \text{if } \mathbf{M}_j = \eta \\ e^{n\alpha} \begin{bmatrix} \cos n\beta & -\sin n\beta \\ \sin n\beta & \cos n\beta \end{bmatrix} & \text{if } \mathbf{M}_j = e^\alpha \begin{bmatrix} \cos \beta & -\sin \beta \\ \sin \beta & \cos \beta \end{bmatrix} \end{cases} \quad (4.16)$$

Denoting the transformed state perturbation  $\mathbf{z}$ , and choosing the same blocking as  $\mathbf{y}$ :

$$\mathbf{z} = \mathbf{N}^{-1} \mathbf{y}_0 = \begin{bmatrix} z_1 \\ z_2 \\ \vdots \\ z_m \end{bmatrix}. \quad (4.17)$$

Equation 4.11 is represented as

$$\mathbf{y}_n = \mathbf{N} \begin{bmatrix} \mathbf{M}_1^n z_1 \\ \mathbf{M}_2^n z_2 \\ \vdots \\ \mathbf{M}_m^n z_m \end{bmatrix}. \quad (4.18)$$

Equation 4.18 shows the local behaviours of Poincaré map at  $\mathbf{x}_0^*$  depends on the linear combination of the motion modes corresponding to these blocks. And according to Sect. 4.4, the 6 multipliers of periodic orbits around Kleopatra  $\{1, 1, \eta_1, \eta_2, \eta_3, \eta_4\}$  are composed of following cases:

1. Complex saddle:  $\eta_i$  ( $i = 1, 2, 3, \dots, 4$ ) include 4 opposite conjugate complex numbers (length  $\neq 1$ );
2. Real saddle:  $\eta_i$  ( $i = 1, 2, 3, \dots, 4$ ) include 2 pairs of inverse real numbers (length  $\neq 1$ );
3. Central saddle:  $\eta_i$  ( $i = 1, 2, 3, \dots, 4$ ) include 2 inverse real numbers (length  $\neq 1$ ) and 2 conjugate complex numbers (length = 1);
4. General centre:  $\eta_i$  ( $i = 1, 2, 3, \dots, 4$ ) include 2 pairs of conjugate complex numbers (length = 1).

These 4 cases correspond to 4 types of local behaviours of the linearized system, which are topologically equivalent with the original system in the neighbourhood of  $\mathbf{x}^*$  (non-resonant cases). As stated in Sect. 4.4, almost all the 29 families of Kleopatra fall into these cases. The rest of this section will look into the general motion patterns near the 4 common types of periodic orbits.

#### 4.5.1 Periodic Orbits of Complex Saddle Type

For a periodic orbit of complex saddle type  $\mathbf{x}^*$ , the monodromy matrix  $\mathbf{M}$  has 4 non-trivial multipliers, denoted as  $e^{\pm\alpha\pm\beta i}$  ( $\alpha, \beta \in \mathbb{R}^+$ ), and the Jordan canonical form includes 4 blocks:

$$1, 1, e^\alpha \begin{bmatrix} \cos \beta & -\sin \beta \\ \sin \beta & \cos \beta \end{bmatrix}, e^{-\alpha} \begin{bmatrix} \cos \beta & -\sin \beta \\ \sin \beta & \cos \beta \end{bmatrix}. \quad (4.19)$$

Then, according to the combinations of the 4 blocks, motion around the periodic orbit can be decomposed into 3 basic maps

1. Identity map, i.e. the component of motion keeps invariant for every time returning to the section, corresponding to the first, second blocks;
2. Unstable focus map, i.e. the component of motion escapes from the origin in a spiral way (Fig. 4.8a), corresponding to the third block;

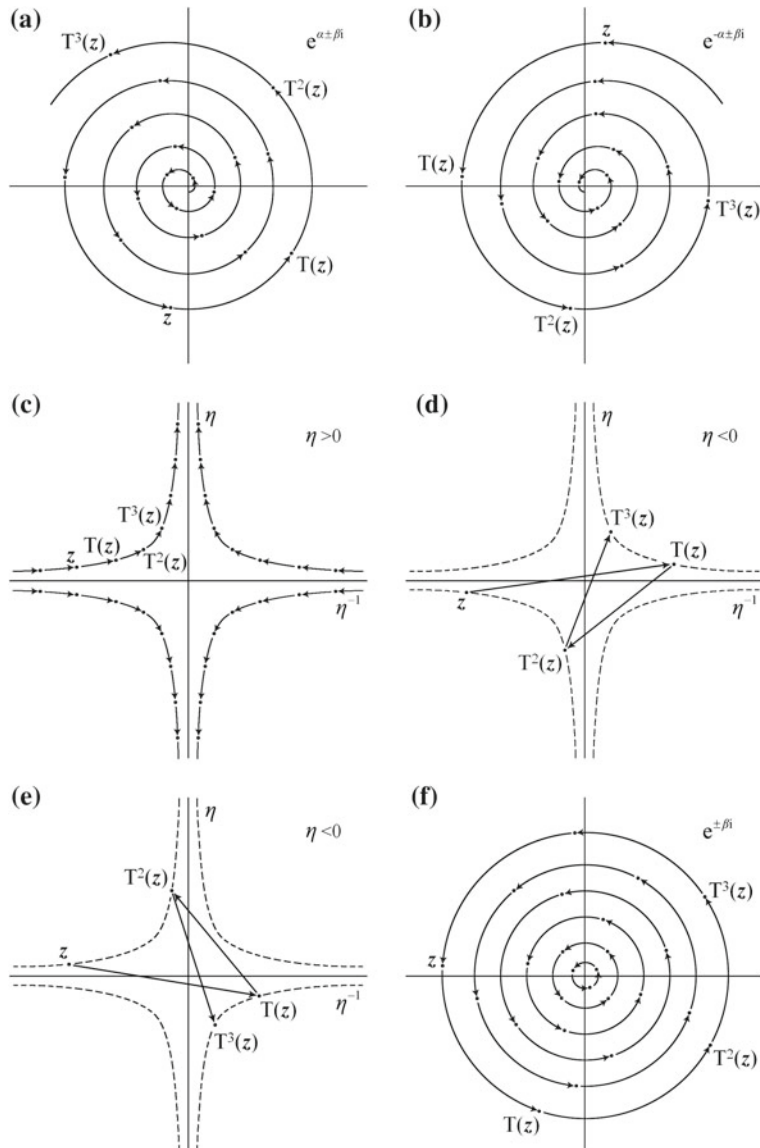


**Fig. 4.8** The basic forms of maps on Poincaré section for periodic orbits around Kleopatra. The arrows show the directions of the maps. **a** Unstable focus map. **b** Stable focus map. **c** Saddle map ( $\eta > 0$ ). **d** Saddle map ( $\eta < 0$ , starting from Quadrant I, III). **e** Saddle map ( $\eta < 0$ , starting from Quadrant II, IV). **f** Center map

3. Stable focus map, i.e. the component of motion approaches the origin in a spiral way (Fig. 4.8b), corresponding to the fourth block.

As a summary, the unstable focus map takes a dominant role among the three. Thus, the general motion around a periodic orbit of complex saddle type is to spiral away as time.

### 4.5.2 Periodic Orbits of Real Saddle Type

For a periodic orbit of real saddle type  $x^*$ , the monodromy matrix  $\mathbf{M}$  has 4 non-trivial multipliers, denoted as  $\eta_1, \eta_1^{-1}, \eta_2, \eta_2^{-1}$  ( $\eta_1, \eta_2 \in \mathbb{R}$ ), and the Jordan canonical form includes 6 blocks:

$$1, 1, \eta_1, \eta_1^{-1}, \eta_2, \eta_2^{-1} \quad (4.20)$$

The two pairs of inverse multipliers describe behaviours equivalent in topology. Then according to the combinations of the 6 blocks, motion around the periodic orbit can be decomposed into 2 basic maps:

1. Identity map, i.e. the component keeps invariant for every time returning to the section, corresponding to the first, second blocks;
2. Saddle map, i.e. the component shows hyperbolic motion corresponding to the third, fourth blocks (or the fifth, sixth blocks), and the path depends on the sign of  $\eta_1$  (or  $\eta_2$ ), as illustrated in Fig. 4.8c–e.

Among the above 2 maps, the unstable branch of the saddle map takes a dominant role, and the general motion around a periodic orbit of real saddle type is to escape away from it in an exponential way.

### 4.5.3 Periodic Orbits of Central Saddle Type

For a periodic orbit of central saddle type  $x^*$ , the monodromy matrix  $\mathbf{M}$  has 4 non-trivial multipliers, denoted as  $\eta, \eta^{-1}, e^{\pm\beta i}$  ( $\eta \in \mathbb{R}, |\eta| > 1, \beta \in \mathbb{R}^+$ ), and the Jordan canonical form includes 5 blocks:

$$1, 1, \eta, \eta^{-1}, \begin{bmatrix} \cos \beta & -\sin \beta \\ \sin \beta & \cos \beta \end{bmatrix} \quad (4.21)$$

Then, according to the combinations of the 5 blocks, motion around the periodic orbit can be decomposed into 3 basic maps

1. Identity map, i.e. the component keeps invariant for every time returning to the section, corresponding to the first, second blocks;

2. Saddle map, i.e. the component shows hyperbolic motion corresponding to the third, fourth blocks, and the path depends on the sign of  $\eta$ , as illustrated in Fig. 4.8c–e.
3. Centre map, i.e. the component shows circular motion corresponding to the fifth block, as illustrated in Fig. 4.8f.

Among the above 3 maps, the unstable branch of the saddle map takes a dominant role, and the general motion around a periodic orbit of real saddle type is to escape away from it in an exponential way.

#### 4.5.4 Periodic Orbits of General Centre Type

For a periodic orbit of general centre type  $x^*$ , the monodromy matrix  $\mathbf{M}$  has 4 non-trivial multipliers, denoted as  $e^{\pm\beta_1 i}$ ,  $e^{\pm\beta_2 i}$  ( $\beta_1, \beta_2 \in \mathbb{R}^+$ ), and the Jordan canonical form includes 4 blocks:

$$1, 1, \begin{bmatrix} \cos \beta_1 & -\sin \beta_1 \\ \sin \beta_1 & \cos \beta_1 \end{bmatrix}, \begin{bmatrix} \cos \beta_2 & -\sin \beta_2 \\ \sin \beta_2 & \cos \beta_2 \end{bmatrix} \quad (4.22)$$

The two pairs of conjugate complex multipliers describe behaviours equivalent in topology. Then according to the combinations of the 4 blocks, motion around the periodic orbit can be decomposed into 2 basic maps:

1. Identity map, i.e. the component keeps invariant for every time returning to the section, corresponding to the first, second blocks;
2. Centre map, i.e. the component shows circular motion corresponding to the third (or fourth) block, as illustrated in Fig. 4.8f.

The above 2 maps show neither convergent or divergent motions, thus the general motion around a periodic orbit of general centre type maintains on a invariant torus, which is the only stable case among the 4 types.

As described in Sects. 4.5.1–4.5.4, the basic forms of maps on Poincaré section are illustrated in Fig. 4.8, including the unstable focus map (a), stable focus map (b), saddle map (c)–(e), and centre map (f).

It is worth noting that the topology of orbits extended from equilibria are correlated with the structure of local manifolds at the equilibrium points. In particular, the equilibrium points  $E_1, E_2$  are topologically equivalent, and correspondingly, orbital families 1–4 have the same topological type; the equilibrium points  $E_3, E_4$  are topologically equivalent, and correspondingly, orbital families 5, 6 have the same topological type.

## 4.6 Summary

This chapter discusses the large-scale periodic motion around a small body, starting with a search of periodic orbits around a specific asteroid. The general motion patterns near a periodic orbit are also surveyed via the analysis of its stability and topology.

Section 4.2 proposes the Hierarchical Grid Search Method to find out large-scale periodic orbits around irregular bodies, which is then applied to asteroid Kleopatra for validation. A total of 29 families of periodic orbits around Kleopatra are generated, suggesting the abundance and denseness of periodic motion about the small body.

Sections 4.3 and 4.4 survey the stability and topological types of these periodic orbits. Through an analysis on the eigen structure of the monodromy matrix, the periodic orbits of system Eq. 2.24 are classified into 7 topological types, and following consequences could be stated:

1. Among the 29 families around Kleopatra, orbits in families 13 and 14 are always stable, and there exist alteration of stability in families 7, 8, 19, and the rest 24 families are unstable;
2. 4 basic topologies are found within the 29 families, including the complex saddle type, real saddle type, central saddle type and general centre type, and the same topology usually appears in families systemic about the central body;
3. 13 families out of the 29 include topological transformations, and all the transformations occur in both directions;
4. The topological transformations are limited, which only exist between the complex saddle (a) and real saddle (b), real saddle (b) and central saddle (c), or central saddle (c) and general centre (e).

Section 4.5 discusses the general motion patterns about the periodic orbits. Then, general solutions to vicinal orbits are derived based on a linearized analysis of Poincaré map, and the orbital behaviours around periodic orbits of 4 common topologies are determined by decomposing into 5 basic forms of maps on the section: identity, unstable focus, stable focus, saddle and general centre.

As stated in Chap. 3, most part of this chapter is based on a specific asteroid Kleopatra, while special attention is paid to the qualitative properties of systems like Eq. 2.22, and the consequences will be reference for the studies on similar celestial bodies.

## References

1. Šuvakov M, Dmitrašinović V (2013) Three classes of newtonian three-body planar periodic orbits. *Phys Rev Lett* 110:114301–114304
2. Szebehely V (1967) Theory of orbits: the restricted problem of three bodies. Academic Press Inc., New York
3. Tsirigopoulos GA, Perdios EA, Markellos VV (2009) Improved grid search method: an efficient tool for global computation of periodic orbits application to hill's problem. *Celest. Mech. Dyn. Astron.* 103:49–78

4. Koon WS, Martin W, Jerrold E, Shane D (2006) Dynamical systems, the three-body problem, and space mission design. World Scientific, Berlin
5. Perko L (1991) Differential equation and dynamical system. Springer, New York
6. Shilnikov LP, Shilnikov AL, Turaev DV, Chua LO (1998) Methods of qualitative theory in nonlinear dynamics. World Scientific Publishing Co., Inc., Hackensack

# Chapter 5

## Orbital Resonance Near the Equatorial Plane of Small Bodies

**Abstract** In celestial mechanics, the orbital resonance usually indicates that the periods of two orbiting bodies are related by a ratio of two small integers, leading to a periodic mutual excitation. The result of orbital resonance could be to destabilize some orbits in Solar System, e.g. the Kirkwood gaps, and Trojan families of asteroids, which are both correlated with resonance with Jupiter. The orbital resonance here mentioned for small bodies means differently from the convention: first, it occurs between the periods of the autorotation and the heliocentric orbit, instead of between two orbits; second, this kind of resonance could make an effect within a short time, instead of accumulation over multiple periods. This chapter studies the resonant orbits near the equatorial plane of a small body, with a special attention paid to the 1:1 resonance, e.g. the occurrence and distribution. The polyhedral gravity model continues to be adopted to approximate the irregular field configuration. Section 5.2 starts with an analysis on the variation of orbital energy, showing the mechanical essence of 1:1 resonance near the small bodies. Section 5.3 surveys the parameter dependence of the resonant orbits near the equatorial plane. Section 5.4 performs a 3-dimensional Monte Carlo simulation in order to determine the parameter conditions of 1:1 resonance. Furthermore, the rest of this section discusses a special case of the resonant orbits, the ejecting orbit, and presents its proportion and distribution around the specified asteroid.

**Keywords** Resonance · Asteroid 216 Kleopatra · Chaotic motions · Planets and satellites: dynamical evolution and stability · Planets and satellites: formation · Statistical methods

### 5.1 Introduction

In celestial mechanics, the orbital resonance usually indicates that the periods of two orbiting bodies are related by a ratio of two small integers, leading to a periodic mutual excitation. The result of orbital resonance could be to destabilize some orbits in Solar System, e.g. the Kirkwood gaps, and Trojan families of asteroids, which are both correlated with resonance with Jupiter.

The orbital resonance here mentioned for small bodies means differently from the convention: first, it occurs between the periods of the autorotation and the heliocentric orbit, instead of between two orbits; second, this kind of resonance could make an effect within a short time, instead of accumulation over multiple periods.

This chapter studies the resonant orbits near the equatorial plane of a small body, with a special attention paid to the 1:1 resonance, e.g. the occurrence and distribution. The polyhedral gravity model continues to be adopted to approximate the irregular field configuration (this adds to the difficulty in applying analytical approaches, thus in this chapter, we rely more on numerical experiments to explore the resonance). Section 5.2 starts with an analysis on the variation of orbital energy, showing the mechanical essence of 1:1 resonance near the small bodies. Section 5.3 surveys the parameter dependence of the resonant orbits near the equatorial plane. Section 5.4 performs a 3-dimensional Monte Carlo simulation in order to determine the parameter conditions of 1:1 resonance. Furthermore, the rest of this section discusses a special case of the resonant orbits, the ejecting orbit, and presents its proportion and distribution around the specified asteroid.

## 5.2 1:1 Resonant Orbits Near the Small Bodies

Resonance occurs frequently in the prograde orbits near the equatorial plane close to the small body, and is defined as the orbital period and rotational period show a temporary correlation by a ratio of two small integers. The effect could be strong enough to alter the fate of the orbit rapidly (shorter than one rotational period).

Here we give a general approximated analysis. Consider the small body as a homogenous sphere of radius  $[L]$ , and check the periods of circular orbits on the equatorial plane. Assuming the ratio of orbital period to rotational period is  $d$ , the altitude of the circular orbit  $h$  satisfies

$$h = \left( \sqrt[3]{d \frac{\kappa}{3\pi}} - 1 \right) [L], \quad (5.1)$$

and assuming  $d$  to be a ratio of two small integers, e.g.  $1/3, 1/2, 2/3, 3/4, 1, 4/3, 3/2, 2, 3$ , and combining Eq. 2.31, the radius of the prograde resonant orbit ranges from 0.7 to 1.5 times of the geostationary orbit.

The 1:1 resonance near Castalia was found by Scheeres et al., that the orbital energy might show abrupt changes due to a commensuration between the asteroid rotation rate and the true anomaly rate at periapsis [1]. This section will take a detailed look at the 1:1 resonant orbits around Kleopatra, based on the polyhedral model of vicinal gravity field.

### 5.2.1 Energy Equations

Scheeres et al. introduced the Keplerian energy as the indicator of the resonant effect, which provided a good approximation under the second-degree and -order gravitational field model. In this section, we apply a full description of the gravity, and accordingly, the complete form of mechanical energy (Eq. 5.2) is adopted as the resonant indicator.

$$W = U + K, \quad (5.2)$$

in which  $U$  is the potential of the small body,  $K$  is the kinetic energy with respect to the inertia frame  $OXYZ$ . Equation 5.2 could be written as

$$W = U + \frac{1}{2} |\boldsymbol{\omega} \times \mathbf{r} + \dot{\mathbf{r}}|^2. \quad (5.3)$$

The orbital energy  $W$  is not conserved because the gravitational field is non-central. In physics, it means there exists an energy transportation between the small body and the test point surrounding it (this influence is negligibly small to the rotation of the small body, which is omitted in Eq. 2.20). Recall the definition of the efficient potential Eqs. 2.21, 5.3 is restated as

$$W = C + \boldsymbol{\omega} \cdot \mathbf{L}, \quad (5.4)$$

where  $\mathbf{L} = \mathbf{r} \times (\boldsymbol{\omega} \times \mathbf{r} + \dot{\mathbf{r}})$  indicates the angular momentum under  $OXYZ$ . Considering the small body is doing work to the orbit of the mass point,

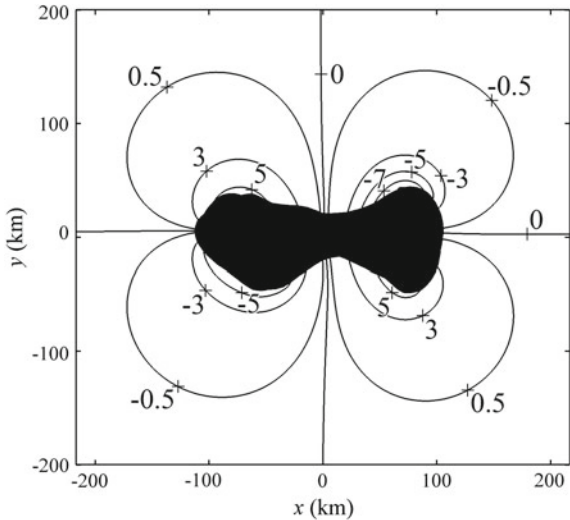
$$p = \frac{d}{dt} W, \quad (5.5)$$

Equation 5.5 defines the instantaneous power. Then substituting Eqs. 5.4 and 5.5, it yields

$$p = -(\boldsymbol{\omega} \times \mathbf{r}) \cdot \nabla U. \quad (5.6)$$

Equation 5.6 shows the rate of orbital energy  $p$  only depends on the relative position to the small body  $\mathbf{r}$ , i.e. it determines a body-fixed scalar field in  $Cxyz$ . Figure 5.1 illustrates the counter lines of the power field on the equatorial plane ( $z = 0$ ). The distribution of  $p$  is approximately symmetric in four quadrants: I.  $x > 0$ ,  $y > 0$ ; II.  $x < 0$ ,  $y > 0$ ; III.  $x < 0$ ,  $y < 0$ ; IV.  $x > 0$ ,  $y < 0$ . In general, the power is positive in quadrants II and IV and negative in quadrants I and III, and its magnitude declines rapidly as distance away from the small body. The border lines  $p = 0$  are close to  $x$ -,  $y$ -axes, and in every quadrant, the magnitude of  $p$  peaks near the doming edges of Kleopatra, which is correlated with its special geography.

**Fig. 5.1** The counter lines of gravitational power  $p$  on the equatorial plane of Kleopatra, unit:  $10^{-7} \text{ km}^2/\text{s}^3$



As shown in Fig. 5.1, the mechanical energy of orbits near the equatorial plane decreases in quadrants I and III and increases in quadrants II and IV. Obviously,

1. All the equilibrium points lie on the border lines  $p = 0$ ;
2. A periodic orbit spans over at least two connected quadrants, e.g. families 1 and 2 (see Sect. 4.2.2), otherwise the orbital energy would show monotonous variation;
3. The orbital energy keeps steady in the area far away from the small body, which appears a quasi Keplerian motion in the inertia frame  $OXYZ$ , and in the area close to the surface of the small body, the orbital energy shows relatively fast changes.

### 5.2.2 A Mechanism of 1:1 Resonance

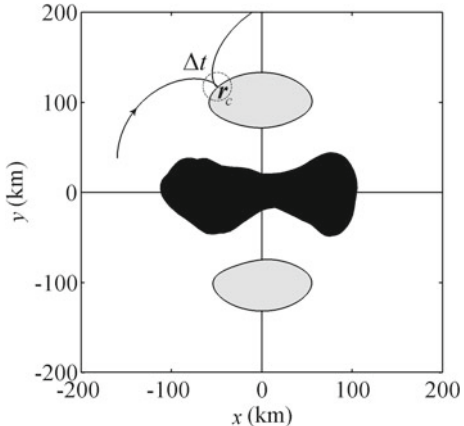
The 1:1 resonance near a small body, is a temporary synchronization caused by close angular speeds of the autorotation and the orbit, subject to

$$\dot{r} \approx 0, \quad (5.7)$$

According to the analysis of accessible region (see Sect. 3.2.2), the instantaneous position  $\mathbf{r}_c$  is close to the zero-velocity surface specified by Jacobi integral. Define  $\Delta t$  the duration of orbit staying around  $\mathbf{r}_c$ , which is relatively long due to the small velocity, and corresponding variation of the orbital energy is

$$\Delta W \approx p(\mathbf{r}_c) \Delta t, \quad (5.8)$$

**Fig. 5.2** An example segment of 1:1 resonant orbit on the equatorial plane of Kleopatra ( $C = -2.09 \times 10^{-3} \text{ km}^2/\text{s}^2$ ). The grey shadow indicates the forbidden area



where  $p(\mathbf{r}_c)$  indicates the energy rate at  $\mathbf{r}_c$ , and as stated in Sect. 5.2.1,  $p \neq 0$  at the area far away from the border lines, thus Eq. 5.8 determines the increment of the orbital energy within the segment about  $\mathbf{r}_c$ . Figure 5.2 illustrates an example of the 1:1 resonant orbit on the equatorial plane of Kleopatra, which approaches the zero-velocity surface at a position  $\mathbf{r}_c$  at quadrant II, corresponding to a positive energy rate  $p(\mathbf{r}_c) > 0$ . Accordingly, the orbital energy experiences a sharp increase  $\Delta W$ , seeming like a swing-by over one side of Kleopatra in the inertia frame  $OXYZ$ .

Further estimate the magnitude of  $\Delta W$ . Equation 5.4 is written as

$$W = C + |\boldsymbol{\omega} \times \mathbf{r}|^2 + (\boldsymbol{\omega} \times \mathbf{r}) \cdot \dot{\mathbf{r}}. \quad (5.9)$$

As shown in Fig. 5.2, the incoming and outgoing velocities to the vicinity of  $\mathbf{r}_c$  are denoted as  $\dot{\mathbf{r}}^-$  and  $\dot{\mathbf{r}}^+$ , respectively. According to Eq. 3.4,

$$|\dot{\mathbf{r}}^-| \approx |\dot{\mathbf{r}}^+|, \quad (5.10)$$

i.e. the magnitudes of these velocities are close, while the directions differ a lot. Defining  $\Delta\dot{\mathbf{r}} = \dot{\mathbf{r}}^+ - \dot{\mathbf{r}}^-$ , and considering the orbital position changes little, we obtain

$$\Delta W \approx (\boldsymbol{\omega} \times \mathbf{r}_c) \cdot \dot{\mathbf{r}}. \quad (5.11)$$

Equation 5.11 estimates the increment of the orbital energy before and after the resonance, and it also shows the essence of 1:1 resonance: the abrupt variation of orbital energy is caused by the noncentral gravitational field doing work along the convected velocity of the orbit during the synchronization.

### 5.2.3 Typical Resonant Orbits

As stated in Sect. 5.2.1, the resonant cases near the equatorial plane are symmetric for the increase and decrease of orbital energy, thus in this chapter we only discuss the increasing case ( $\Delta W > 0$ ) as representative. The orbital energy is applied to discriminate the fate of an orbit:  $W > 0$  if the orbit is escaping away from the central body,  $W < 0$  if the orbit is orbiting around it, and  $W = 0$  is treated as the critical case.

It is worth noting that the orbital energy in system Eq. 2.20 is not constant, thus the classification stated above is not absolute, instead, we can delineate some morphological types of the 1:1 resonant orbits according to the change of  $W$ :

1. The orbit remains cycling around the small body, but with a larger eccentricity;
2. The orbit turns from cycling around the small body to escaping away;
3. The orbit comes in as a hyperbola, and gains a greater speed to escape away after the resonance.

Figure 5.3 shows the example orbits about Kleopatra for above 3 types in  $OXYZ$  ( $\Delta W > 0$ ), respectively. Taking Fig. 5.3a as an example (type I), the dashed line indicates the whole segment of orbit spanning a time range as shown in the energy curve (right), the solid lines indicate the resonant segment over  $[t_A, t_B]$ , which is determined from the sharp increase of the orbital energy. The orbital shapes and corresponding energy variations of type II and III are illustrated in the same way.

Figure 5.3 reveals some feature of 1:1 resonance:

1. The resonance occurs near the perigee of the orbit in  $OXYZ$ ;
2. The resonance usually lasts only a short time (<1 period of autorotation), but results in an abrupt change of the orbital energy;
3. The resonance is only observed among prograde orbits near the equatorial plane, which is consistent with our analysis in Sect. 5.2.2, that retrograde orbits have positive Jacobi integral  $C$  in which case the forbidden region vanishes near the equatorial plane.

As shown in Fig. 5.3a, b, the type I and type II provide a mechanism to clean the equatorial area near Kleopatra, which should be correlated with the formation conditions of natural satellites.

## 5.3 Parameter Dependence of the Resonance

To further analyze the dependence of orbital energy  $W$  on Jacobi integral  $C$ , denote the convected velocity  $\mathbf{v}_t = \boldsymbol{\omega} \times \mathbf{r}$ , and combine Eqs. 3.4 and 5.9, we have

$$W = C + |\mathbf{v}_t|^2 + \cos\gamma |\mathbf{v}_t| \sqrt{2(C - V)}, \quad (5.12)$$

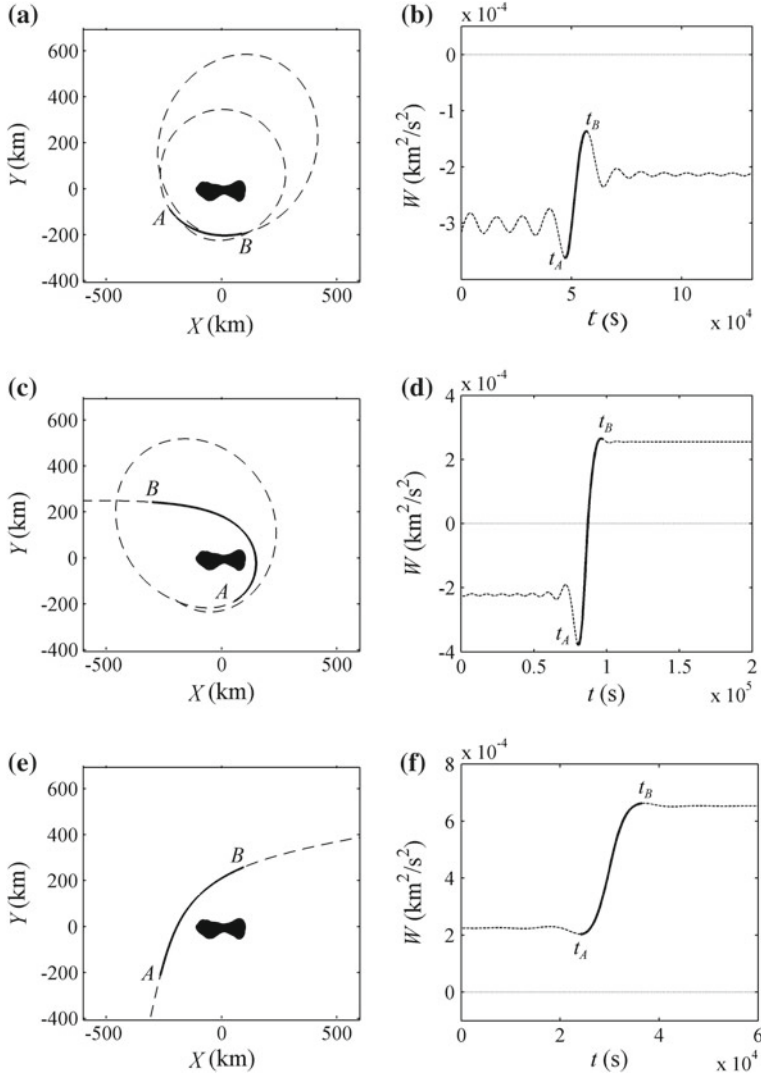


**Fig. 5.3** The example orbits near the equatorial plane of Kleopatra for the 3:1:1 resonant types ( $\Delta W > 0$ ), together with the time variations of the orbital energy. **a** Type I: orbital morphology. **b** Type I: orbital energy. **c** Type II: orbital morphology. **d** Type II: orbital energy. **e** Type III: orbital morphology. **f** Type III: orbital energy

in which the third term on the right hand side indicates the inner product of the convected velocity and relative velocity,  $0 \leq \gamma \leq \pi$  indicates their separation angle. And considering the convected velocity  $v_t$  only depends on the position, thus given the value of  $C$ , Eq. 5.12 presents the range of orbital energy at any field point:

$$\begin{aligned} W_{\max} &= C + |\mathbf{v}_t|^2 + |\mathbf{v}_t| \sqrt{2(C - V)}, \\ W_{\min} &= C + |\mathbf{v}_t|^2 - |\mathbf{v}_t| \sqrt{2(C - V)}. \end{aligned} \quad (5.13)$$

The width of this range is  $2|\mathbf{v}_t| \sqrt{2(C - V)}$ , whose size relies on the distance away from the zero-velocity surface. The farther away, the wider the range would be, and, the width is 0 on the zero-velocity surface, i.e.  $W = W_{\max} = W_{\min}$  is a constant value. This is the typical 1:1 resonance, and at the resonant position  $\mathbf{r}_c$ , the orbital energy is

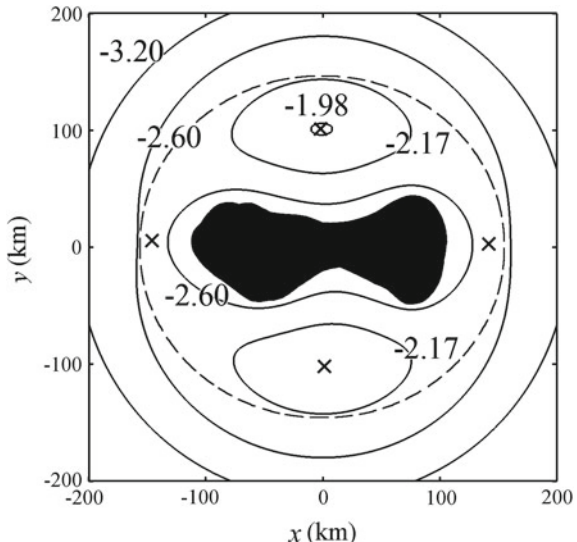
$$W_c \approx C + |\mathbf{v}_t|^2. \quad (5.14)$$

Recall the analysis on the increasing cases ( $\Delta W > 0$ ):  $W_c > 0$  corresponds to the escaping orbit (type II or type III);  $W_c < 0$  corresponds to the escaping orbit (type I). Figure 5.4 outlines the regions of  $W_c > 0$  and  $W_c < 0$  at different Jacobi integral  $C$ , that as the dashed line discriminated, outside this region, the points on zero-velocity surfaces have positive  $W_c$ , and inside it,  $W_c$  is negative.

Figure 5.4 shows the contour lines of Jacobi integral at 4 given values, and according to the intersection between these contours and the boundary, we have (considering the case of  $W_c > 0$ ):

1. When  $C > -2.17 \times 10^{-3} \text{ km}^2/\text{s}^2$ , all positions on the zero-velocity surface have positive  $W_c$ , in which case all 1:1 resonant orbits belongs to type I;
2. When  $C < -2.60 \times 10^{-3} \text{ km}^2/\text{s}^2$ , all positions on the zero-velocity surface have negative  $W_c$ , in which case all 1:1 resonant orbits belongs to type II or type III;

**Fig. 5.4** The regions of  $W_c > 0$  and  $W_c < 0$  on the equatorial plane of Kleopatra, unit:  $10^{-3} \text{ km}^2/\text{s}^2$ . The crosses show the positions of the equilibrium points  $E_1-E_4$ , and the dashed line indicates the boundary  $W_c = 0$



3. When  $-2.60 \times 10^{-3} \text{ km}^2/\text{s}^2 \leq C \leq -2.17 \times 10^{-3} \text{ km}^2/\text{s}^2$ , the zero-velocity surface intersects with the dashed line, in which case or three types of 1:1 resonant orbits exist;
4. All the 4 equilibrium points of Kleopatra fall inside the region  $W_c < 0$ , thus the orbits on unstable manifolds at the equilibria will be trapped within the vicinity of Kleopatra within a short term.

It is notable that above analyses are valid only if the zero-velocity surface intersects with the equatorial plane, i.e.  $C < -1.99 \times 10^{-3} \text{ km}^2/\text{s}^2$ , otherwise the low-latitude orbits will never approach the zero-velocity surface, and accordingly no 1:1 resonance will be observed. Besides, the outcome of resonant orbit when  $-2.60 \times 10^{-3} \text{ km}^2/\text{s}^2 \leq C \leq -2.17 \times 10^{-3} \text{ km}^2/\text{s}^2$  (whether escape or not) highly depends on the phase angle of the resonant position, which suggests the resonant orbit is sensitive to the initial condition.

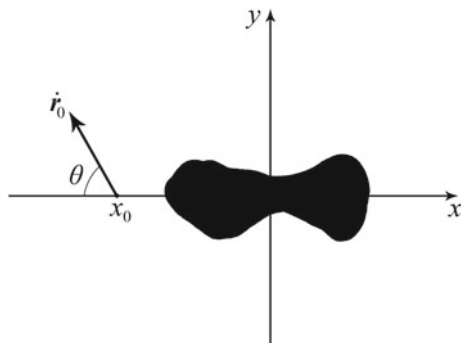
## 5.4 Resonant Orbits Near the Equatorial Plane of 216 Kleopatra

According to the analyses in Sect. 5.3, the distribution of 1:1 resonant orbits near the equatorial plane relies on Jacobi integral  $C$ , and for a given value of  $C$ , whether there exists 1:1 resonance and its strength relies on the initial condition. This section tends to perform a traversing search over all the orbits of low latitude in numeric, in order to get the global distribution of resonant orbits about Kleopatra.

Considering the quasi planar motion near the equatorial plane, the dimension of initial state  $(\mathbf{r}_0, \dot{\mathbf{r}}_0)$  could be reduced to 4. And then combining the symmetric analysis in Sect. 5.2.1, only the trajectories of  $\Delta W > 0$  in quadrant II should be calculated here. Assigning the initial position  $\mathbf{r}_0$  along  $-x$  axis, i.e.  $\mathbf{r}_0 = (x_0, 0, 0)$ ,  $\dot{\mathbf{r}}_0$  pointing to quadrant II, and  $\theta$  measures the incident angle down from  $-x$  axis ( $0 \leq \theta \leq \pi$ ), the magnitude of  $\dot{\mathbf{r}}_0$  is determined by Eq. 3.4 with specified Jacobi integral  $C$ .

Figure 5.5 illustrates the initial states of an incident trajectory into quadrant II, determined by  $x_0$  and  $\theta$ . Then integrating Eq. 2.20 until the trajectory escapes from

**Fig. 5.5** The initialization of incident trajectories in quadrant II around Kleopatra



quadrant II, we get the full segment inside quadrant II, corresponding to  $(x_0, \theta)$ . Grid searching is performed over the 2-dimensional parameter space of  $(x_0, \theta)$ , and for different governing parameter  $C$ , which makes a traversing algorithm in numeric.

### 5.4.1 Parameter Conditions for Orbital Resonance

As stated in Sect. 5.2.2, 1:1 resonance corresponds to a sharp increase of orbital energy. The grid search presents the distribution of the energy increment over  $(x_0, \theta)$  plane  $\Delta W$ , which indicates the 1:1 resonance of different strength.

Assuming  $-2.55 \times 10^{-3} \text{ km}^2/\text{s}^2 \leq C \leq -0.49 \times 10^{-3} \text{ km}^2/\text{s}^2$ ,  $-7.19 \times 10^2 \text{ km} \leq x_0 \leq -1.25 \times 10^2 \text{ km}$ ,  $0 \leq \theta \leq \pi$ , Fig. 5.6 illustrates the distribution of orbital energy increment of trajectories located in quadrant II for 6 different Jacobi constants, each of which is derived from a  $200 \times 200$  grid search.

Figure 5.6 reveals several interesting points about the resonance, summarized as follows:

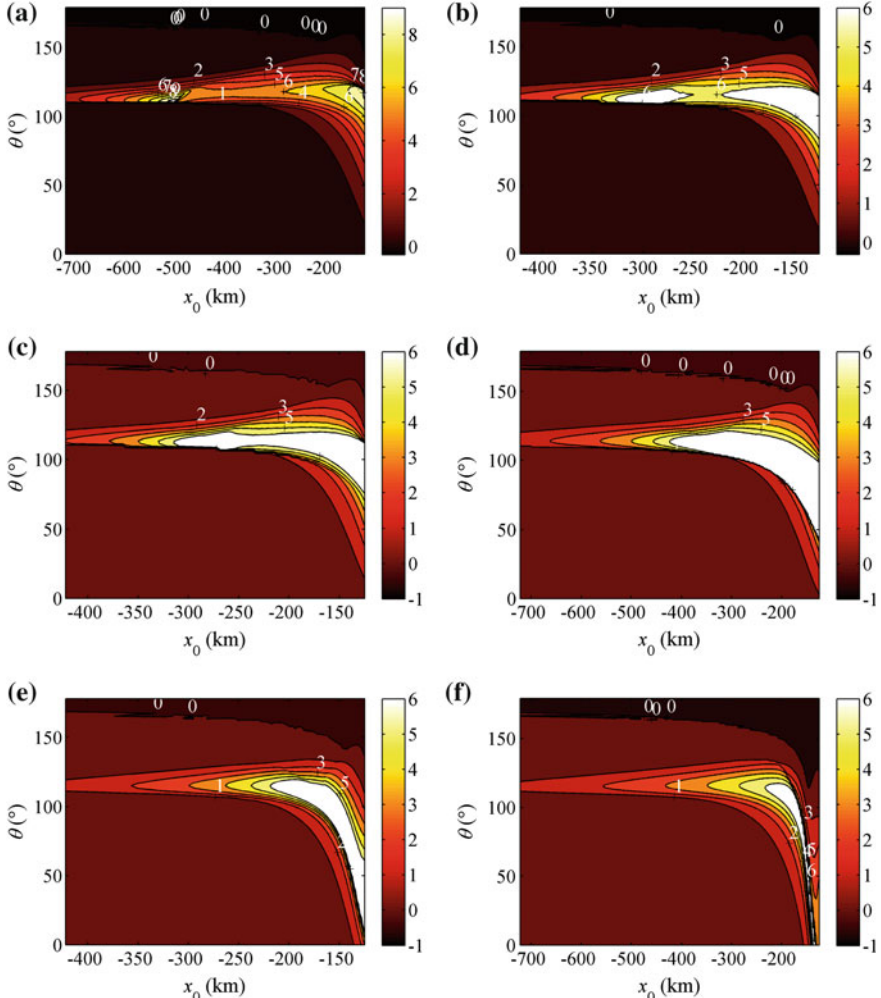
1. When  $x_0 < -200 \text{ km}$ ,  $\Delta W$  peaks around  $\theta = 125^\circ$ , and declines as  $|x_0|$  increasing, i.e. 1:1 resonance occurs near a constant incident angle;
2. When  $x_0 > -200 \text{ km}$ , large values of  $\Delta W$  expands over a wide range of the incident angle  $20^\circ < \theta < 125^\circ$ , showing extreme instability of the prograde orbits near the equatorial plane of Kleopatra;
3. The big values of  $\Delta W$  concentrate within a narrow region of the  $(x_0, \theta)$  plane, and outside this region,  $\Delta W$  declines rapidly;
4. When  $C > -1.09 \times 10^{-3} \text{ km}^2/\text{s}^2$ , a secondary resonant region is separated from the primary, which is mainly constitute of the hyperbolic resonant orbits of type III.

Apparently, the 1:1 resonance is sensitive to all the parameters  $C$ ,  $x_0$  and  $\theta$ . Table 5.1 presents the initial states  $(x_0, \theta)$  corresponding to the peak values of  $\Delta W$  at the 6 Jacobi constants, showing the extreme values  $\Delta W_{\max}$  always appear close to the surface of Kleopatra. And Fig. 5.7 illustrates the curve of  $\Delta W_{\max}$  varying as Jacobi integral.

As show in Fig. 5.7,  $\Delta W_{\max}$  declines rapidly when  $C > -1.99 \times 10^{-3} \text{ km}^2/\text{s}^2$ , which is consistent with the analysis of Sect. 5.3: in this case, the zero-velocity surface does not intersect with the equatorial plane, and thus there exists no typical 1:1 resonant orbits around Kleopatra.

### 5.4.2 Distribution of the Ejecting Orbits

In the long term, there are three outcomes for an orbit starting from the neighbourhood of a small body: I. stable motion around the small body; II. escape from the

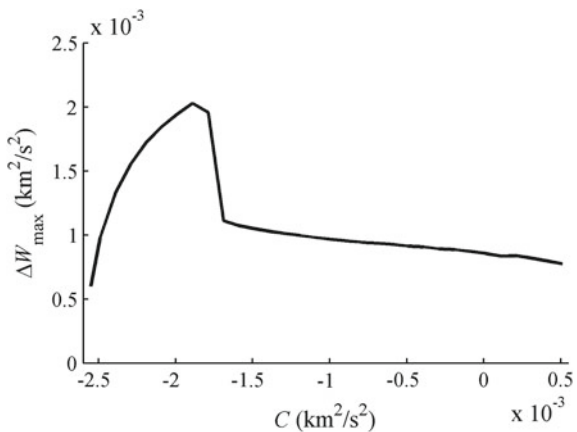


**Fig. 5.6** The distribution of orbital energy increment of the trajectories located in quadrant II about Kleopatra. The colour map shows the magnitude of  $\Delta W$ , and the numbers labelled over the frames indicate the values of contour lines, unit:  $\text{km}^2/\text{s}^2$ . **a**  $C = -0.49 \times 10^{-3} \text{ km}^2/\text{s}^2$ . **b**  $C = -0.89 \times 10^{-3} \text{ km}^2/\text{s}^2$ . **c**  $C = -1.09 \times 10^{-3} \text{ km}^2/\text{s}^2$ . **d**  $C = -1.69 \times 10^{-3} \text{ km}^2/\text{s}^2$ . **e**  $C = -2.29 \times 10^{-3} \text{ km}^2/\text{s}^2$ . **f**  $C = -2.51 \times 10^{-3} \text{ km}^2/\text{s}^2$

gravitational field of the small body; III. reimpact on the surface of the small body. This section focuses on the natural ejecting orbit, which is initialized as cycling around the small body, and eventually escape from it because of 1:1 resonance (see Fig. 5.3c). The ejecting orbits show a strong effect of 1:1 resonance at cleaning the neighbourhood of a small body, and their universality is correlated with our understanding of the vicinal spatial environment.

**Table 5.1** The initial states ( $x_0$ ,  $\theta$ ) corresponding to the peak values of  $\Delta W$ 

$C$ ( $10^{-3}$ km $^2$ /s $^2$ )	$x_0$ (km)	$\theta$ ( $^\circ$ )
-0.49	-127	112.3
-0.89	-128	108.6
-1.09	-127	96.1
-1.69	-129	67.6
-2.29	-131	30.7
-2.51	-134	20.4

**Fig. 5.7** The curve of  $\Delta W_{\max}$  varying as Jacobi integral  $C$ 

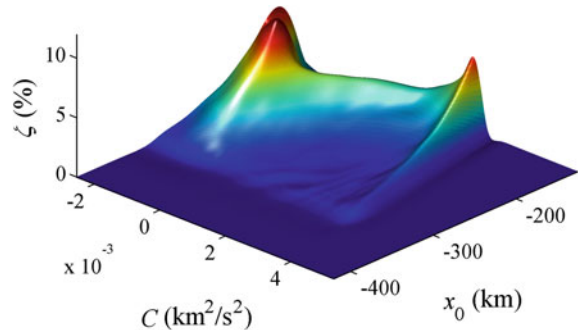
Grid search is performed over the orbital segments in quadrant II to examine the distribution of natural ejecting orbits. Assigning Jacobi integral  $-2.55 \times 10^{-3}$  km $^2$ /s $^2 \leq C \leq 5.31 \times 10^{-3}$  km $^2$ /s $^2$ , initial position  $-7.19 \times 10^2$  km  $\leq x_0 \leq -1.25 \times 10^2$  km and the incident angle  $0 \leq \theta \leq \pi$ , an ejecting orbit is defined as:  $W < 0$  when entering quadrant II, and  $W > 0$  when exiting from quadrant II. The parameter space ( $C, x_0$ ) is then divided into  $500 \times 500$  mesh, and at each node, the orbit is integrated with incident angle  $\theta = 1^\circ, \theta = 2^\circ, \dots, \theta = 180^\circ$ . The proportion of ejecting orbit at a given node is

$$\psi = \frac{N_{eject}}{180}, \quad (5.15)$$

in which  $N_{eject}$  defines the number of ejecting orbits out of the 180 samples. Figure 5.8 illustrates the distribution of ejecting orbits about Kleopatra over the parameter space ( $C, x_0$ ).

As illustrated in Fig. 5.8, the proportion of ejecting orbits near the equatorial plane of Kleopatra shows continuous distribution and reaches up to 7 %. Several interesting points could be stated:

**Fig. 5.8** The proportion of ejecting orbits  $\psi$  correlated with Jacobi integral  $C$  and initial position  $x_0$



1. Natural ejecting orbits are distributed over the region  $C < 3.41 \times 10^{-3} \text{ km}^2/\text{s}^2$ ,  $x_0 > -3.51 \times 10^2 \text{ km}$ , and the proportion peaks at  $C = -2.07 \times 10^{-3} \text{ km}^2/\text{s}^2$ ,  $x_0 = -2.06 \times 10^2 \text{ km}$ ;
2. High proportion of ejecting orbits is observed in a banded region  $-2.55 \times 10^{-3} \text{ km}^2/\text{s}^2 \leq C \leq -1.99 \times 10^{-3} \text{ km}^2/\text{s}^2$ , which is consistent with the consequences of Sect. 5.3;
3. There appears a high probability of ejecting orbits in  $-2.40 \times 10^2 \text{ km} \leq x_0 \leq -1.35 \times 10^2 \text{ km}$ , which turns to be the high-risk band for spacecraft;
4. All equatorial orbits are retrograde when  $C > 3.41 \times 10^{-3} \text{ km}^2/\text{s}^2$ , in which case there is no 1:1 resonance and thus the proportion of ejecting orbits turns to be 0;
5. The proportion of ejecting orbits drops to 0 when  $x_0 > 3.51 \times 10^2 \text{ km}$ , i.e. beyond the vicinal banded region, the resonance becomes very weak and the orbits of low latitudes show more stability. As a support from observations, both natural satellites of Kleopatra lie in this region.

## 5.5 Summary

This chapter surveys the 1:1 resonant orbits near the equatorial plane of a small body based on the polyhedral model of gravitational field. The energy analysis reveals that the essence of 1:1 resonance is the abrupt change of orbital energy caused by the non-central gravitational field doing work along the convected velocity; a classification of 1:1 resonant orbits is proposed according to the orbital energy before and after the resonance, and example orbits for 3 typical cases about Kleopatra are presented, respectively. The second part of this chapter discusses the parameter dependence of the 1:1 resonance on Jacobi integral  $C$ . Taking Kleopatra as an example, we present the range of  $C$  when 1:1 resonance occurs, and show it is correlated with the shape of zero-velocity surface on the equatorial plane, and that the resonant effect is sensitive to the synchronous phase of the orbit.

Special attention is paid to the resonant orbits near the equatorial plane of Kleopatra. The parameter condition and global distribution of 1:1 resonant orbits are examined based on numerous simulations, and the results are summarized as follows:

1. 1:1 resonance is the main cause of natural ejecting orbit, which shows consistent distribution with the orbital energy increment;
2. A banded region of high proportion of ejecting orbits is observed close to the surface of Kleopatra, which could be dynamically dangerous for spacecrafts;
3. 1:1 resonance does not exist among the retrograde orbits near the equatorial plane, which is more stable than the prograde ones;
4. Beyond the specified region of parameters, the proportion of ejecting orbits drops to 0 and the resonance becomes weak, which agrees with the observation on the region near Kleopatra where exists natural satellites.

## Reference

1. Scheeres DJ, Ostro SJ, Hudson RS et al (1996) Orbits close to asteroid 4769 Castalia. *Icarus* 121:67–87

# Chapter 6

## Natural Motion Near the Surface of Small Bodies

**Abstract** Observations have shown that most small bodies of diameters larger than 300 m are covered by regolith materials, i.e. an active layer of loose unconsolidated rocks and dust, which has been shaped by various space weathering effects. Thus, a detailed look at the grains' dynamics is apparently important and necessary for the understanding of above processes. The ejecta from a meteorite impact may experience different evolutional histories and end up with different fates. Differing from around planets, the orbital motion and surface motion around a small body are not clearly demarcated, because: first, the gravity from a small body is usually weak, and the minimum launch speed could be easily reached each by a natural grain on the surface; second, small bodies have no atmosphere, i.e., once an object lifts from the surface, it is counted as orbital motion. This chapter presents our method to model the migration of individual grain on asteroid's surface. In Sect. 6.2, a global valid method for gravitational field calculation is developed; Sect. 6.3 proposes an event-driven model to implement full simulation of an individual particle moving over the surface of an asteroid; Sect. 6.4 includes basic tests as verification to the model proposed; Sect. 6.5 demonstrates a possible application of our method, to explore the surface mechanical environment of a specified asteroid 1620 Geographos, and to find out the connections between the local geological features and the dynamical behaviours of the test particle.

**Keywords** Planetary geology · Asteroid 1620 Geographos · Computer methods · Chaotic motions · Regolith formation · Planets and satellites · Dynamical evolution and stability

### 6.1 Introduction

Observations have shown that most small bodies of diameters larger than 300 m are covered by regolith materials, i.e., an active layer of loose unconsolidated rocks and dust, which has been shaped by various space weathering effects like meteorite impacts, solar wind sputtering, planetary tides, etc. Reference [1] a detailed look at the grains' dynamics is apparently important and necessary for the understanding

of above processes. The ejecta from a meteorite impact may experience different evolutional histories and end up with different fates, e.g., part of the ejecta may escape directly, part may enter a stable cycling orbit around the small body, and the rest may fall back onto the surface and have interactions like hopping, sliding, twisting, rolling, etc.

Differing from that on planets, the orbital motion and surface motion around a small body are not clearly demarcated, because: first, the gravity from a small body is usually weak, and the minimum launch speed could be easily reached each by a natural grain on the surface, e.g. the lower limit of launching speed on Eros is  $\sim 5$  m/s (see Sect. 6.4 for the definition of launching speed); second, small bodies have no atmosphere (some asteroids have jets like coma, which cannot really constitute the atmosphere), and once an object lifts from the surface, it is counted as orbital motion.

This chapter presents our method to model the migration of individual grain on asteroid's surface, which is a mixed routine of orbiting over the surface and interactions with the surface. In Sect. 6.2, a global valid method for gravitational field calculation is developed, which fixed the possible singularities based on the conventional polyhedron method proposed by Werner et al. [2]; Sect. 6.3 proposes an event-driven model to implement full simulation of an individual particle moving over the surface of an asteroid; Sect. 6.4 includes basic tests as verification to the model proposed; Sect. 6.5 demonstrates a possible application of our method, to explore the surface mechanical environment of a specified asteroid 1620 Geographos, and to find out the connections between the local geological features and the dynamical behaviours of the test particle.

## 6.2 Modelling Mechanics of the Surface

Considering the motion of an object (viewed as a mass point) on/above the surface of a small body (modelled as a homogenous polyhedron), at least two aspects of work must be done: first, a global valid method is required to calculate the potential and gravity on the surface, since Eqs. 2.14 and 2.15 fail at some points of the facets; and second, the polyhedral surface must be smoothed to ensure that the particle's velocity is continuous when crossing the common edge of two facets, otherwise there would be a sharp change in the local tangent plane.

### 6.2.1 Modified Polyhedral Method

Two classes of singularities might be caused by following the polyhedral method proposed in Sect. 2.3.3: the first is the application of Gauss's divergence theorem with the conditions violated, which occurs when the field point locates inside the polyhedron or on its surface, making the integrated field function discontinuous at

this point [3]; the second is the numerical exceptions from Eqs. 2.14 and 2.15, resulted by the infinite integrals in Eqs. 6.1 and 6.2 when there are zero denominators in the integral area.

$$L_e = \int_e \frac{1}{r} ds, \quad (6.1)$$

$$\theta_f = \int_f \frac{\hat{\mathbf{n}}_f \cdot \mathbf{r}_f}{r^3} dS, \quad (6.2)$$

in which the variants are defined in Sect. 2.3.3. When the field point falls on edge  $e$  or facet  $f$ , these terms are improper integrals and singularity appears. The second class can be corrected easily by examining the exceptions. When the field point  $\mathbf{r}$  lies outside edge  $e$ , the line integral Eq. 6.3 yields

$$L_e = L_e^* = \ln \frac{r_1 + r_2 + d_e}{r_1 + r_2 - d_e}, \quad (6.3)$$

where  $r_1, r_2$  indicate the distances from  $\mathbf{r}$  to the two edges of edge  $e$ , and  $d_e$  indicates the length of  $e$ . If  $\mathbf{r}$  falls on edge  $e$ , Eq. 6.3 fails, and a well-known solution is to exclude a small neighbourhood  $\delta_e$  around the singular point, and to calculate the normal integration over the remained area  $e^\circ$ , then approaching the limit as  $\delta_e \rightarrow 0$ , Eq. 6.1 becomes

$$L_e = \lim_{\delta_e \rightarrow 0} \int_{e^\circ} \frac{1}{r} ds. \quad (6.4)$$

Combining the corresponding terms in Eqs. 2.14 and 2.15, when  $\mathbf{r}$  lies on edge  $e$ , it yields

$$L_e \mathbf{E}_e \cdot \mathbf{r}_e = \lim_{\delta_e \rightarrow 0} \mathbf{E}_e \cdot \mathbf{r}_e \int_{e^\circ} \frac{1}{r} ds = \lim_{\delta_e \rightarrow 0} \mathbf{0} \int_{e^\circ} \frac{1}{r} ds = \mathbf{0}. \quad (6.5)$$

Likewise, Eq. 6.6 fails if  $\mathbf{r}$  falls on the facet polygon. Then exclude a small neighbourhood  $\delta_f$  around the singular point, and calculate the normal integration over the remained area  $f^\circ$ . The integral value could be achieved by approaching the limit as  $\delta_f \rightarrow 0$ , as shown by Eq. 6.7.

$$\theta_f = \theta_f^* = 2 \arctan \frac{\mathbf{r}_1 \cdot (\mathbf{r}_2 \times \mathbf{r}_3)}{r_1 r_2 r_3 + r_3 \mathbf{r}_1 \cdot \mathbf{r}_2 + r_1 \mathbf{r}_2 \cdot \mathbf{r}_3 + r_2 \mathbf{r}_3 \cdot \mathbf{r}_1}, \quad (6.6)$$

$$\theta_f = \lim_{\delta_f \rightarrow 0} \int_{f^\circ} \frac{\hat{\mathbf{n}}_f \cdot \mathbf{r}_f}{r^3} dS. \quad (6.7)$$

And the corresponding terms in Eqs. 2.14 and 2.15, when  $\mathbf{r}$  lies inside the polygon facet  $f$ , become

$$\theta_f \mathbf{F}_f \cdot \mathbf{r}_f = \lim_{\delta_f \rightarrow 0} \mathbf{F}_f \cdot \mathbf{r}_f \int_{f^\circ} \frac{\hat{\mathbf{n}}_f \cdot \mathbf{r}_f}{r^3} dS = \lim_{\delta_f \rightarrow 0} \mathbf{0} \int_{f^\circ} \frac{\hat{\mathbf{n}}_f \cdot \mathbf{r}_f}{r^3} dS = \mathbf{0}. \quad (6.8)$$

By using the arctangent function with two arguments atan2, the singular zone could be further reduced to the three borders of polygon  $f$ , denoted by  $\bar{f}$ . Define piecewise functions

$$P_e(\mathbf{r}) = \begin{cases} \mathbf{0} & \mathbf{r} \in e \\ L_e^* \mathbf{E}_e \cdot \mathbf{r}_e & \mathbf{r} \notin e \end{cases}, \quad (6.9)$$

$$Q_f(\mathbf{r}) = \begin{cases} \mathbf{0} & \mathbf{r} \in \bar{f} \\ \theta_f^* \mathbf{F}_f \cdot \mathbf{r}_f & \mathbf{r} \notin \bar{f} \end{cases}, \quad (6.10)$$

the modified expressions of the gravitational potential and attraction are represented by Eqs. 6.11 and 6.12,

$$U = \frac{1}{2} G \sigma \left( \sum_{e \in ES} \mathbf{r}_e \cdot P_e(\mathbf{r}) - \sum_{f \in FS} \mathbf{r}_f \cdot Q_f(\mathbf{r}) \right), \quad (6.11)$$

$$\nabla U = -G \sigma \left( \sum_{e \in ES} P_e(\mathbf{r}) - \sum_{f \in FS} Q_f(\mathbf{r}) \right), \quad (6.12)$$

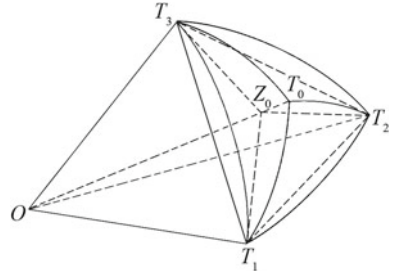
which removed the possible numerical exceptions of the second class. Notably, a tolerance domain should be defined when applying Eqs. 6.11 and 6.12 in numeric, that once  $\mathbf{r}$  enters the domain, it should be taken as the singular case.

On the other hand, the singularity of the first class is more essential and influential than the second class. Tossups et al. proposed a solution to apply Gauss's divergence theorem based on the formulas of pure line integrals [4]. However, the theorem violation in Eqs. 2.14–2.16 when  $\mathbf{r}$  lies inside or on the polyhedron seems benign, and Werner et al. pointed out these formulas are still correct in the interior [2]. Thus, we actually derived a global valid method to calculate the gravity and potential at any point inside, outside or on the surface of the polyhedron, by increasing only a small quantity of computation.

### 6.2.2 $C^1$ Surface Interpolation over the Polyhedron

An essential barrier of this study is the inconsistent states on two connected facets, which happens when a particle moving on the surface across the common edge, and the solution proposed here is to cover the polyhedron with patches of curved surfaces, which retain the profile of the asteroidal shape but portray more detailed geology of

**Fig. 6.1** The Bézier patches generated over the facet of a polyhedron



its surface. Shirman et al. developed an algorithm to generate quartic Bézier patches over a triangular facet [5], as illustrated in Fig. 6.1.

As shown in Fig. 6.1, an arbitrary facet  $\triangle T_1 T_2 T_3$  of the polyhedron is first divided into three small triangular ones  $\triangle T_1 T_2 Z_0$ ,  $\triangle T_2 T_3 Z_0$  and  $\triangle T_3 T_1 Z_0$ . Then 31 control points are calculated and used to determine the coplanar cubic curves  $\widehat{T_1 T_2}$ ,  $\widehat{T_2 T_3}$ ,  $\widehat{T_3 T_1}$ ,  $\widehat{T_1 Z_0}$ ,  $\widehat{T_2 Z_0}$  and  $\widehat{T_3 Z_0}$ . As the last step, these curved wireframes are filled with Bézier patches (the derivations and expressions of interpolated surfaces have been omitted). Thus, for a polyhedron consist of  $N_f$  triangular facets, total  $3N_f$  Bézier patches will be created, each assigned with a unique *ID*.

$$ID = (f, i), \quad (6.13)$$

which is composed of facet number  $f = 1, 2, \dots, N_f$  and patch number  $i = 1, 2, 3$ . And represent the equation of Bézier patch *ID* as

$$\mathbf{r} = B(u, v; \mathbf{c}_{ID}^1, \mathbf{c}_{ID}^2, \dots, \mathbf{c}_{ID}^{15}), \quad (6.14)$$

where  $\mathbf{c}_{ID}^j$  ( $j = 1, 2, \dots, 15$ ) are vector parameter,  $0 \leq u \leq 1$ ,  $0 \leq v \leq 1 - u$ . Figure 6.2 defines the local frames on three subpatches of facet  $f$ .

Equation 6.14 also presents the transformation from the local coordinates  $(u, v)$  of patch *ID* to the position vector  $\mathbf{r}$  in body frame  $Oxyz$ . On the contrary, denoting

$$\begin{aligned} \mathbf{b}_1 &= B(0, 0; \mathbf{c}_{ID}^1, \mathbf{c}_{ID}^2, \dots, \mathbf{c}_{ID}^{15}), \\ \mathbf{b}_2 &= B(0, 0; \mathbf{c}_{ID}^1, \mathbf{c}_{ID}^2, \dots, \mathbf{c}_{ID}^{15}), \\ \mathbf{b}_3 &= B(0, 0; \mathbf{c}_{ID}^1, \mathbf{c}_{ID}^2, \dots, \mathbf{c}_{ID}^{15}), \end{aligned} \quad (6.15)$$

the local coordinates  $(u, v)$  of  $\mathbf{r}$  on patch *ID* could be obtained by

$$\begin{aligned} u &= -\frac{\mathbf{r} \times \mathbf{b}_1 \cdot (\mathbf{b}_3 - \mathbf{b}_1)}{\mathbf{r} \times (\mathbf{b}_2 - \mathbf{b}_1) \cdot (\mathbf{b}_3 - \mathbf{b}_1)}, \\ v &= -\frac{\mathbf{r} \times \mathbf{b}_1 \cdot (\mathbf{b}_2 - \mathbf{b}_1)}{\mathbf{r} \times (\mathbf{b}_3 - \mathbf{b}_1) \cdot (\mathbf{b}_2 - \mathbf{b}_1)}. \end{aligned} \quad (6.16)$$

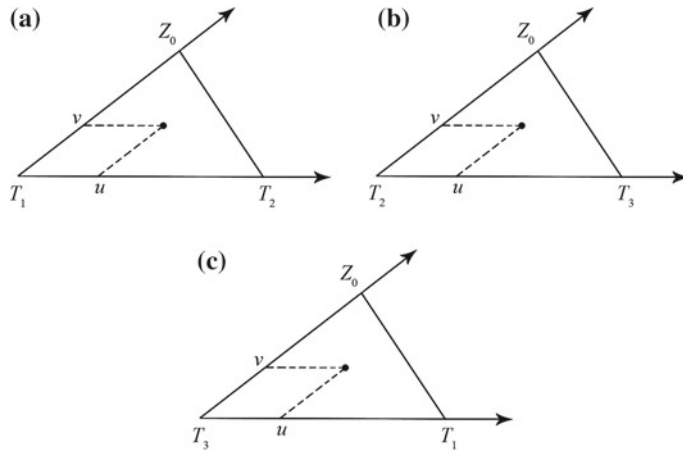


**Fig. 6.2** Definitions of the local affine frames on three sub patches of facet  $f$ . **a**  $ID = (f, 1)$ . **b**  $ID = (f, 2)$ . **c**  $ID = (f, 3)$

The Bézier patches expressed by Eq. 6.14 construct a global surface model of the asteroid, which is  $C^\infty$  continuous inside the patches, and  $G^1$  continuous on the cubic borders. In addition, Hugentobler et al. proved that for triangular facets, these patches are actually  $C^1$  continuous on the borders, thus, this approach provides fine smoothness to meet our requirements for the simulation of migrating grains on the asteroid's surface.

### 6.2.3 Equation of Motion on Surface

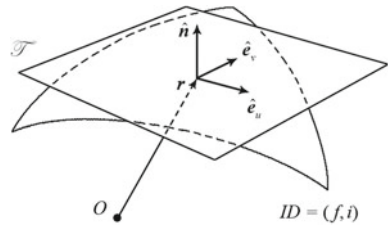
For the first stage of our study, we model the object, either natural or artificial, as a tracer particle, which is sizeless and has no effects on the motion of the asteroid. A mass point moving on the interpolated surface feels four types of forces: the gravity from the asteroid, the centrifugal force due to the rotation, Coriolis force and contact force from the surface (including the normal supportive force and tangential friction). The definition of Coulomb friction is adopted, i.e. the frictional coefficients are constant, denoted as  $\mu_s$  (static friction) and  $\mu_k$  (dynamic friction). Thus the motion equation of a mass point on patch  $ID$  is

$$\ddot{\mathbf{r}} + 2\boldsymbol{\omega} \times \dot{\mathbf{r}} = -\nabla V + N\hat{\mathbf{n}} - \mu_k N\hat{\mathbf{r}}, \quad (6.17)$$

in which  $N$  is the normal supportive force, and  $\hat{\mathbf{n}}$  is the unit normal vector pointing outwards. Define a local affine frame on patch  $ID$  with three unit base vectors  $\hat{\mathbf{e}}_u$ ,  $\hat{\mathbf{e}}_v$  and  $\hat{\mathbf{n}}$ , which are determined by Eq. 6.14:

$$\hat{\mathbf{e}}_u = \frac{\mathbf{B}_u}{|\mathbf{B}_u|}, \quad \hat{\mathbf{e}}_v = \frac{\mathbf{B}_v}{|\mathbf{B}_v|}, \quad \hat{\mathbf{n}} = \frac{\hat{\mathbf{e}}_u \times \hat{\mathbf{e}}_v}{|\hat{\mathbf{e}}_u \times \hat{\mathbf{e}}_v|}. \quad (6.18)$$

**Fig. 6.3** The local affine frame on Bézier patch  $ID$



$B_u, B_v$  indicate the partial derivatives of Eq. 6.14 for  $u, v$ , respectively. As illustrated in Fig. 6.3,  $\hat{e}_u, \hat{e}_v$  span a tangent plane of the Bézier patch at  $(u, v)$ , denoted as  $T$ , thus, the velocity vector  $\dot{r}$  lies on  $T$ . Take the first and second derivatives of Eq. 6.14 with respect to  $t$ , we have

$$\dot{r} = B_u \dot{u} + B_v \dot{v}, \quad (6.19)$$

$$\ddot{r} = B_u \ddot{u} + B_v \ddot{v} + B_{uu} \dot{u}^2 + 2B_{uv} \dot{u} \dot{v} + B_{vv} \dot{v}^2, \quad (6.20)$$

where  $B_{uu}, B_{uv}, B_{vv}$  are second derivatives for  $u$  and  $v$ .

Substituting Eqs. 6.14, 6.19 and 6.20 into Eq. 6.17, we have the motion equation form represented with local coordinates.

$$B_u \ddot{u} + B_v \ddot{v} = N \hat{n} - F, \quad (6.21)$$

where  $F$  is defined as

$$F = \nabla V \circ B + \mu_k N \frac{B_u \dot{u} + B_v \dot{v}}{|B_u \dot{u} + B_v \dot{v}|} + 2\omega \times (B_u \dot{u} + B_v \dot{v}) + B_{uu} \dot{u}^2 + 2B_{uv} \dot{u} \dot{v} + B_{vv} \dot{v}^2. \quad (6.22)$$

The operator  $\circ$  indicates the compound between functions. Noting  $B_u \cdot \hat{n} = 0$  and  $B_v \cdot \hat{n} = 0$ , the supportive force  $N$  satisfies

$$N = \hat{n} \cdot [\nabla V \circ B + 2\omega \times (B_u \dot{u} + B_v \dot{v}) + B_{uu} \dot{u}^2 + 2B_{uv} \dot{u} \dot{v} + B_{vv} \dot{v}^2]. \quad (6.23)$$

Equation 6.21 is apparently superfluous. In order to decouple the  $\ddot{u}$  and  $\ddot{v}$  terms, we multiply  $B_u, B_v$  on both sides, respectively.

$$\begin{aligned} B_u \cdot B_u \ddot{u} + B_u \cdot B_v \ddot{v} &= -B_u \cdot F \\ B_u \cdot B_v \ddot{u} + B_v \cdot B_v \ddot{v} &= -B_v \cdot F \end{aligned} \quad (6.24)$$

Since vectors  $B_u, B_v$  are always independent, the coefficient matrix of Eq. 6.24 is guaranteed to be nonsingular. Therefore, Eq. 6.24 actually presents an explicit form of surface motion equation on patch  $ID$ .

### 6.3 Modelling the Natural Motion Near the Surface

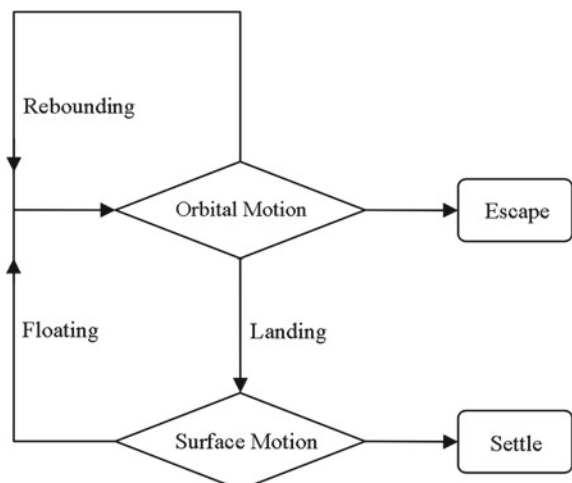
Equations 2.22 and 6.24 govern the motion of a mass point orbiting around the asteroid and sliding on its surface, respectively, which are two simple forms that will be considered in this section (the real interactions of the grain with the asteroid could be more complicated). We take the global trajectory as a chain of orbiting and sliding above/on the surface, with links of instantaneous collision or liftoff. Namely, it is an event-driven method. Figure 6.4 presents a diagram for the event-driven model, showing the simulator would be stopped in two cases: first, the particle is escaping out of the influential sphere (see Sect. 2.2 for the definition); second, the sliding motion is damped out by frictions and stops somewhere on the surface. Three types of triggering events are declared: first, the orbiting particle collides with the surface and bounds off, entering a new segment of orbiting, named “rebounding”; second, the orbiting particle falls down to the surface and switches to the sliding mode, named “landing”; third, a sliding particle reaches a speed over the criterial value and lifts off the surface, named “floating”.

Following two sections go to separate discussions on these events.

#### 6.3.1 Triggering Events Within Orbital Motion Segments

Two types of events occur within the orbiting mode: rebounding and landing. And to identify these events, a collisional detection must be done beforehand. Considering two adjacent time steps  $t_k$  and  $t_{k+1}$  ( $k = 0, 1, 2, \dots$ ), and corresponding position vectors  $\mathbf{r}_k$ ,  $\mathbf{r}_{k+1}$  with the local coordinates  $(u_k, v_k)$ ,  $(u_{k+1}, v_{k+1})$ , respectively. The condition of the particle colliding with the surface between  $t_k$  and  $t_{k+1}$  yields

**Fig. 6.4** A diagram of the event-driven model. The *diamonds* indicate process states, *rounded rectangles* indicate the terminative states, and triggering events are labeled beside the flow lines



$$|\mathbf{r}_k| > |B(u_k, v_k)| \cap |\mathbf{r}_{k+1}| \leq |B(u_{k+1}, v_{k+1})|. \quad (6.25)$$

Here, the target small body is supposed to have a star shape, i.e., it contains a point from which the entire surface is visible. The colliding site is determined using Eqs. 6.26 and 6.27.

$$\lambda_{pos} = \frac{(|\mathbf{r}_k| - |B(u_k, v_k)|) |\mathbf{r}_{k+1}|}{|\mathbf{r}_k| |B(u_{k+1}, v_{k+1})| - |\mathbf{r}_{k+1}| |B(u_k, v_k)|}, \quad (6.26)$$

$$\mathbf{r}_c = (1 - \lambda_{pos})\mathbf{r}_k + \lambda_{pos}\mathbf{r}_{k+1}. \quad (6.27)$$

Likewise, the colliding speed could be calculated by linear interpolation using Eqs. 6.28 and 6.29.

$$\lambda_{vel} = \frac{(|\mathbf{r}_k| - |B(u_k, v_k)|) |B(u_{k+1}, v_{k+1})|}{|\mathbf{r}_k| |B(u_{k+1}, v_{k+1})| - |\mathbf{r}_{k+1}| |B(u_k, v_k)|} \quad (6.28)$$

$$\dot{\mathbf{r}}^- = \lambda_{vel}\dot{\mathbf{r}}_k + (1 - \lambda_{vel})\dot{\mathbf{r}}_{k+1} \quad (6.29)$$

As illustrated in Fig. 6.5, the collision is treated as an instantaneous interaction with the local tangent plane, i.e. the position remains before and after the collision, and the velocity changes immediately, as described in Eqs. 6.30 and 6.31. The energy loss due to the surface coupling is approximated by introducing the restitution coefficients,  $\epsilon_n$  (normal coefficient,  $0 \leq \epsilon_n \leq 1$ ) and  $\epsilon_t$  (tangent coefficient,  $-1 \leq \epsilon_t \leq 1$ ).

$$\dot{\mathbf{r}}^- = \dot{\mathbf{r}}_n^- + \dot{\mathbf{r}}_t^-, \quad (6.30)$$

$$\dot{\mathbf{r}}^+ = -\epsilon_n \dot{\mathbf{r}}_n^+ + \epsilon_t \dot{\mathbf{r}}_t^+. \quad (6.31)$$

Equations 6.30 and 6.31 represent the normal and tangent components of the incoming and outgoing velocities. For instance,  $\epsilon_n = 0, \epsilon_t = 0$  means the particle is stuck once touching the surface;  $\epsilon_n = 1, \epsilon_t = 1$  means perfect bouncing by smooth surface.

In order to discriminate the “rebounding” and “landing” cases, we estimate, the height of bouncing off and compare it with the numeric tolerance. Denoting  $g_n$  as

**Fig. 6.5** The relative velocities before and after the collision

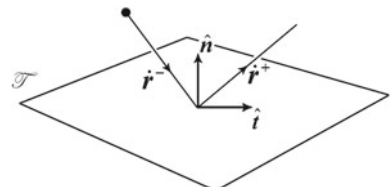
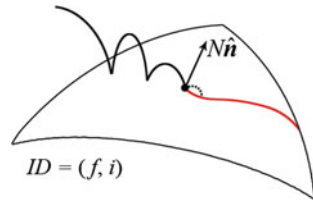


**Fig. 6.6** Triggering events “rebounding” and “landing” on patch  $ID$ . The orbiting and sliding segments are indicated with dark, red curves, respectively



the normal component of local gravitational acceleration, the scaled bouncing-off height is

$$l = \frac{|\dot{\mathbf{r}}_n^+|^2}{2g_n[L]}, \quad (6.32)$$

and comparing  $l$  with the tolerance  $l_\epsilon$  (in this section we set  $l_\epsilon = 10^{-4}$ ), two cases are then separated:

1. **Rebounding** ( $l > l_\epsilon$ )

In this case, the motion after the collision is still orbiting, which is initialized with the position  $\mathbf{r}_c$  and the velocity  $\dot{\mathbf{r}}^+$ , as shown in Fig. 6.6.

2. **Landing** ( $l < l_\epsilon$ )

In this case, the motion after the collision is sliding on the surface (Fig. 6.6), which is initialized with the position  $\mathbf{r}_c$  and a tangent velocity  $\dot{\mathbf{r}}^+ = \epsilon_t \dot{\mathbf{r}}_t^-$ .

In addition, the tolerance height  $l_\epsilon$  is also used to estimate the time step of numeric integration  $\Delta t$ , which satisfies

$$\Delta t < \frac{1}{2} \sqrt{\frac{2l_\epsilon[L]}{g_n}}. \quad (6.33)$$

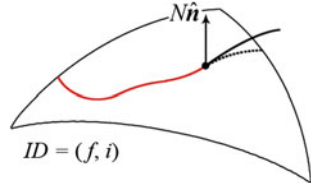
### 6.3.2 Triggering Events Within Surface Motion Segments

The triggering event “floating” occurs within the sliding mode, i.e., the sliding speed exceeds the liftoff speed and enters an orbit. Obviously, it happens only if the supportive force  $N$  turns negative (see Fig. 6.7), and the initial conditions of the orbital motion are determined by Eqs. 6.14 and 6.19.

Besides, the sliding mode comes to the terminate state if the relative speed is 0 and the tangent acceleration lies below the limit of static friction, i.e., the particle stops in the equilibrium region, s.t.

$$\mu_s |\nabla V \cdot \hat{\mathbf{n}}| > |(\nabla V \cdot \hat{\mathbf{n}}) \hat{\mathbf{n}} - \nabla V|. \quad (6.34)$$

**Fig. 6.7** Triggering event “floating” on patch  $ID$ . The orbiting and sliding segments are indicated with dark, red curves, respectively



### 6.3.3 Global Trajectory Patching Technique

As the triggering events occurring on the Bézier patches have been processed, this section focuses on the implementation of global tracking technology, i.e., to build a simulation scheme that enables automatic conversion between different motion modes. Since the surface is patched up with interpolated patches, and the surface motion is represented in local coordinations, there exist two obvious barriers for global tacking: first, the local coordinates should be recalculated when a particle is sliding across the border of the patch; second, the  $ID$  needs to be identified when an orbiting particle lands on a patch and starts sliding.

#### 1. Local coordinates transformation

For arbitrary patch  $ID$ , Table 6.1 defines 6 borders, including edges  $b_1, b_2, b_3$  and vertices  $b_4, b_5, b_6$ . The coordinates  $u, v$  on patch  $ID$  satisfy  $0 \leq u \leq 1$ ,  $0 \leq v \leq 1 - u$ , and once the sliding trajectory going across one of these borders,  $ID$  must be updated and  $u, v$  must be recalculated.

Given two connected patches  $ID_1$  and  $ID_2$ , and assuming the particle is going from  $ID_1$  to  $ID_2$ , corresponding local coordinates of the start and end points represented on  $ID_1$  are denoted as  $(u_k, v_k)$  and  $(u_{k+1}, v_{k+1})$ , and the intersection point with the border is denoted as  $(u_b, v_b)$  on  $ID_1$  and  $(u'_b, v'_b)$  on  $ID_2$ . As illustrated in Fig. 6.8, the edge borders and vertex borders must be treated separately.

Apparently, the vertex border case is more complicated because more than two patches are sharing the common border and we have to search for the “real” connected one, which could be done by projecting all neighbour patches to the current plane and checking all the edge vectors. After the target patch locked, namely,  $ID_2$  fixed, the intersection point could be determined via interpolation and the

**Table 6.1** The definitions of 6 borders of patch  $ID$

Boundary	Local coordinates
$b_1$	$u = 0, 0 \leq v \leq 1$
$b_2$	$v = 0, 0 \leq u \leq 1$
$b_3$	$u + v = 1, u \geq 0, v \geq 0$
$b_4$	$u = 0, v = 0$
$b_5$	$u = 1, v = 0$
$b_6$	$u = 0, v = 1$

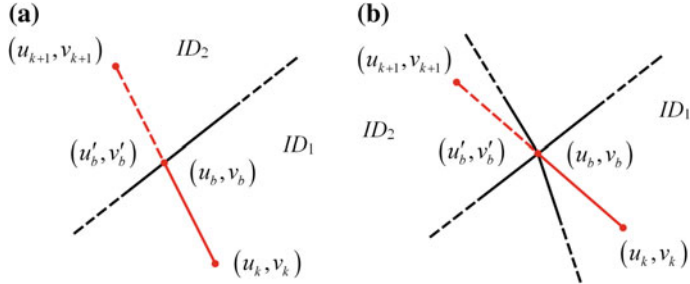


**Fig. 6.8** The two cases when the particle crossing the common border of connected patches  $ID_1$  and  $ID_2$ . **a** The edge border case. **b** The vertex border case

**Table 6.2** The correlations of local coordinates on connected patches  $ID_1$  and  $ID_2$

Boundary of $ID_1$	$(u_b, v_b)$	Boundary of $ID_2$	$(u'_b, v'_b)$
$b_1$	$(0, v)$	$b_3$	$(1 - v, v)$
$b_2$	$(u, 0)$	$b_2$	$(1 - u, 0)$
$b_3$	$(u, 1 - u)$	$b_1$	$(0, 1 - u)$
$b_4$	$(0, 0)$	$b_4$	$(0, 0)$
		$b_5$	$(1, 0)$
$b_5$	$(1, 0)$	$b_4$	$(0, 0)$
		$b_5$	$(1, 0)$
$b_6$	$(0, 1)$	$b_6$	$(0, 1)$

current step  $k + 1$  should be reset back to  $(u_b, v_b)$  to avoid any skipping over, and the local coordinates on patch  $ID_2$   $(u'_b, v'_b)$  could be determined according to the correlation listed in Table 6.2.

Equations 6.35 and 6.36 present the local coordinates of the position and velocity at the intersection point, represented on patch  $ID_1$ .

$$(u_b, v_b) = \eta(u_k, v_k) + (1 - \eta)(u_{k+1}, v_{k+1}), \quad 0 \leq \eta \leq 1, \quad (6.35)$$

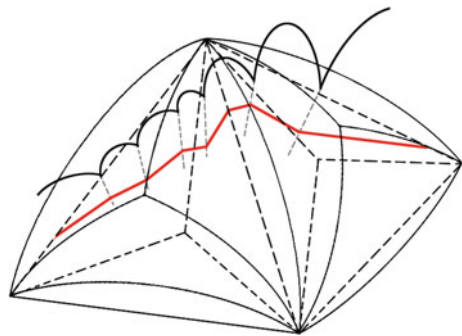
$$(\dot{u}_b, \dot{v}_b) = \eta(\dot{u}_k, \dot{v}_k) + (1 - \eta)(\dot{u}_{k+1}, \dot{v}_{k+1}). \quad (6.36)$$

And the local coordinates of the crossing velocity on patch  $ID_2$  could be derived via Eqs. 6.16 and 6.19.

## 2. Tracing an orbiting particle

The global motion may contain several segments of orbits, and each time when the orbiting mode is switched to the sliding mode, the Bézier patch must be repositioned, i.e., to identify the  $ID$  of current patch. A straight approach is to search over all the  $3N_f$  patches of the surface, which would be computationally expen-

**Fig. 6.9** The ground trace (red lines) of a segment of trajectory (dark curves)



sive for a high-resolution polyhedral model when the number of facets is very large.

A more efficient approach to trace an orbiting particle is proposed here. First, the ground trace is defined as the centripetal projection of the trajectory (on-orbit or on the Bézier patch) onto the polyhedron, which is unique and guaranteed to exist. As illustrated in Fig. 6.9, the ground trace is continuous, and it is simple to track and update its local *ID*. Thus, it plays as a link between the “real” trajectory and the local coordinates, which helps to rapidly position the *ID* when the particle crossing different patches or switching between two modes.

Figure 6.9 interprets how the ground trace works: the patch *ID* and local coordinates ( $u, v$ ) are calculated and recorded at each integration step (either orbiting or sliding), thus the local information will never be lost and can be called anytime when triggering events happen.

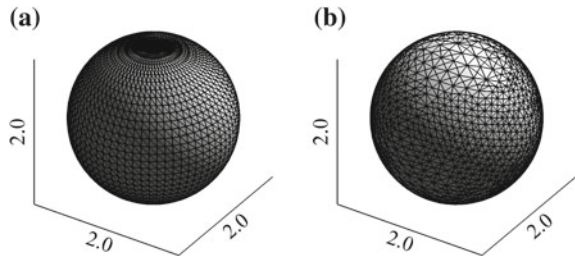
## 6.4 Verification and Assessment

A series of fundamental tests are performed to validate the methodology proposed in this chapter. Examples include testing the modified gravitational model near the surface of the polyhedron, checking the orbital behaviours with different initial conditions, etc.

### 6.4.1 Example 1: Gravitational Field of a Solid Sphere

A homogeneous unit sphere is considered to test the gravitational model, because its potential and attraction are analytically determined both at exterior and interior. Assuming the density and gravitational constant are both 1, Eqs. 6.37 and 6.38 calculate the potential and gravity varying as the radial distance  $r$ .

**Fig. 6.10** Meshes of the unit sphere generated with different surface divisions.  
**a** Standard grid. **b** Random grid



$$U = \begin{cases} \frac{2\pi}{3}(r^2 - 3) & r \leq 1 \\ -\frac{4\pi}{3r} & r > 1 \end{cases} \quad (6.37)$$

$$\nabla U = \begin{cases} \frac{4\pi}{3}r & r \leq 1 \\ \frac{4\pi}{3r^2} & r > 1 \end{cases} \quad (6.38)$$

Figure 6.10 illustrates two polyhedral models of the unit sphere: the standard grid model (Fig. 6.10a) adopts a uniform surface division, i.e., meshes are generated following the latitude and longitude lines, which is a polyhedron of 2114 vertices and 4224 facets; the random grid model (Fig. 6.10b) adopts an arbitrary surface division and a polyhedron of 2048 vertices and 4096 facets are generated.

Equations 6.11 and 6.12 are applied to estimate the gravitational field induced by the two polyhedral models shown in Fig. 6.10, especially, for the values on the facets and the edges. Figure 6.11 compares the theoretical values and numerical values as  $r$  changing from 0 to 2.

Figure 6.11 shows the theory values and the numerical results at the test points are exactly consistent both at the interior and the exterior. In particular, the singularity at the edge and facet of the polyhedron has been removed, which provides a complete solution to our problem.

#### 6.4.2 Example 2: Demonstration Trajectories over Different Bodies

As a further validation of our methodology, this section presents some demonstration trajectories near/on the surface a specific small bodies. Figure 6.12a illustrates several typical trajectories around a nonrotating homogeneous sphere (random grid model, see Sect. 6.4.1). Assuming the dynamical factor  $\kappa = 1.0$ , and the friction coefficients  $\mu_s = 0.6$ ,  $\mu_k = 0.5$ , the restitution coefficients  $\epsilon_n = 0.6$ ,  $\epsilon_t = 0.9$ , trajectory 1 is a hyperbolic orbit that has an initial speed exceeding the escaping speed; trajectory 2 is an elliptic (periodic) orbit cycling around the sphere; and trajectory 3 is a collisional orbit with a small initial speed, followed with a series of hopping, sliding and eventually stopped on the surface.

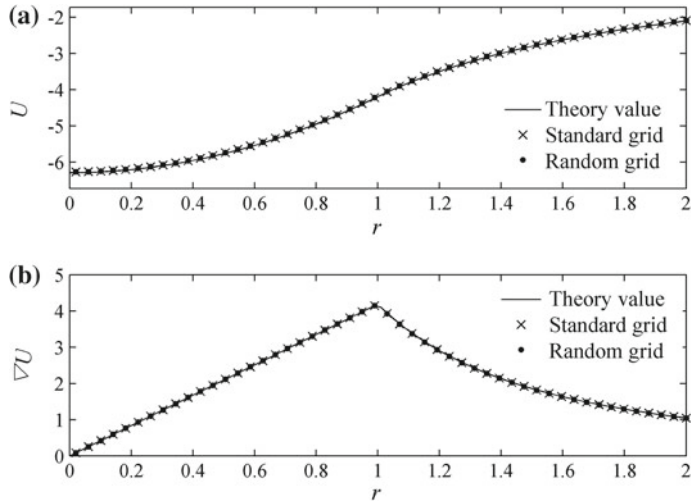


**Fig. 6.11** The comparison of the potential and gravity derived from analytical formula and modified polyhedral model. The *solid line* indicates the theoretical value, the *crosses* indicate the result from the standard grid model, and the *circles* indicate the result from the random grid model. **a** The potential variation as the radial distance  $r$ . **b** The gravity (magnitude) variation as the radial distance  $r$

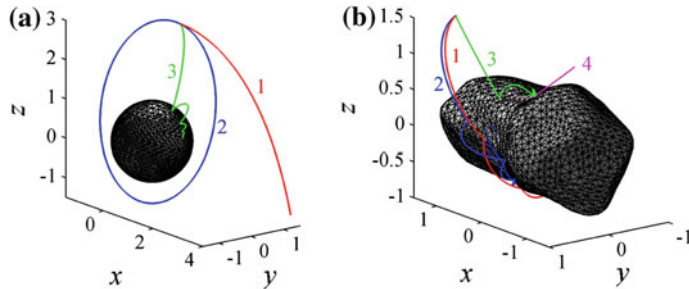


**Fig. 6.12** Typical trajectories near/on the surfaces of example bodies, including a homogeneous sphere **(a)** and the asteroid 2063 Bacchus **(b)**

Figure 6.12b shows 4 representative trajectories around the normalized polyhedral model of asteroid 2063 Bacchus, which includes 2048 vertices and 4092 facets. Assuming the dynamical factor  $\kappa$  to be 468.27, and the friction and restitution coefficients as set above, trajectories 1 and 2 keep close at first but experience a separation after multiple rebounds, showing a high sensitivity to the initial conditions; trajectory 3 shows a transformation from “orbiting” to “sliding”, and eventually the particle stops at the bottom of a crater; trajectory 4 shows a transformation from “sliding” to “orbiting”, which starts from the bottom of a crater, and lifts off as the particle rushing out of the rim.

## 6.5 Analysis of the Natural Motion Near Asteroid 1620 Geographos

The methodology is applied to mimic the natural motion near asteroid 1620 Geographos, serving as a database to understand the dynamical environment close to the surface. 1620 Geographos is taken as the target asteroid because it has representative rugged landscapes [6], which is a typical case for this study.

Figure 6.13 illustrates the polyhedral model of Geographos, which includes 16,380 vertices and 24,570 facets. We assume the bulk density to be 2.0 g/cc (homogeneous), and the rotational period to be 5.22 h (spinning around the principal axis of maximum inertia). A calculation shows the gravity and centrifugal force are complementary in magnitude: in the middle region of the asteroid, the gravity is much larger than the centrifugal force, i.e., the surface motion in this area is dominated by gravity; while near the tips along the long axis, the magnitudes of these two forms are comparable, generating a low-gravity region in which moving objects can escape easily.

Except the gravity and centrifugal force, the most influential factor to the natural motion is the features of the surface, including the geometric features and mechanical properties. Here, we first discuss the effects of local slope and curvature of Geographos' surface.

### 6.5.1 Surface Slope and Equilibrium Area

The surface slope relies on the local gravity and local geography. Equation 6.39 gives a definition of the slope:

$$\phi = \arccos(-\hat{\mathbf{g}} \cdot \hat{\mathbf{n}}), \quad 0 \leq \phi \leq \pi \quad (6.39)$$

**Fig. 6.13** The polyhedral shape model of asteroid 1620 Geographos

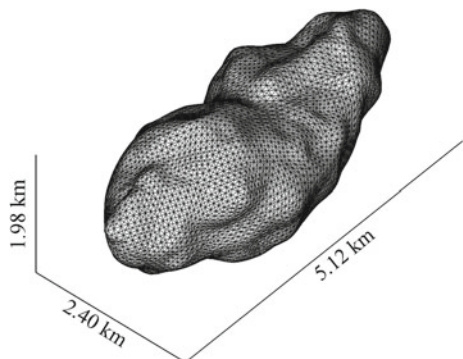
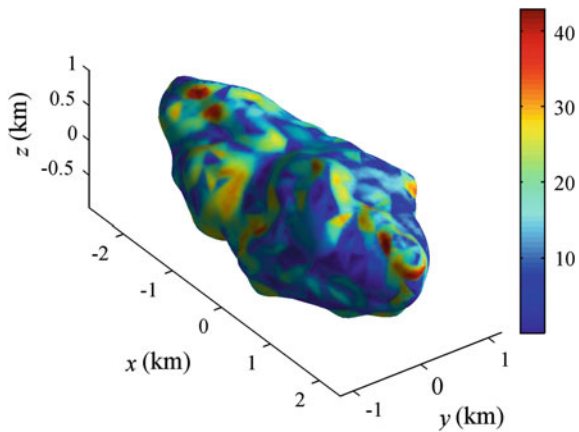


**Fig. 6.14** The distribution of surface slope over Geographos, unit:  $^{\circ}$ . The slope angle is scaled by the color bar and mapped onto the interpolated asteroid surface



where  $\hat{g}$  indicates the unit vector in direction of the local gravity,  $\hat{n}$  indicates the normal vector of the Bézier patch. Obviously, for real asteroids, we have  $0 \leq \phi \leq \pi/2$ . Figure 6.14 illustrates distribution of the slope over the surface of Geographos, which varies hugely due to the sophisticated local terrain. The slope angle, ranging up to a maximum of  $42.9^{\circ}$ , presents notable regional distribution; wherever hills or a craters that contains steep walls exist, there will be highlighted areas with large slopes. The average slope over the entire body is  $\sim 13.8^{\circ}$ .

The information that Fig. 6.14 gives is correlated with the distribution of the regolith on the surface of the asteroid. The area of surface where the weathered material may exist depends on the local angle of repose  $\theta_r$ : regolith material is probable to accumulate only in the area where  $\phi < \theta_r$  [7], which is called equilibrium area. Approximately, taking the regolith as granular media, the angle of repose  $\theta_r$  and static friction coefficient  $\mu_s$  satisfy

$$\mu_s \approx \tan \theta_r. \quad (6.40)$$

Table 6.3 lists the proportions of the equilibrium region for different  $\theta_r$  values, i.e., the ratio of area in the entire surface of Geographos.

As shown by Table 6.3, the particle can stop everywhere on the surface when  $\theta_r$  exceeds the peak slope of Geographos  $42.9^{\circ}$ , and  $\sim 97\%$  of the surface has a slope below  $30^{\circ}$ . As  $\theta_r$  decreasing, the equilibrium region shrinks rapidly, and when  $\theta_r = 10^{\circ}$ , only one third of the surface could be deposited with regolith material.

### 6.5.2 Surface Curvature and Liftoff Speed

Another local geometric feather that matters to the surface motion is the curvature, which defines the convexity/concavity of the surface in the direction of motion.

**Table 6.3** The proportions of the equilibrium region for different angles of repose

Angle of repose $\theta_r$	Static friction $\mu_s$	Proportion of equilibrium area (%)
40°	0.84	99.90
30°	0.58	97.26
20°	0.36	81.24
10°	0.18	33.89

Equations 6.41 and 6.42 present the first and second fundamental forms based on the expressions of Bézier patches.

$$E = B_u \cdot B_u, \quad F = B_u \cdot B_v, \quad G = B_v \cdot B_v \quad (6.41)$$

$$L = B_{uu} \cdot \hat{\mathbf{n}}, \quad M = B_{uv} \cdot \hat{\mathbf{n}}, \quad N = B_{vv} \cdot \hat{\mathbf{n}} \quad (6.42)$$

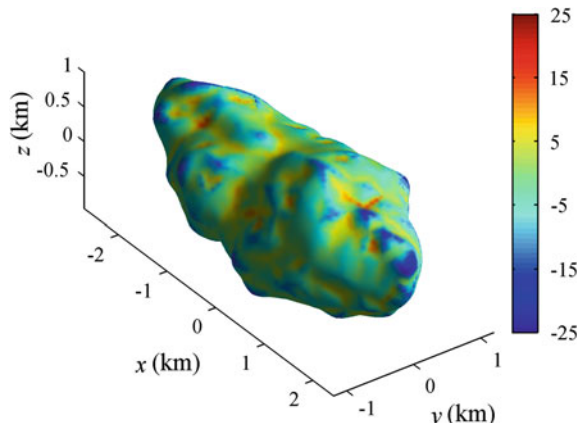
And the mean curvature is defined as

$$H_c = \frac{EN + LG - 2FM}{2(EG - F^2)}, \quad (6.43)$$

which is an average of the principal curvatures. Figure 6.15 illustrates the distribution of the mean curvature over the surface of Geographos, revealing a connection between the mean curvature and local topography:

1. The mean curvature usually reaches the minimum on the ridges or tops of the hill (marked in blue);
2. The valleys and basins of craters marked in red usually have the maximum values of the mean curvature.

**Fig. 6.15** The distribution of the mean curvature over Geographos, which is scaled by the color bar and mapped onto the interpolated asteroid surface



For a particle sliding on the surface, the liftoff speed is defined as the minimum speed to float over the surface along some direction (see Sect. 6.3.2). It is apparently related with the local curvature in the direction of motion. Generally, the particle sliding on a concave patch can never lift off no matter how large the speed is; the particle sliding on a convex patch may rush out in any directions in the tangent plane when its speed is high enough; for a saddle patch, it becomes a little complicated, only in those directions that have a negative curvature (convex) the particle can lift off the surface, and these directions make up some percentage of all directions in the local tangent plane. Equation 6.44 presents the criterion of local liftoff speed  $c$ .

$$(Ldu^2 + 2Mdudv + Ndv^2)c^2 + 2\omega \times (B_u du + B_v dv) \cdot \hat{n}c + \nabla V \circ B \cdot \hat{n} = 0, \quad (6.44)$$

where  $(du, dv)$  determines the sliding direction on the surface  $(du^2 + dv^2 = 1)$ . It provides a necessary and sufficient condition, that the particle could lift off along  $(du, dv)$  only if Eq. 6.44 has a solution. Several points should be stated based on a numerical search over the surface of Geographos:

1. All the positions with mean curvature  $H_c > 20$  are found to be convex, and all the positions with mean curvature  $H_c < -20$  are found to be concave;
2. The lower limit of the liftoff speed  $\sim 4.2$  mm/s appears around one tip of Geographos.

### 6.5.3 Behaviours of Global Trajectories over 1620 Geographos

The natural motion of a particle close to the surface gives important information for the mechanical environment. This section surveys the behaviours of global trajectories about Geographos based on Monte Carlo simulations. 300 positions are randomly chosen over the Bézier patches of Geographos, with a height ranging from 50 m to 200 m (close to the surface). Assuming  $\mu_s = 0.95$ ,  $\mu_k = 0.8$ ,  $\epsilon_n = 0.7$  and  $\epsilon_t = 0.7$ , all these sample particles are released from 0 velocity and the simulation are done until the particles finally stop on the surface. Figure 6.16 illustrates the distribution of these sample trajectories (snapshots are taken in two perspectives, with enlarged views of some area).

Figure 6.16 reveals a general evolutional path, that the trajectories will enter the sliding mode after multiple hops, then get damped by friction, and eventually stop in the equilibrium region. The local topography proves to be quite influential, and most test particles are finally trapped in nearby valleys/crater basins. Only a few trajectories, driven by the gradient potential field, take a long trip along the long axis and settle down in the low-lying area.

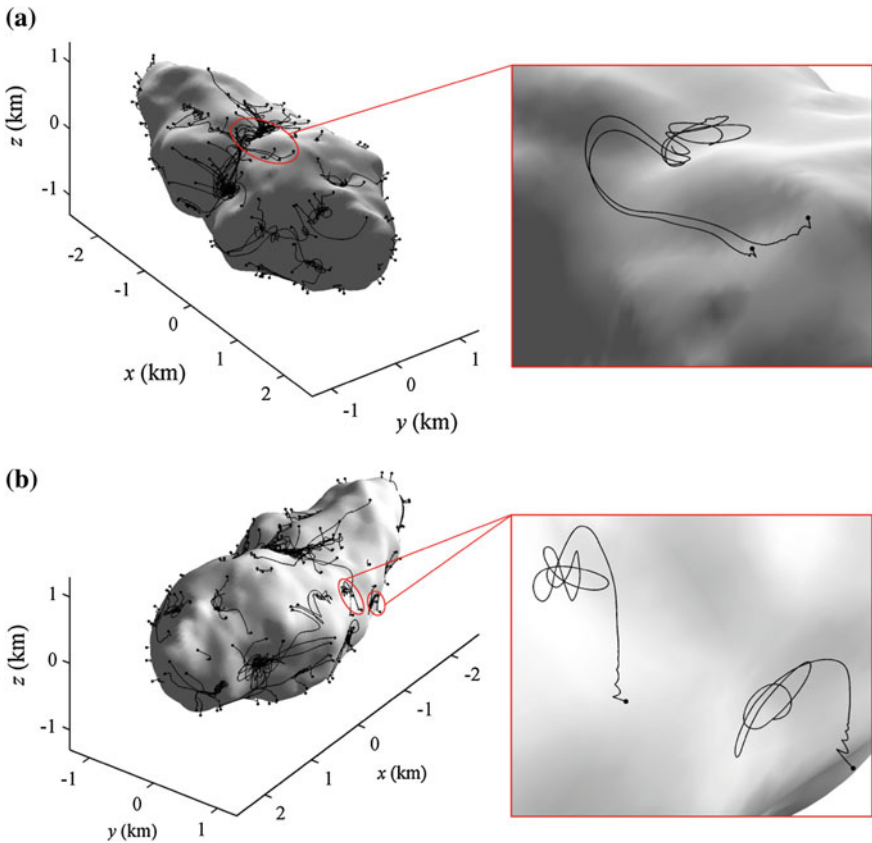


**Fig. 6.16** The distribution of sample trajectories over Geographos in two perspectives. The enlarged views show some typical morphologies of the trajectories. **a** Azimuth  $54^\circ$ , altitude  $33^\circ$ . **b** Azimuth  $126^\circ$ , altitude  $33^\circ$

These descriptions give a quick sketch of the global trajectories over the surface of Geographos, serving as a demonstration of our holistic methodology. As Geographos makes a typical object, we respect the approach and basic consequences portable to a group of similar systems.

## 6.6 Summary

This chapter focuses on the motion of a natural/artificial object near the surface of a small body. A global valid method for gravitational field calculation is first developed, which is a modified version of the polyhedral method proposed by Werner et al. Fundamental tests are organized to verify that the numerical singularity on the

facets and edges has been removed in our method. Then, an event-driven model is proposed to mimic the global trajectory of a particle moving near the small body, which combines the equations of surface motion and orbital motion in an efficient way. As the last part, this model is applied to track the surface motion close to a specified asteroid 1620 Geographos, showing the connections between the local geological features and the dynamical behaviours of the test particle:

1. The proportion of equilibrium region is correlated with the local angle of repose, and the static friction coefficient  $\mu_s$  is at least 0.93 to ensure the regolith material can accumulate everywhere on the surface of Geographos;
2. The liftoff speed  $c$  relies on the local curvature, gravity and centrifugal force, and for the positions with mean curvature  $H_c < -20$ , the particle may lift off the surface in any directions;
3. The lower limit of the liftoff speed  $\sim 4.2$  mm/s appears around the tip of Geographos;
4. Two types of global trajectories close to the Geographos' surface exist: most sample trajectories are trapped into nearby valleys/craters after several hops, but a few may have a long trip through the valleys along the long axis and eventually stop around the middle part of Geographos.

## References

1. Clark BE, Hapke B, Pieters C (2002) Asteroid space weathering and regolith evolution. In: William F et al (eds) *Asteroids III*, Univ. Arizona Press, Tucson, AZ, pp 603–612
2. Werner RA, Scheeres DJ (1997) Exterior gravitation of a polyhedron derived and compared with harmonic and mascon gravitation representations of asteroid 4769 Castalia. *Celest Mech Dyn Astron.* 65:313–344
3. Petrović S (1996) Determination of the potential of homogeneous polyhedral bodies using line integrals. *J. Geodesy* 71:44–52
4. Tsoulis D, Petrović S (2001) On the singularities of the gravity field of a homogeneous polyhedral body. *Geophysics* 66:535–539
5. Shirman LA, Séquin CH (1987) Local surface interpolation with Bézier patches. *Comput Aided Geom Des* 4:279–295
6. Hudson RS, Ostro SJ (1999) Physical model of Asteroid 1620 Geographos from radar and optical data. *Icarus* 140:369–378
7. Pudasaini SP, Hutter K (2007) Avalanche dynamics: dynamics of rapid flows of dense granular avalanches. Springer, Heidelberg

# Chapter 7

## Conclusions and Future Directions

### 7.1 Conclusions

Four types of orbital motion are discussed in this thesis: the equilibrium points, periodic orbits, resonant orbits near the equatorial plane and motion near the surface. The main consequences are summarized below.

In the study of equilibrium points, we present the 3D zero-velocity surfaces of asteroid Kleopatra with the gravity approximated using the polyhedral method. Four equilibrium points are positioned by checking the parameter dependence of zero-velocity surface, and all these points are found to be unstable. Equilibrium points in opposite directions are found to be topologically equivalent. Six local periodic families are derived from the centre manifolds about the equilibria, and we prove the orbits of all these families are unstable, consistent with corresponding equilibrium points. The motion around an equilibrium point is decomposed into three types of local manifolds (stable, unstable, and centre manifolds), and a qualitative analysis shows the general patterns of orbital behaviours in the neighbourhoods of the equilibria.

In the study of periodic motion, the Hierarchical Grid Search Method is proposed to find out large-scale periodic orbits around irregular bodies. As a demonstration of this method, 29 families of periodic orbits are generated around Kleopatra, showing the denseness of periodic motion about an irregular body. These periodic orbits are classified into 7 topological types according to the distribution of the characteristic multipliers. 13 families out of the 29 involve topological transformations, which prove to exist between the complex saddle and real saddle, real saddle and central saddle, or central saddle and general centre, and all the transformations occur in both directions. General motion patterns around a periodic orbit are derived based on a linearized analysis of Poincaré map, which are decomposed into 5 basic maps on the section: identity, unstable focus, stable focus, saddle and general centre.

In the study of resonant orbits near the equatorial plane, we focus on the 1:1 resonance. The energy analysis based on accurate gravitational model reveals that the essence of 1:1 resonance is the abrupt change of orbital energy caused by the non-

central gravitational field doing work along the convected velocity. A classification of 1:1 resonant orbits is proposed according to the energy increment, and example orbits for 3 typical cases are presented, respectively. As for the parameter dependence of the resonant orbits, we perform Monte Carlo simulations and find a banded region of high proportion of ejecting orbits close to the surface of Kleopatra, which could be dynamically dangerous for space crafts. The parameter condition of forming 1:1 resonance around Kleopatra is determined numerically, which is consistent with the observation of the orbits of natural satellites.

In the study of the migration of a grain on/over the surface, we propose a modified polyhedral method to remove the singularities on the edges. An interpolated surface model is developed, based on which we present the surface motion equations in local coordinates. The event-driven strategy is adopted to implement full simulation of a tracer particle moving near/on the surface of an asteroid. A series of fundamental tests are performed to validate our method, and the surface mechanical environment of asteroid 1620 Geographos is examined using this model. The connections between the local geological features and the dynamical behaviours of the test particle are revealed, e.g. the dependence of equilibrium region on the slope, and that of liftoff speed on the curvature. Most mitigation paths are found trapped into nearby valleys/craters, except a few paths taking a trip through the valleys along the long axis and eventually stop around the middle part of Geographos.

## 7.2 Future Directions

The literature on orbital dynamics in gravitational fields of small bodies has shown accelerated growth since the twenty nineties involving extensive physics and mathematics related with this subject. While as a new hotspot in modern celestial mechanics, these studies are rather scattered and lack of systemic. As stated above, this thesis presents our investigation to a few problems in this field, and along these directions, there are still a lot of issues worth further explorations

1. Since the polyhedral model has been widely accepted as a tool of describing the shape of a small body, the polyhedral method based on non-homogeneous assumption should be considered in order to give a better approximation to the gravitational field of the target asteroid, which will be necessary after its interior structure is measured by future space mission.
2. As for an asteroid surface lander, the mass point model is obviously over simplified. A solid body moving on rugged terrain should be considered, with more detailed mechanics included, like rolling and twisting frictions, etc.
3. The parameter dependence of the orbital behaviours has not been well understood, e.g. how will the number, position and stability of an equilibrium point change as the dynamical factor  $\kappa$  increasing? A general discussion on a perturbed system will feed us with knowledge of the common features about a large group of small bodies.

4. For a large-scale spacecraft, e.g. solar sail, tethered system, robotic arm, etc., the irregular gravitational field induced by the small body is apparently a tough working environment. The coupling effect between the orbital motion and librational motion in this context could be interesting and significant both in theory and in practice.